Studies on Microplasmas in Coaxial Dielectric Barrier Discharges and Their Application to Thin Film Deposition at Atmospheric Pressure

Yosuke ITO

March 2010

Abstract

Studies on Microplasmas in Coaxial Dielectric Barrier Discharges and Their Application to Thin Film Deposition at Atmospheric Pressure

Yosuke ITO

Kyoto University, 2010

This dissertation presents characteristics of microplasmas produced by coaxial dielectric barrier discharges and their application to plasma enhanced chemical vapor deposition (PE-CVD) of oxide films. The author investigated the properties of a microplasma array and an atmospheric-pressure plasma jet (APPJ) as plasma sources of coaxial dielectric barrier discharges. These plasma sources are used as either assembled arrays or single units of microplasmas, and they have high electron density and low gas temperature. Each of the following chapters presents experimental results, theoretical studies, and applications of coaxial dielectric barrier discharges.

In order to investigate the characteristic properties of coaxial dielectric barrier discharges, spectroscopic approaches such as optical emission spectroscopy (OES) and laser absorption spectroscopy (LAS) were applied to the APPJ. From these experiments, the gas temperature in the plasma plume is room temperature, and helium metastable excited atoms $He^*(2^3S_1)$ is produced only when the applied voltage is positive. Furthermore, the effects of the electric fields and the helium flow on the plasma were investigated by measuring the length of the plasma plumes of the microplasma array and the APPJ. From these experiments, it was found that the

plasma plume is propagated by the electric field along the helium flow and that the Reynolds number is one of key factors in the plasma plume's extension. The discharge mechanism of the APPJ was different between the plasmas in the capillary and those extending outside the tube. The direct and stepwise ionization reactions of helium atoms affect the generation of plasmas in the glass tube, but $He^*(2^3S_1)$ play important roles in producing plasmas by Penning ionization with nitrogen molecules in an extended plasma plume.

When the plasma extends into the ambient air, the effects of N_2, H_2O and O_2 are not negligible. Hence the electron density in nitrogen plasma generated in the microplasma array was analyzed by using a millimeter-wave transmission method. At atmospheric pressure, the generated plasma occupied almost the entire hollow-electrode space, and the electron density was estimated to be 10^{12} - 10^{13} cm^{-3}. This value is in good agreement with the theoretical prediction of a simple particle balance model. The effect of injecting small admixtures of H_2O and O_2 into nitrogen discharges at atmospheric pressure was also studied. In the case of H_2O addition, the measured electron density was lower than that in pure nitrogen plasma, especially in a highly reduced electric field, due to the deformation of the loss processes of electrons. In the case of O_2 addition, the electron density decreased with an increase in the O_2 concentration due to the additional loss process through the formation of negative ions.

In order to investigate the effect of accumulated charge on a substrate surface in the deposition of oxide films with the APPJ, the discharge current flowing into the copper substrate, which was placed 20 mm from the exit of the APPJ and connected to a variable capacitor in series, was measured. It was found that the discharge current decreased markedly when the capacitance of the substrate was below 100 pF, and the deposition rate of SiO_2 traced the variation of capacitance. To analyze the behavior of the APPJ, an equivalent circuit of this system was considered

and the validity of the supposition that the accumulated charge restricts the deposition rate was verified. Thereby, it was found that the discharge current and deposition rate were determined by the capacitance of both the glass tube wall and the substrate.

The experimental study of the PE-CVD of SiO_2 films from tetraethoxysilane (TEOS) using the APPJ is presented in Chapter 5. In this study, three different configurations: (a) a coaxial type, (b) a crossed type with a vertical plasma jet and a tilted TEOS supply, and (c) another crossed type with the reversed arrangement of the configuration (b) were attempted. The deposition rate of SiO_2 films increased with the driving frequency of the APPJ in all configurations, and as the best result, it reached up to 400 nm/s at a driving frequency of 30 kHz in the configuration (c) with the aid of O_3 supply, which was about four times as fast as the measured deposition rate in the configuration (a) without O_3 supply. From numerical calculation, this might be due to long residence time of the precursors in the plasma. It leads to production of inactive powders.

In Chapter 6, the PE-CVD using the APPJ was also applied to deposition of ZnO films. Using vaporized bis(octane-2,4-dionato)zinc ($Zn(OD)_2$) flow crossed by the APPJ, the deposition rate was about 160 nm/s. From the results of infrared spectra, the films deposited at a substrate temperature of T_{sub} = 100℃ contained a significant amount of carbon residue, while the films prepared at T_{sub} = 250℃ showed a lower carbon fraction. The experimental results confirmed that the APPJ decomposed $Zn(OD)_2$ in the gaseous phase and on the substrate and that there should be a critical level of T_{sub} to form high-quality ZnO films in the range from 100 to 250℃. By annealing the films, the transparency showed a drop at around 370 nm corresponding to the band gap energy of zinc oxide, and the resistivity was of the order of 10^6 Ωcm. Hence, the transparent and semiconductor-like films were obtained.

This dissertation describes the techniques for measuring the electron density of microplasmas at atmospheric pressure and the characteristic features of the coaxial dielectric barrier discharges. Furthermore, it also describes the possibilities of PE-CVD of oxide films, such as SiO_2 and ZnO, by the microplasmas based on coaxial dielectric barrier discharge.

List of Figures

List of Tables

Contents

Chapter 1

Introduction

1.1 Historical Background of Plasma Processing

Plasma enhanced chemical vapor deposition (PE-CVD) is now commonly used in the semiconductor industry. PE-CVD is a process used to deposit thin films from a source material gas onto a substrate. The plasma generates active species, such as electrons, ions, and radicals. These bring about chemical reactions with the source material gas and decompose it. Figure 1.1 shows typical configurations of PE-CVD systems. Figure 1.1(a) shows capacitively coupled plasma (CCP), which has been used as a high-pressure and low-electron-density plasma source. By applying a very high frequency (VHF, 40 - 100 MHz), the electron density n_e becomes high and the electron temperature T_e becomes low, making it possible to deposit fairly light-degradation-free films. Figure 1.1(b) shows inductively coupled plasma (ICP), which is

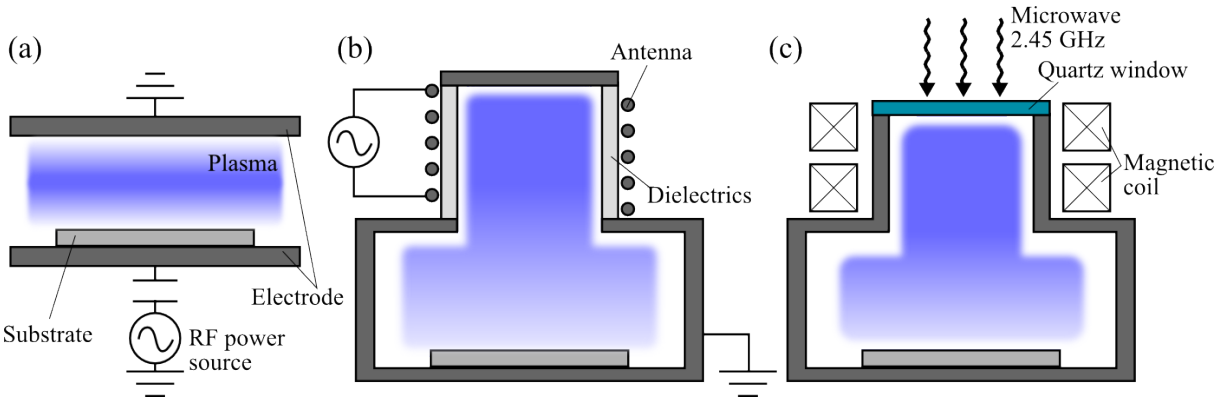

Figure 1.1 Typical configurations of PE-CVD at low pressure: (a) CCP-CVD, (b) ICP-CVD and (c) ECR-CVD.

Table 1.1 Electron temperature T_e, electon density n_e, and pressure p of typical plasma sources.

	T_e (eV)	n_e (cm^{-3})	p (Pa)
RF CCP	1 - 4	10^8 - 10^{10}	10 - 1000
RF ICP	2 - 5	10^9 - 10^{12}	0.1 - 10
ECR	2 - 5	10^{11} - 10^{13}	0.01 - 1

one of the plasma sources that have low pressure and high electron density [1.1]. By using ICP, microcrystalline or polycrystalline silicon can be obtained at a relatively low temperature. Figure 1.1(c) is a schematic draw of electron cyclotron resonance (ECR) plasma. ECR plasma can be driven at lower pressure and has higher T_e than the others. Therefore ECR plasma has made plasma processing sophisticate.

PE-CVD was developed by R. C. Chittick *et al.* in 1969 [1.2]. They formed silicon thin films by ICP using silane gas. Although thermal CVD had previously accounted for the major portion of CVD, from this development PE-CVD has been investigated in the semiconductor industry for application to the formation of thin films, such as polycrystalline silicon and silicon dioxide [1.3–5]. Subsequently, many methods have been developed and leveraged in a wide range of areas. These include, for example, microwave CVD developed by Kamo *et al.* [1.6] and ECR-CVD improved by Matsuo *et al.* [1.7]. Typical conditions of the plasma sources are listed in Table 1.1. Those types of PE-CVD are driven under low pressure. Since electrons are accelerated to high energy by electric fields at low pressure, their temperature T_e is generally much higher than that of neutral molecules and ions, i.e., they work in a non-thermal equilibrium state. Therefore, such plasma has been used widely as a reactive plasma source not only for thin-film deposition [1.8–11] but also for surface modification [1.12–14] and dry etching [1.15–17]. However, the low density of gas molecules leads to the low density of electrons. Consequently, the plasma processes at low pressure take a long time. Although it has become easy to get

Table 1.2 Constants A and B of various gas [1.23].

Gas	A $\mathrm{cm^{-1}kPa^{-1}}$	B V/cm/kPa	E/p* Validity Range V/cm/kPa
Air	112.8	2744.4	751.9 - 6015.0
N_2	90.2	2571.4	751.9 - 4511.3
H_2	38.3	1043.6	150.4 - 4511.3
He	22.6	255.6	150.4 - 1127.8
Ne	30.1	751.9	751.9 - 3007.5
Ar	105.3	1353.4	751.9 - 4511.3
Kr	127.8	1804.5	751.9 - 7518.8
Xe	195.5	2631.6	1503.8 - 6015.0

high electron density in the low-pressure plasma by using radio-frequency discharge [1.18, 19], hollow-cathode effect [1.20, 21] and so on, the cost of building and maintaining a hypobaric environment is enormous. Additionally, it takes much time and many procedures to transfer specimens into and from a vacuum chamber. Accordingly, to achieve a convenient and low-cost process, it is necessary to drive plasmas at around atmospheric pressure.

At high pressure, the sustaining voltage of plasmas becomes higher than that of low-pressure plasmas because collisions among electrons and gas molecules occur frequently. F. Paschen studied the breakdown voltage V_b of parallel plates in a gas as a function of pressure p and characteristic dimension d, and found the law of breakdown voltage, which was named Paschen's law in 1889 [1.22]. The breakdown voltage is described by the equation:

$$V_\mathrm{b} = \frac{Bpd}{\ln \dfrac{Apd}{\ln(1 + 1/\gamma)}}, \tag{1.1}$$

where the constants A and B depend on the gaseous composition, as listed in Table 1.2, and γ is

*Although the reduced electric field E/p is generally expressed in V/cm/Torr (1 Torr ≈ 0.133 kPa), it is expressed in V/cm/kPa in this dissertation.

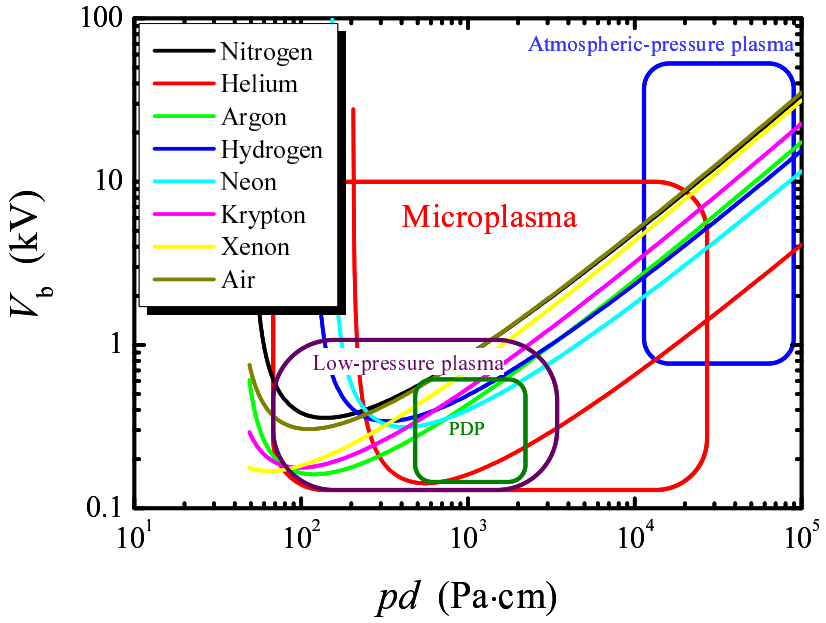

Figure 1.2 Schematic diagram of Paschen curve as a function of the product of pressure p and characteristic dimension d at secondary electron emission coefficient γ of 0.01 [1.23].

the secondary electron emission coefficient of the electrode. Figure 1.1 shows the plots of V_b in various gases against the product of p and d [1.23]. Since d in the plasma processing is generally from several mm to several cm, the higher p becomes, the higher V_b becomes in various kinds of gas shown in Fig. 1.1. In other words, in order to generate a plasma at atmospheric pressure, much higher voltage is required. Also, the plasma is prone to localize spatially and temporally, and to be unstable because the mean free path of electrons is very short (about 10^{-5} cm) [1.23], i.e., it is difficult for the energetic electrons to diffuse over the surrounding area while keeping their high energy.

If excessive electrical power is given, the plasma can easily reach a condition of thermal equilibrium and become an arc discharge due to their high collision frequency. In the arc discharge, a majority of electrons are produced by thermionic electron emission and electron field emission. Since the gas temperature T_g is 10^3 - 10^4 K, it has been applied to metallic processing such

as meltdown and welding of metal, metal treating, and thermal spraying of metal [1.24–26]. Consequently, the technology of plasma processing at atmospheric pressure had not been extensively developed for a long period up until the late 20th century. However, in 1988, Okazaki *et al.* suggested that a glow plasma could be achieved at atmospheric pressure using dielectric barrier discharges (DBDs) [1.27, 28]. This suggestion gained international attention and prompted a great deal of active research on atmospheric-pressure glow-like discharges (APGDs). Finally, the first atmospheric-pressure plasma CVD system was demonstrated by SEKISUI Chemical Co., Ltd. at SEMICON Japan 2000. In this system, pulsed voltages are applied to parallel-plate electrodes placed several mm apart from each other to sustain glow discharges. The deposition rate was very high, e.g., the deposition rate of SiO_2 was about 200 nm/min, and the film quality was not that different from the film deposited by conventional methods.

In 2003, Tachibana propounded the idea of “microplasma” and organized the research project on “Generation of micro-scale reactive plasmas and development of their new application” (short title: Microplasma) [1.30, 31], which was one of the programs of The Specific Research on Priority Areas for five years under the financial support of a Grant-in-Aid for Scientific Research from the Japanese Ministry of Education, Culture, Sports, Science and Technology (MEXT). Generally, plasmas maintain electroneutrality for the entire region. The value which expresses the electroneutrality condition is Debye length λ_D:

$$\lambda_D \equiv \sqrt{\frac{\varepsilon_0 k_B T_e}{n_e e^2}}. \tag{1.2}$$

Here, ε_0 is the permittivity in vacuum, e is the elementary charge, k_B is Boltzmann coefficient, and n_e and T_e are the density and temperature of electrons, respectively. If the characteristic

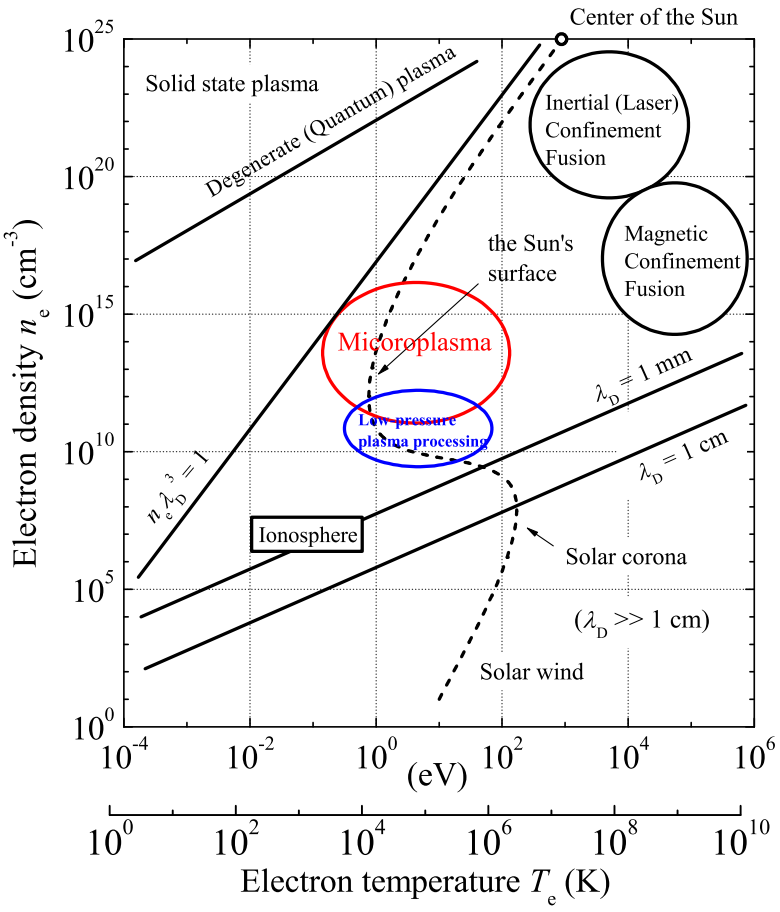

Figure 1.3 Classification of various kinds of plasmas in the nature and industry due to their electron temperature T_e and density n_e [1.29].

size of the plasma is smaller than λ_D, the plasma cannot maintain its electroneutrality. In other words, the size of the plasma is limited by λ_D, e.g., glow discharges at low pressure, which are used in conventional plasma processing, have to be more than 1 mm, as shown in Fig. 1.3 [1.29]. In contrast, microplasmas, whose size ranges several mm to μm, are generated at atmospheric pressure or higher.

In recent years, the media where plasmas are generated has begun to extend from gas phase to liquid and supercritical fluid phase as shown in Fig. 1.4. Scaling down *d* makes it possible to

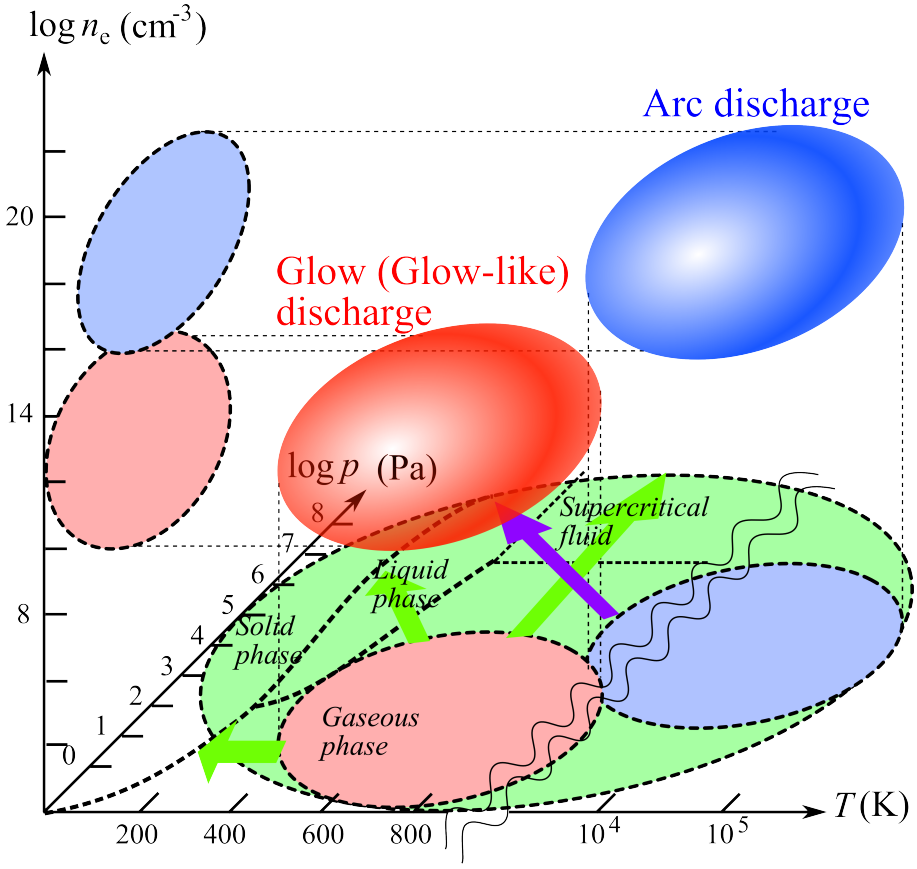

Figure 1.4 Extended range of media in which plasmas are produced, on the phase diagram of CO_2 as an example.

generate plasmas i.e., microplasmas in the dense media as Fig. 1.1 shows. The plasma in liquid phase and the reactions at the interface of gas phase and liquid phase can offer key advantages for plasma processing, such as nanoparticle synthesis [1.32, 33], pollution prevention [1.34–36] and bacteria inactivation [1.37]. Moreover, discharges in a supercritical fluid have been investigated in both practical and theoretical work [1.38–42]. In a supercritical fluid, the breakdown voltage of plasmas become lower than the value of the conventional Paschen curve because the particles in the supercritical fluid form clusters and the apparent density becomes lower. Additionally, plasmas whose gas temperature is in the cryogenic range (cryoplasma) have been investigated because they can effectively reduce the side etching of a nanostructured silicon

trench in a micro-electro-mechanical system (MEMS) [1.43, 44]. As seen above, microplasma technology is opening the door to new scientific and industrial fields of plasmas.

1.2 Atmospheric-Pressure Glow-like Discharges

Recently, atmospheric-pressure glow-like discharges (APGDs) have been investigated throughout the world because they can be generated without vacuum systems, leading to lower-cost fabrication. The plasma can be applied to many applications such as controlling the hydrophilicity and hydrophobicity of organic and inorganic materials [1.45, 46], synthesizing new materials [1.47–49], and killing bacteria and sterilizing [1.50, 51].

APGDs have their roots in A. von Engel *et al*'s successful generation of a glow discharge using a cold cathode at atmospheric pressure [1.52]. However, the plasma that Engel *et al*. generated was a spatially localized and one-dimensional plasma, although it had a negative glow, a Faraday dark space, and a positive column in the manner of a low-pressure plasma. APGDs started receiving considerable attention after S. Okazaki *et al.* suggested an APGD using a DBD in helium in 1988 [1.27, 28]. This DBD has been widely used for ozonizers, ionizers, excimer lamps, surface modification, and sterilization. Okazaki *et al.* obtained a two-dimensional and pulsed glow discharge, and the detailed conditions of this plasma were as follows.

1. An insulating layer was inserted between electrodes.
2. AC voltage with a frequency of more than 1 kHz was applied to the electrodes.
3. Helium, or any gas diluted in a large amount of helium, or argon with a small addition of ketone, was used as a discharge gas.

The insulating layer not only protects the electrodes against ion bombardments but also plays an important role in sustaining the plasma. Charge accumulation on its surface creates an electric potential that opposes the applied voltage and, as a result, terminates increment of the discharge current and prevents the glow-to-arc transition. At the same time, the surface charge accumulated during one half period aids the discharge breakdown in the next half cycle of the applied voltage. Regarding its discharge mechanism, there have been various investigations by experiment and numerical calculation, and many research groups have reported mechanisms that can sustain a glow discharge at atmospheric pressure. F. Massines *et al.* reported that a glow-like discharge can also be realized in nitrogen at atmospheric pressure, and they showed by experiment and numerical calculation that it is not a glow discharge but a Townsend discharge and that nitrogen metastable molecules play a prominent role in maintaining the nitrogen plasma [1.53–55]. Y. B. Golubovskii *et al.* demonstrated one-dimensional and two-dimensional simulations of APGDs including interactions between the charged particles and the dielectric surface, and suggested that the homogeneous plasma in nitrogen is a Townsend discharge [1.56–58]. U. Kortshagen *et al.* suggested that the Penning reaction of helium metastable atoms and the nitrogen molecules of impurities play important roles in sustaining the glow discharge with helium, and they also found that the maximum values of the densities of electrons and helium metastable atoms are on the order of 10^{10} cm^{-3} by two-dimensional spatiotemporal analysis of plasma emissions and one-dimensional simulation of the fluid flow model [1.59, 60].

In recent years, research has shown that it is important to control discharges spatiotemporally in order to generate and maintain APGDs while preventing the glow-to-arc transition. Accordingly, various methods to generate APGDs, such as controlling of gas flows [1.61–63] and applying short pulse voltages [1.64, 65], have been suggested besides DBDs. With this

background, the “microplasma” concept was put forward by K. Tachibana [1.30, 31].

1.3 Microplasma Technology

As mentioned above, the product of p and d determines the breakdown voltage. Therefore, when we try to generate plasmas at atmospheric pressure, it is reasonable to scale down d from mm to μm sizes. Moreover, there is a novel and interesting field spreading between traditional plasma area and exotic area, which contains warm dense matters. Figure 1.5 shows the characteristic features of microplasmas in a plane of spatial size d and electron density n_e [1.30, 66]. It is seen that microplasmas, which are in mezzo-exotic area, are discriminated from traditional plasmas, in which n_e is typically less than 10^{13} cm^{-3} since the operating gas pressure is in the range from 0.1 to 100 Pa. And, in mezzo-exotic area, there are some fruitful applications of microplasmas, such as MEMS tools, EM wave control devices, and biomedical processing.

One of the most important concepts of microplasmas is to control plasma-production spatiotemporally. That is, the plasma-production is controlled spatially by regulating the concentration and the volume of the medium where the plasma is generated, and by devising the electrode structure. And, by changing the waveform of the applied voltage, the temporal behavior of plasmas is determined. These lead to a high degree of freedom for the plasma parameters, such as electron density, electron temperature, gas temperature and so on, as shown in Fig. 1.6 [1.30, 66]. From this aspect, plasma jets, whose locality was controlled by the media, are considered types of microplasmas. Microplasmas combine the potential of low-temperature plasmas with the advantages of locality. The plasmas create a highly reactive environment that contains electrons, ions, excited species, radicals, and photons. Indeed, microplasmas present

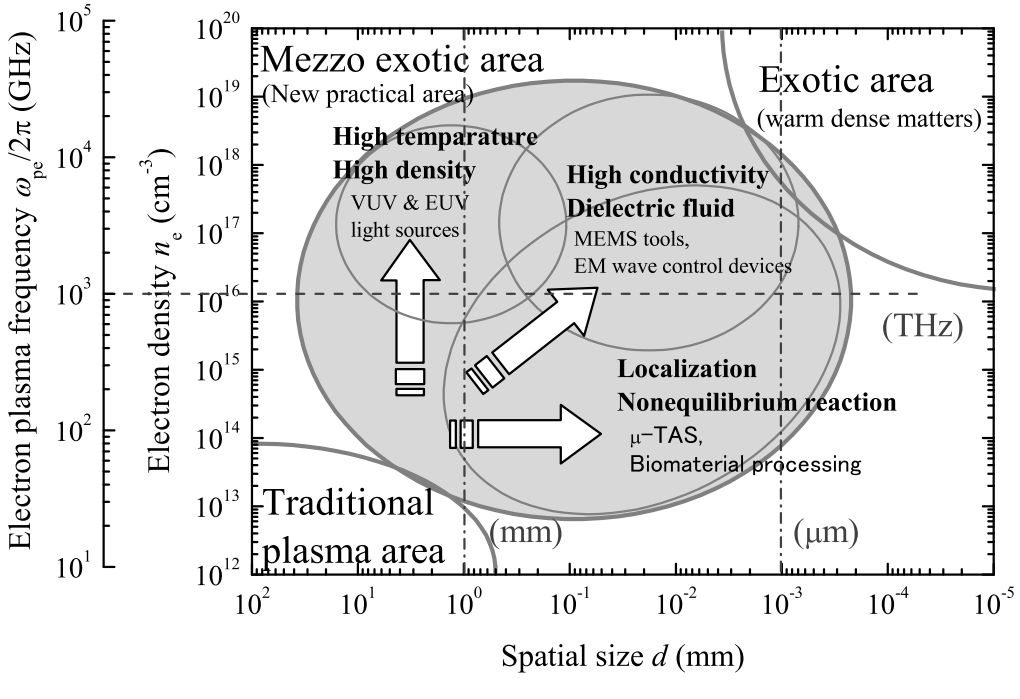

Figure 1.5 Characteristic area of microplasmas in a plane of spatial size d and electron density n_e [1.30, 66].

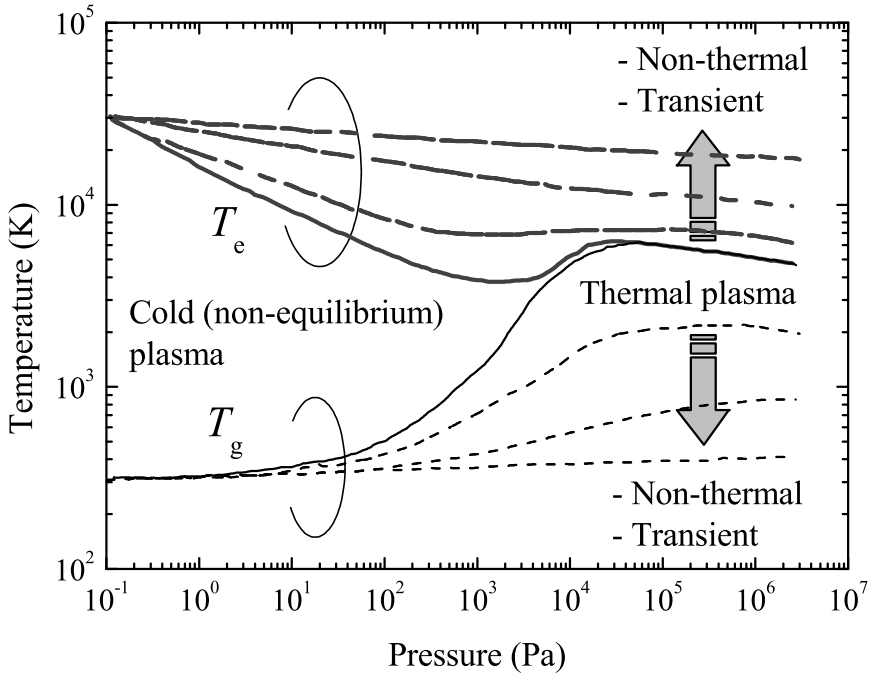

Figure 1.6 Pressure dependence of electron temperature T_e and gas temperature T_g [1.30, 66].

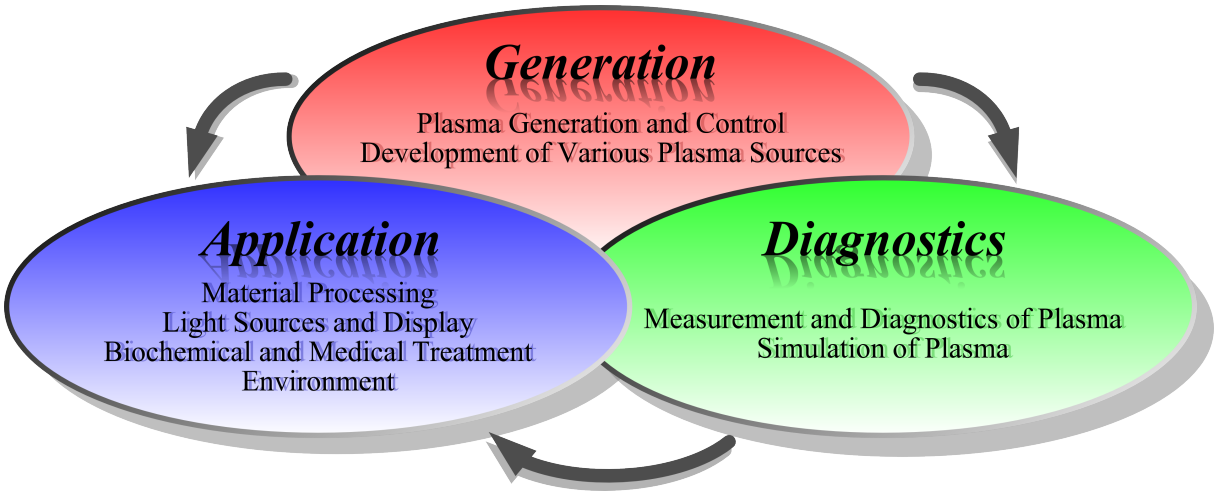

Figure 1.7 Key scientific fields of industrial plasmas, such as generation, diagnostics, and applications.

a new field in plasma physics that is receiving growing attention for its potential economic and technological impact in many scientific disciplines [1.30, 31, 66–68].

In such small microplasmas, it becomes possible to make the residence time of source gas very short at a moderate gas flow rate. By using pulsed voltages, of which the pulse width is shorter than the electron energy relaxation time, the lighting time of the plasma can also be short. As a result, it is possible to maintain a non-thermal equilibrium state. Moreover, we can obtain high densities of electrons and ions even if the degree of ionization is low. The smallness provides additional freedom in actual usage: a microplasma can be used as a single unit, for such purposes as micro-fabrication and micro-chemical analysis [1.69–72], or, otherwise, a group of microplasmas can be used in an integrated array, such as a plasma display panel (PDP) [1.73–75], an electromagnetic-wave control device [1.76–79], and a large-area-process plasma source [1.80–82]. Here, we discuss the key technologies of microplasmas, such as generation, diagnostics, and application of plasmas. These technologies are closely related to each other as shown in Fig. 1.7.

1.3.1 Generation Methods

There are many ways to generate microplasmas, and the methods can be distinguished by the driving frequency of the power sources from DC to GHz. In DC discharge mode, the hollow cathode (HC) type has been developed by Schoenbach's group for miniaturized structures and integrated assemblies [1.83]. The structure they suggested is a simple metal-insulator-metal sandwiched structure with a hole of a few tens to hundreds of micrometers in diameter. This structure allowed electrons to perform a pendulum motion in the cathode area in order to increase the ionization rate, which is called the hollow cathode effect.

In the pulsed discharge mode, the DBD configuration is often used, in which both or at least one of the electrodes is covered with insulating materials as shown in Fig. 1.8. Structure (a) is similar to the structure Okazaki *et al.* used to generate APGDs for the first time, and structures

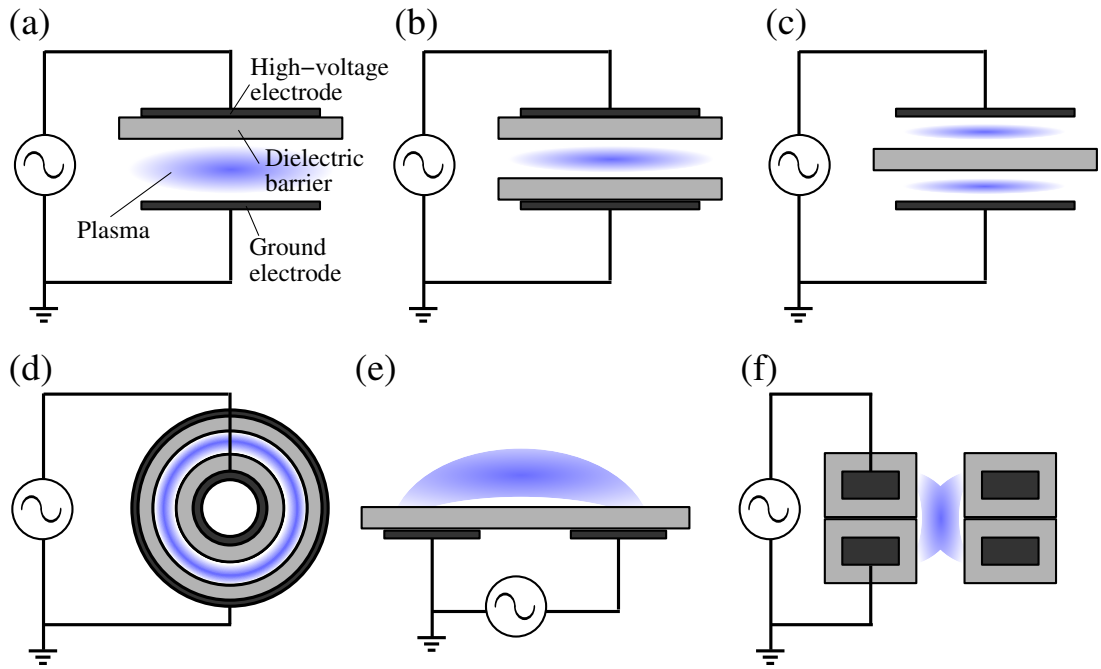

Figure 1.8 Some examples of electrode configurations of microdischarge cells in DBD schemes.

(b) and (c) are variations of (a). Type (d) is applied to excimer lamps. The outer dielectric barrier also serves as a reactor. Type (e) uses surface discharges and is applied to a commercial PDP. Structure (f) is a coaxial type, in which the plasma is generated between the upper and lower electrodes. In this configuration, the directions of electric fields and gas flows are the same. This configuration is easy to be applied to material processing because it is possible to extend the plasma by using an auxiliary electrode or gas flow and the source gas can be fed vertically to the electrode plane through the hole.

1.3.2 Diagnostics of Microplasma

Parameters characterizing microplasma properties are the electron density n_e, the electron temperature T_e, the gas temperature T_g, the electric field E, and so on. Furthermore, microplasmas contain a great deal of active species, such as radicals, excited molecules, and ions. In order to understand the reactions in microplasmas, it is necessary to measure the space-time distribution of the plasma parameters. However, when we diagnose microplasmas, it is difficult to use a Langmuir probe, which is a common method for measuring the parameters of low-pressure plasmas, due to their smallness and the collisional effects in the probe sheath region. Thus, for measurement of the plasma parameters of microplasmas, laser-aided and electromagnetic-wave-aided diagnostics can be useful methods.

Optical Emission Spectroscopy

The simplest spectroscopic method to diagnose plasmas is optical emission spectroscopy (OES). The spectra from plasmas include the information of transition states of active species, as shown in Fig. 1.9 [1.84]. The electron impact excitation of the ground state of atoms and

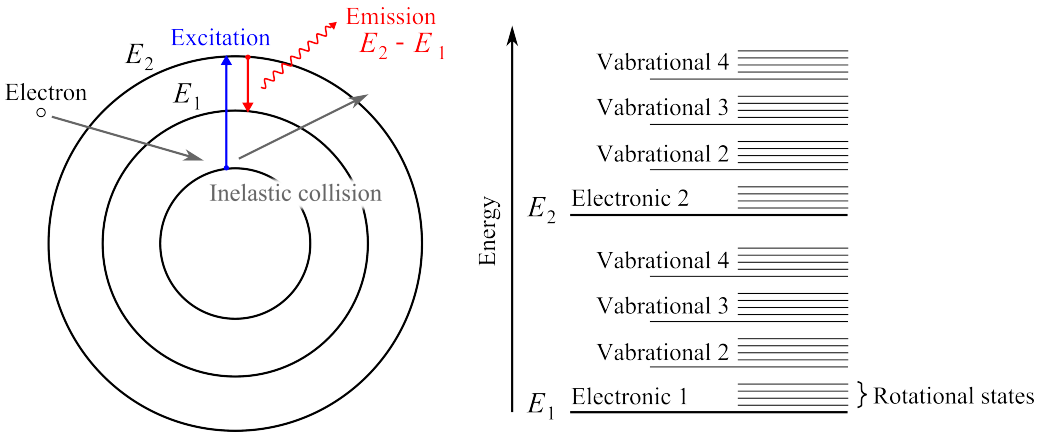

Figure 1.9 Schematic of typical photon emission process of electron impact excitation and energy levels of a molecular [1.84].

molecules to an excited state of them is followed by subsequent emission to a lower energy level. In the case of molecules, there are vibrational and rotational states in addition to electronic states. The spectral lines are broadened by various factors such as natural broadening, collisional pressure broadening, Doppler broadening, Zeeman broadening, and Stark broadening. Traditionally, the Doppler broadening of the spectra has been used for measurement of T_g, and the Stark broadening can be used for estimation of n_e and T_e. At higher pressure, collisions of particles also broaden the spectral lines (collisional pressure broadening), but such broadening is not usually observed in the discharges at low pressure. We should consider the influence of the collisional pressure broadening in high-pressure plasmas. On the contrary, since particle-particle collisions frequently occur, there is an advantage of being able to regard the rotational temperature of nitrogen and other molecules obtained from their rotational spectrum distribution as T_g [1.85]. Thus, OES is simple and useful method. However, it should be noted that we can obtain only the information of given particles not in lower level but in higher one from OES spectra.

Laser-aided Diagnostics

The methods of laser-aided diagnostics are classified into laser scattering, laser interferometry, laser absorption spectroscopy, and laser-induced fluorescence.

Laser Thomson scattering (LTS) can be cited as a typical example of laser scattering methods [1.86, 87]. In LTS method, the plasma parameters can be measured at 10 μm and 1 ns resolution by choosing a suitable laser wavelength and power. In this method, by analyzing the spectra of scattering light from free electrons, we can obtain localized T_e, ion temperature T_i, and n_e. Laser interferometry can be applied to the measurement of n_e and the collision frequency ν_m. Although a microwave method and THz time-domain spectroscopy can be used for the same measurement, the advantage of laser interferometry is high spatial resolution by using laser lights [1.88]. Laser absorption spectroscopy is used for measuring the density of metastable molecules [1.89, 90]. From the attenuation of the incident laser lights, whose energy is corresponding to the excitation energy of the molecules in the plasma, we can calculate the density of various kinds of metastable molecules by selecting the wavelength of the laser lights. Laser-induced fluorescence gives us a three-dimensional distribution of radicals, excited species and ions by crossing the directions of the incident laser and a detector [1.91–93]. This method is used to measure the fluorescence from the particles selectively excited by the incident laser lights. However, some techniques are required to estimate the absolute density of the particles.

Electromagnetic-wave-aided Diagnostics

The electromagnetic-wave-aided diagnostics uses the macroscopic interactions between the waves and plasmas. The elctromagnetic waves are used in wide-ranging applications, as shown in Fig. 1.10. In particular, microwaves have been studied intensively because their antennae can

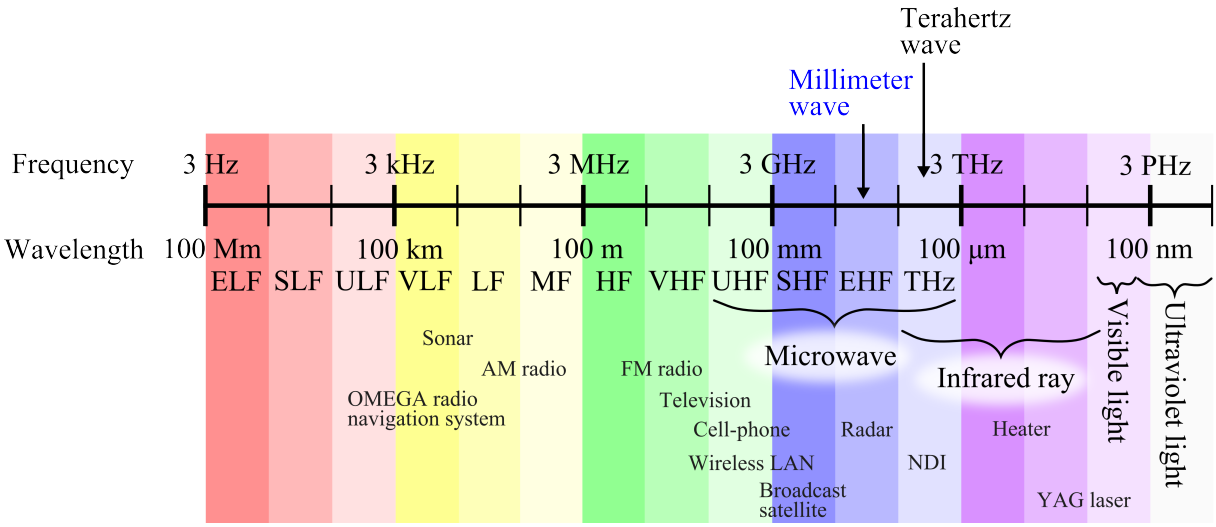

Figure 1.10 Classification of electromagnetic waves and their use due to their frequency.

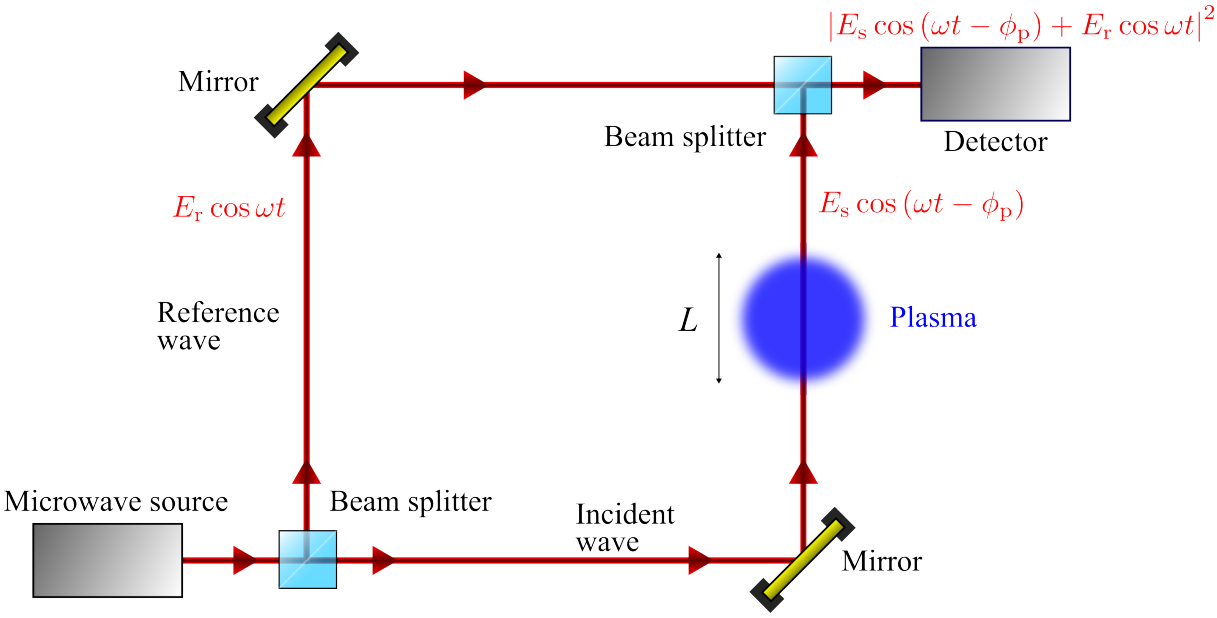

Figure 1.11 Schematic diagram of typical microwave interferometry measurement.

be downsized due to the wavelength. Microwave interferometry measurement is well known as a method that can diagnose n_e in plasmas by detecting the phase shift of microwaves [1.94, 95]. Figure 1.11 shows the schematic diagram of the principle of interferometry. The original electromagnetic wave is separated into two paths, where the wave in one of the paths is the reference wave, while the wave in the other path enters the plasma whose length is L, which gives a phase shift ϕ_p. After merging the two waves at the interferometer exit, we obtain the signal containing the information of ϕ_p expressed by the following equation:

$$\phi_p = k_0 \int_L \left(1 - N_p\right) dx, \tag{1.3}$$

where k_0 is the wave number of the electromagnetic wave in vacuum, and N_p is the refractive index of the plasma. N_p is described as follows:

$$N_p = \sqrt{1 - \frac{\omega_{pe}^2}{\omega^2}}. \tag{1.4}$$

Here, ω_{pe} and ω are the electron plasma frequency and the angular frequency of the electromagnetic wave, respectively. This method gives us the information of ω_{pe}, which is defined by

$$\omega_{pe} \equiv \sqrt{\frac{n_e e^2}{\varepsilon_0 m_e}}, \tag{1.5}$$

where m_e is the electron mass. From this relation, we can calculate the electron density n_e.

Figure 1.12 shows the wave dispersion relation in a collision-less bulk plasma in the absence of external magnetic fields. As shown in Fig. 1.12, ω_{pe} determines the response of the plasma to an external electric field of a wave at angular frequency ω. That is, if $\omega \gg \omega_{pe}$, the electro-

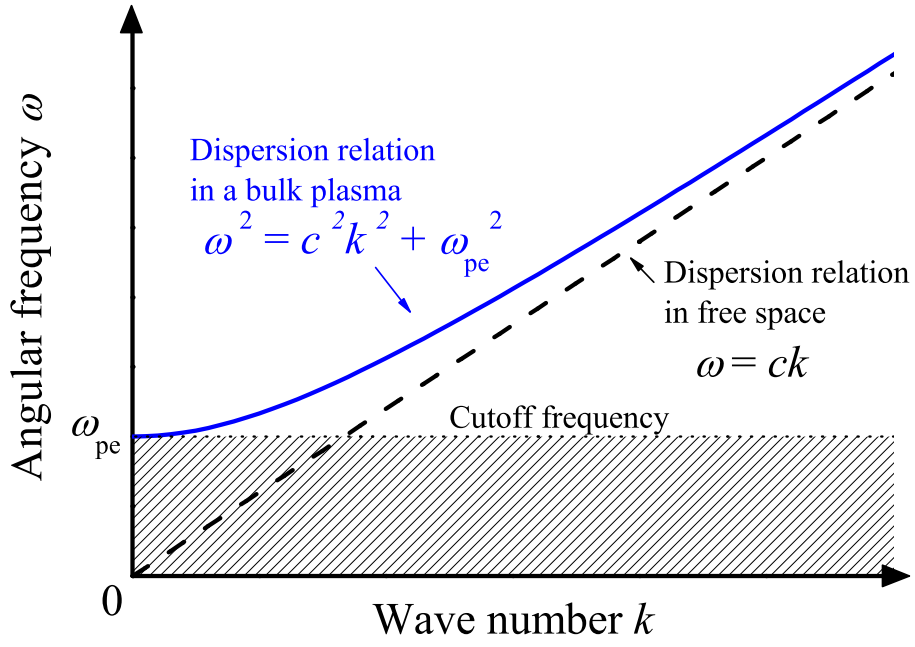

Figure 1.12 Wave dispersion relations in collision-less bulk plasma in the absence of an external magnetic field and in free space. c is the velocity of light.

magnetic wave can propagate through the plasma as if it were free space. On the other hand, if $\omega \ll \omega_{pe}$, the electromagnetic wave cannot go through it but is reflected by the plasma as if it were a metal. Those effects take place in the collision-less plasmas that have unlimited length. When collisional plasmas have finite length, the wave is not reflected perfectly, its phase changes due to the real part of the refractive index of the plasma, and its amplitude attenuates through the plasma via elastic collisions of electrons with gas particles. The microwave transmission method is based on this phenomenon [1.94–96]. Generally speaking, the electron density in microplasmas is 10^{12} - 10^{16} cm^{-3}, i.e., 10 GHz - 1 THz in the electron plasma frequency. Additionally, since the size of microplasmas is in the mm to μm range, it is preferable that the wave for the measurement is in the millimeter-wave to terahertz range.

1.3.3 Advanced Plasma Processing by Using Microplasmas

Fundamental features of plasmas are luminescence, reactivity, and conductive and dielectric properties. On the other hand, characteristic properties of microplasmas are their locality, brevity, high densities of electrons and ions, non-thermal equilibrium, high density of the media, and so on. Furthermore, by selecting the usage, such as single unit and assembly, there are various applications of microplasmas as shown in Fig. 1.13 [1.66]. For example, a PDP is a display device exploiting the properties of luminescence, locality, brevity, and assembly. Also, the integrated microplasmas can be effectively applied to large-area light sources and material processing. Generally speaking, compared with a singular large-area plasma, an assembly of microplasmas can be obtained in wider ranges of driving parameters, such as driving frequency, voltage, and pressure. That is, even if we use air and gases containing water vapors or source materials as a discharge gas, it is possible for an assembly of microplasmas to obtain apparently homogeneous plasmas over a wide range of driving conditions. In addition, by aligning microplasmas periodically, they also work as photonic crystals and are able to control electromagnetic waves [1.76–79].

Moreover, one of the possible applications of microplasmas is plasma jets. In the case of material processing, a plasma jet that can extend a thin-shaped and long plasma plume outside of an enclosed area is able to be a useful tool for localized processes. Therefore, various kinds of plasma jets have been investigated energetically [1.65, 70, 97–104]. At the same time, materials treated by plasma jets are not only industrial materials but also bioengineered materials and living bodies, and the technology of plasma processing is still expanding within the field of health and medical treatment [1.51, 105, 106], since a plasma jet is in a non-thermal equilibrium

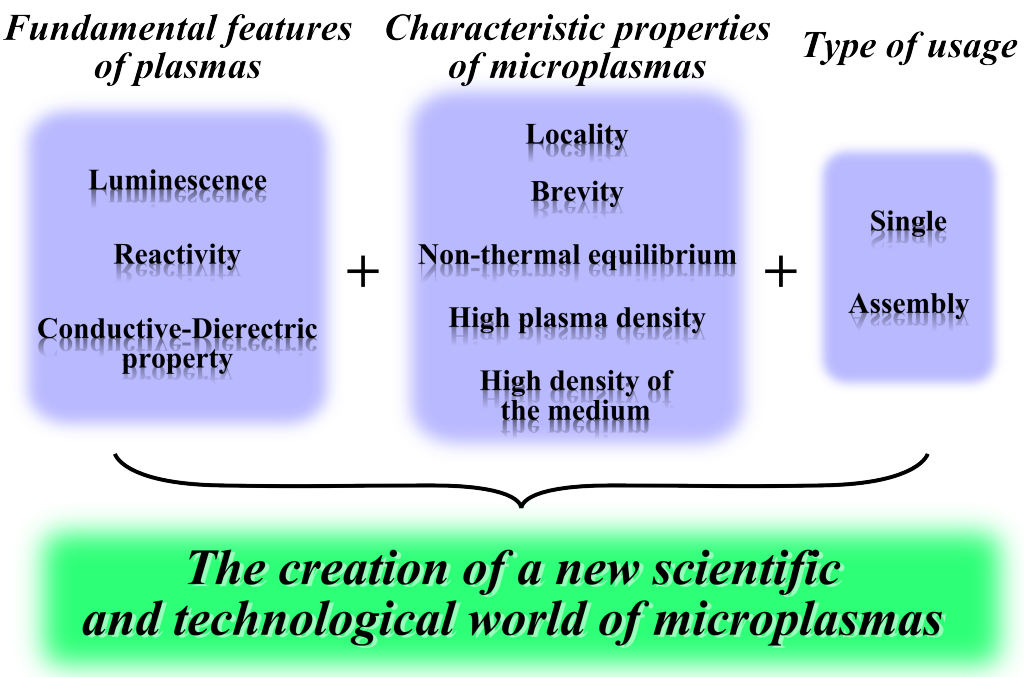

Figure 1.13 Creation of new science and technology for microplasma by combining its properties and usage [1.66].

state and has high reactivity. In addition, by selecting metalline liquids as the medium of the plasma, it is possible to synthesize metallic nanoparticles, which are currently in the spotlight as new materials [1.33, 48].

Naturally, there is also the possibility of improving traditional PE-CVD by microplasma technology. With the miniaturization of semiconductor components, large-area processes have become no longer indispensable in semiconductor and optoelectronic industry in recent years. Microplasmas can deposit films at high speed in a small area, and they are suitable for bottom-up processes that build electronic devices from tiny components. In this way, a high-speed and ecological process can be realized by using microplasma technology.

1.4 Objective of This Study

As mentioned above, microplasmas have extended the field of plasma processing. Moreover, in the field of conventional semiconductor manufacturing, microplasmas raise considerable practical interest due to their characteristics such as high density of active species, reactivity, locality, and non-thermal equilibrium. Using these characteristics, various research efforts have been progressing toward the development of high-speed and convenient plasma processing [1.70, 101, 107–109]. PE-CVD is taken for instance. Heretofore, PE-CVD has been used mainly in low-pressure regions ranging from 0.1 Pa to 10 kPa, and commonly has the electron density of the order of 10^{11} cm^{-3} depending on the discharge mode and input power. Compared with thermal CVD, PE-CVD at low pressure can decrease the substrate temperature and is suitable for semiconductor processing. However, the density of active species is low even if the ionization degree is enhanced since the gas pressure is low, and this leads to a low deposition rate. On the other hand, in the case of PE-CVD at atmospheric pressure, the electron density is in the range from 10^{12} to 10^{16} cm^{-3}, even if the ionization degree is low, and the deposition rate becomes higher than that at low pressure.

The objective of this study is to make plasma processing high-speed and convenient by using microplasmas originating from coaxial dielectric barrier discharges at atmospheric pressure. The coaxial dielectric barrier discharge has the electrode structure shown in Fig. 1.8(f). In this structure, since the directions of electric fields and gas flows can be the same, plasmas can be draw out by either electric fields or gas flows. And, the metal electrodes are covered with dielectric material, which protects the electrodes against wear. These features are highly preferable for plasma processing. Moreover, as mentioned above, by selecting the type of

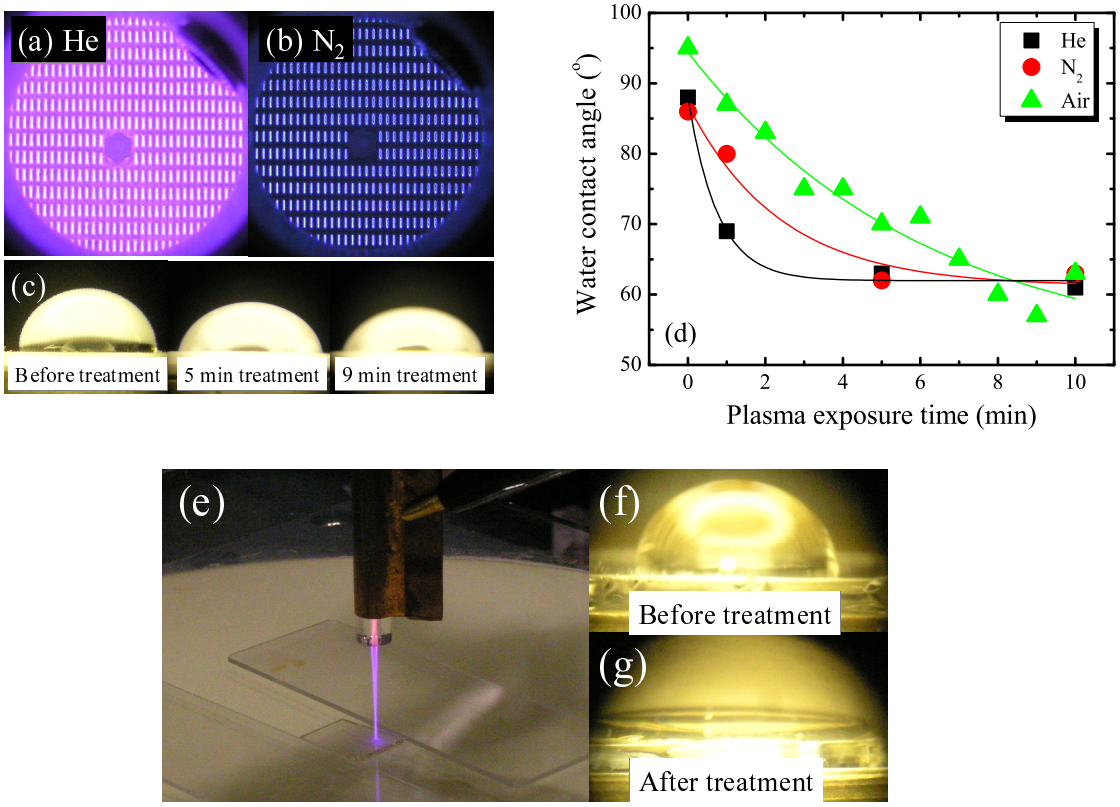

Figure 1.14 Surface modification of polytetrafluoroethylene (PTFE) sheets by microplasma array, and that of polyimide films by APPJ: visible emissions in microplasma array in helium (a) and nitrogen (b), wettability change in PTFE sheets treated by microplasma array in air with different irradiation times of 0 (untreated), 5, and 9 min (c), experimental results of contact angle of water droplet after plasma treatment as a function of plasma exposure time in three kinds of gases (d), photograph of APPJ during treatment of a polyimide film (e), and wettability change in polyimide films treated by APPJ before treatment (f) and after treatment with a scanning speed of 1 mm/s (g) [1.110].

usage, such as single and assembly, the plasma source can be applied to both maskless and large-area processes. Therefore, two types of plasma sources: a microplasma array and an atmospheric-pressure plasma jet (APPJ) have been used in previous study, and applied to surface modification as shown in Fig. 1.14 [1.110].

In this dissertation, the characteristics of those plasmas are diagnosed to clarify the discharge mechanism of coaxial dielectric barrier discharges. Furthermore, the APPJ is applied to PE-CVD in order to realize a high-speed and convenient method for deposition of oxide materials.

In Chapter 2, the fundamentals of the microplasma array and the APPJ are investigated. For plasma processes, it is necessary to extend the plasmas to the reaction field. Therefore, in this chapter, the plasma is effused externally by an electric field and by a gas flow, and is measured its length. Furthermore, the effect of helium gas flow and the discharge mechanism in these plasma sources are discussed.

In Chapter 3, the electron density in nitrogen plasma generated in the microplasma array at atmospheric pressure is diagnosed by using a millimeter-wave transmission method. Nitrogen is a reasonable candidate as an inert gas, so the plasma parameters in nitrogen should be investigated. However, in general, nitrogen plasma at atmospheric pressure tends to be filamentary, and it is difficult to measure the electron density. Therefore, the microplasma array, which is an assembly of small plasmas, is used to measure the electron density. Then the validity of this experimental results are assessed with a simple particle balance model. In addition, the effect of small admixtures of H_2O and O_2 into nitrogen discharges at atmospheric pressure is also studied for plasma processing.

In Chapter 4, In order to investigate the effect of accumulated charge on a substrate surface in deposition of oxide films with the APPJ, the discharge current to the copper substrate connected to a variable capacitor in series is measured. To analyze the behavior of the plasma jet, the equivalent circuit of this system is considered and the validity of the supposition that the accumulated charge restricts the deposition rate is verified.

In Chapter 5, as one of applications of the APPJ, the experimental study on the PE-CVD of SiO_2 films from tetraethoxysilane (TEOS) is presented. In this study, three different configurations: (a) a coaxial type, (b) a crossed type with a vertical plasma jet and a tilted TEOS supply, and (c) another crossed type with the reversed arrangement are attempted. Then, the reactions

in gas phase are discussed with a simplified global model.

In Chapter 6, PE-CVD using the APPJ is applied to deposition of ZnO films. Using vaporized bis(octane-2,4- dionato)zinc flow crossed by the plasma jet, high-speed deposition of ZnO as transparent semiconductor-like films is realized. Then, the optical and electrical properties of the films are discussed.

Finally, in Chapter 7, the obtained results from each chapter of this dissertation are summarized, and future prospects are offered.

References

[1.1] J. Hopwood: Plasma Sources Sci. Technol. **1**, 109 (1992).

[1.2] R. C. Chittick, J. H. Alexander and H. F. Sterling: J. Electrochem. Soc. **116**, 77 (1969).

[1.3] S. C. Deshmukh and E. S. Aydil: J. Vac. Sci. Technol. A **13**, 2355 (1995).

[1.4] A. M. Wróbel, A. Walkiewicz-Pietrzykowska, S. Wickramanayaka and Y. Hatanaka: J. Electrochem. Soc. **145**, 2866 (1998).

[1.5] A. Granier, C. Vallée, A. Goullet, K. Aumaille and G. Turban: J. Vac. Sci. Technol. A **17**, 2470 (1999).

[1.6] M. Kamo, Y. Sato, S. Matsumoto and N. Setaka: J. Cryst. Growth **62**, 642 (1983).

[1.7] S. Matsuo and M. Kiuchi: Jpn. J. Appl. Phys. **22**, L210 (1983).

[1.8] K. Tachibana, H. Tadokoro, H. Harima and Y. Urano: J. Phys. D: Appl. Phys. **15**, 177 (1982).

[1.9] M. Shimizu, Y. Matsueda, T. Shiosaki and A. Kawabata: J. Cryst. Growth **71**, 209 (1985).

[1.10] L. L. Tedder, G. Lu and J. E. Crowell: J. Appl. Phys. **69**, 7037 (1991).

[1.11] H. Jia, H. Kuraseko and M. Kondo: J. Appl. Phys. **103**, 024904 (2008).

[1.12] D. T. Clark and T. Fok: Thin Solid Films **78**, 271 (1989).

[1.13] J. E. Gray, P. R. Norton and K. Griffiths: Appl. Surf. Sci. **217**, 210 (2003).

[1.14] C. T. Andrade, R. A. Simão, R. M. S. M. Thiré and C. A. Achete: Carbohydr. Polym. **61**, 407 (2005).

[1.15] Y. W. Chen, B. S. Ooi and G. I. Ng: Opt. Mater. **14**, 223 (2000).

[1.16] S.-M. Gu, D.-P. Kim, K.-T. Kim and C.-I. Kim: Thin Solid Films **475**, 313 (2005).

[1.17] T. Wakayama, T. Suemasu, T. Kanazawa and H. Akinaga: Jpn. J. Appl. Phys. **45**, L569

(2006).

[1.18] C. M. Braams, W. J. Schrader and J. C. Terlouw: Nucl. Instr. Meth. **4**, 327 (1959).

[1.19] J. L. Wilson, J. B. O. Caughman II, P. L. Nguyen and D. N. Ruzic: J. Vac. Sci. Technol. A **7**, 972 (1989).

[1.20] C. C. V. Voorhis and A. G. Shenstone: Rev. Sci. Instrum. **12**, 257 (1941).

[1.21] T. Callegari, F. Gegot, L. C. Pitchford, J. Galy and J. P. Boeuf: IEEE Trans. Plasma Sci. **33**, 384 (2005).

[1.22] F. Paschen: Ann. Physik **37**, 69 (1889).

[1.23] E. Nasser: *Fundamentals of Gaseous Inonization and Plasma Electronics* (Wiley, New York, 1971).

[1.24] H. S. Gecim and P. K. John: Int. J. Electronics **71**, 977 (1991).

[1.25] J. Zhang and A. Kobayashi: Vacuum **80**, 1185 (2006).

[1.26] T. Iwao and M. Yumoto: IEEJ Trans. Electr. Electron. Eng. **1**, 163 (2006).

[1.27] S. Kanazawa, M. Kogoma, T. Moriwaki and S. Okazaki: J. Phys. D: Appl. Phys. **21**, 838 (1988).

[1.28] S. Okazaki, M. Kogoma, M. Uehara and Y. Kimura: J. Phys. D: Appl. Phys. **26**, 889 (1993).

[1.29] M. A. Lieberman and A. J. Lichtenberg: *Principles of Plasma Discharges and Materials Processing* (Wiley, New York, 1994).

[1.30] K. Tachibana: IEEJ Trans. Electr. Electron. Eng. **1**, 145 (2006).

[1.31] K. Tachibana (Project reader): Scientific Research on Priority Area 429 Microplasma Summary Report 2003-2007 FY *Generation of Micro-Scale Reactive Plasmas and Development of Their New Applications* (2008).

[1.32] O. Takai: Pure Appl. Chem. **80**, 2003 (2008).

[1.33] H. Furusho, K. Kitano, S. Hamaguchi and Y. Nagasaki: Chem. Mater. **21**, 3526 (2009).

[1.34] P. Baroch, V. Anita, N. Saito and O. Takai: J. Electrostatics **66**, 294 (2008).

[1.35] O. Sakai, M. Kimura, T. Shirafuji and K. Tachibana: Appl. Phys. Lett. **93**, 231501 (2008).

[1.36] Y. Yang, A. Gutsol, A. Fridman and Y. I. Cho: Int. J. Heat Mass Transfer **52**, 4901 (2009).

[1.37] M. Sato: Plasma Sources Sci. Technol. **17**, 024021 (2008).

[1.38] H. Kikuchi, H. Kubo, T. Tomai and K. Terashima: Thin Solid Films **516**, 6677 (2008).

[1.39] C. Ventosa, D. Rébiscoul, V. Perrut, V. Ivanova, O. Renault and G. Passemard: Micro-electron. Eng. **85**, 1629 (2008).

[1.40] T. Tomai, H. Yui and K. Terashima: Appl. Phys. Lett. **94**, 151501 (2009).

[1.41] T. Maehara, A. Kawashima, A. Iwamae, S. Mukasa, T. Takemori, T. Watanabe, K. Kurokawa, H. Toyota and S. Nomura: Phys. Plasmas **16**, 033503 (2009).

[1.42] E. H. Lock, A. V. Saveliev and L. A. Kennedy: IEEE Trans. Plasma Sci. **37**, 1078 (2009).

[1.43] Y. Noma, J. H. Choi, T. Tomai and K. Terashima: Appl. Phys. Lett. **93**, 101503 (2008).

[1.44] J. H. Choi, Y. Noma and K. Terashima: Plasma Sources Sci. Technol. **18**, 025023 (2009).

[1.45] M. Iwasaki, K. Takeda, M. Ito, T. Yara, T. Uehara and M. Hori: Jpn. J. Appl. Phys. **46**, L540 (2007).

[1.46] T. Wang, C. Wang and Y. Qiu: J. Appl. Polym. Sci. **108**, 25 (2008).

[1.47] Z. Yang, H. Shirai, T. Kobayashi and Y. Hasegawa: Thin Solid Films **515**, 4153 (2007).

[1.48] M. Li, J. Gonzalez-Aguilar and L. Fulcheri: Jpn. J. Appl. Phys. **47**, 7343 (2008).

[1.49] W.-J. Liu, X.-J. Guo, C.-L. Chang and J.-H. Lu: Thin Solid Films **517**, 4229 (2009).

[1.50] N. Abramzon, J. C. Joaquin, J. Bray and G. Brelles-Mariño: IEEE Trans. Plasma Sci. **34**, 1304 (2006).

[1.51] M. Laroussi: IEEE Trans. Plasma Sci. **37**, 714 (2009).

[1.52] A. von Engel, R. Seeliger and M. Steenbeck: Z. Physik **85**, 144 (1933).

[1.53] N. Gherardi, G. Gouda, E. Gat, A. Ricard and F. Massines: Plasma Sources Sci. Technol. **9**, 340 (2000).

[1.54] F. Massines, N. Gherardi, N. Naudé and P. Ségur: Plasma Phys. Control. Fusion **47**, B577 (2005).

[1.55] N. Naudé, J.-P. Cambronne, N. Gherardi and F. Massines: J. Phys. D: Appl. Phys. **38**, 530 (2005).

[1.56] Y. B. Golubovskii, V. A. Maiorov, J. Behnke and J. F. Behnke: J. Phys. D: Appl. Phys. **35**, 751 (2002).

[1.57] Y. B. Golubovskii, V. A. Maiorov, J. Behnke and J. F. Behnke: J. Phys. D: Appl. Phys. **36**, 39 (2003).

[1.58] R. Brandenburg, V. A. Maiorov, Y. B. Golubovskii, H-EWagner, J. Behnke and J. F. Behnke: J. Phys. D: Appl. Phys. **38**, 2187 (2005).

[1.59] L. Mangolini, C. Anderson, J. Heberlein and U. Kortshagen: J. Phys. D: Appl. Phys. **37**, 1021 (2004).

[1.60] P. Zhang and U. Kortshagen: J. Phys. D: Appl. Phys. **39**, 153 (2006).

[1.61] Y. Akishev, O. Goossens, T. Callebaut, C. Leys, A. Napartovich and N. Trushkin: J. Phys. D: Appl. Phys. **34**, 2875 (2001).

[1.62] Y. Akishev, M. Grushin, I. Kochetov, V. Karal'nik, A. Napartovich and N. Trushkin: Plasma Sources Sci. Technol. **14**, S18 (2005).

[1.63] K. Hattori, H. Yamada, T. Kumagai, A. Ando and M. Inutake: Jpn. J. Appl. Phys. **45**, 8246 (2006).

[1.64] K. Takaki, H. Kirihara, C. Noda, S. Mukaigawa and T. Fujiwara: Jpn. J. Appl. Phys. **45**, 8241 (2006).

[1.65] J. L. Walsh and M. G. Kong: Appl. Phys. Lett. **91**, 221502 (2007).

[1.66] K. Tachibana, S. Ishi, K. Terashima and T. Shirafuji (Eds.): *Microplasma* (Ohmsha, Tokyo, 2009) [in Japanese].

[1.67] K. H. Becker, K. H. Schoenbach and J. G. Eden: J. Phys. D: Appl. Phys. **39**, R55 (2006).

[1.68] F. Iza, G. J. Kim, S. M. Lee, J. K. Lee, J. L. Walsh, Y. T. Zhang and M. G. Kong: Plasma Process. Polym. **5**, 322 (2008).

[1.69] T. Yokoyama, S. Hamada, S. Ibuka, K. Yasuoka and S. Ishii: J. Phys. D: Appl. Phys. **38**, 1684 (2005).

[1.70] T. Ideno and T. Ichiki: Thin Solid Films **506-507**, 235 (2006).

[1.71] V. Raballand, J. Benedikt and A. von Keudell: Appl. Phys. Lett. **92**, 091502 (2008).

[1.72] D. Shanmugarajah, D. Ding, Q. Huang, X. Chen, H. Kochat, P. N. Petluru, P. Y. Ayala, A. R. Parker and F. H. Hausheer: J. Chromatogr. B **877**, 857 (2009).

[1.73] J. Meunier, P. Belenguer and J. P. Boeuf: J. Appl. Phys. **78**, 731 (1995).

[1.74] F. Iza, S. S. Yang, H. C. Kim and J. K. Lee: J. Appl. Phys. **98**, 043302 (2005).

[1.75] K. Tachibana, Y. Kishimoto, S. Kawai, T. Sakaguchi and O. Sakai: Plasma Phys. Control. Fusion **47**, A167 (2005).

[1.76] O. Sakai, T. Sakaguchi, Y. Ito and K. Tachibana: Plasma Phys. Control. Fusion **47**, B617 (2005).

[1.77] O. Sakai, T. Sakaguchi, T. Naito, D.-S. Lee and K. Tachibana: Plasma Phys. Control.

Fusion **49**, B453 (2007).

[1.78] O. Sakai and K. Tachibana: J. Phys.: Conf. Ser. **86**, 012015 (2007).

[1.79] T. Naito, O. Sakai and K. Tachibana: Appl. Phys. Express **1**, 066003 (2008).

[1.80] T. Ito, K. Katahira, A. Asahara, S. A. Kulinich and K. Terashima: Sci. Technol. Adv. Mater. **4**, 559 (2003).

[1.81] O. Sakai, Y. Kishimoto and K. Tachibana: J. Phys. D: Appl. Phys. **38**, 431 (2005).

[1.82] O. Sakai, K. Tachibana, K. Tatsugawa, K. Ohishi and R. Inoue: Trans. Mater. Res. Soc. Jpn. **31**, 453 (2006).

[1.83] K. H. Schoenbach, M. Moselhy, W. Shi and R. Bentley: J. Vac. Sci. Technol. A **21**, 1260 (2003).

[1.84] F. F. Chen and J. P. Chang: *Lecture Notes on Principles of Plasma Processing* (Springer, Berlin, 2003).

[1.85] D. M. Phillips: J. Phys. D: Appl. Phys. **9**, 507 (1976).

[1.86] S. Hassaballa, K. Tomita, Y. K. Kim, K. Uchino, H. Hatanaka, Y. M. Kim, C. H. Park and K. Muraoka: Jpn. J. Appl. Phys. **44**, L442 (2005).

[1.87] S. C. Snyder, G. D. Lassahn and J. D. Grandy: J. Quant. Spectrosc. Radiat. Transf. **107**, 217 (2007).

[1.88] T. Matsuoka, T. Fujimoto, K. Tanaka, S. Miyasaka, S. Tajima, K. Fujii, M. Suzuki and M. Tonouchi: Physica C **469**, 982 (2009).

[1.89] K. Tachibana, Y. Kishimoto and O. Sakai: J. Appl. Phys. **97**, 123301 (2005).

[1.90] M. Matsui, K. Komurasaki and Y. Arakawa: Vacuum **83**, 21 (2008).

[1.91] T. Oda, Y. Yamashita, K. Takezawa and R. Ono: Thin Solid Films **506-507**, 669 (2006).

[1.92] K. Urabe, Y. Ito, K. Tachibana and B. N. Ganguly: Appl. Phys. Express **1**, 066004

(2008).

[1.93] S. Reuter, K. Niemi, V. S. von der Gathen and H. F. Döbele: Plasma Sources Sci. Technol. **18**, 015006 (2009).

[1.94] J. D. Swift and M. J. R. Schwar: *Electrical Probes for Plasma Diagnostics* (Iliffe Books, London, 1970).

[1.95] I. H. Hutchinson: *Principles of Plasma Diagnostics* (Cambridge University Press, Cambridge, 1990).

[1.96] M. P. Bachynski and K. A. Graf: RCA Rev. **25**, 3 (1964).

[1.97] M. Teschke, J. Kedzierski, E. G. Finantu-Dinu, D. Korzec and J. Engemann: IEEE Trans. Plasma Sci. **33**, 310 (2005).

[1.98] W. P. Xi Chen and, X. Meng, K. Cheng, D.-Y. Xu and C. Wu: Pure Appl. Chem. **78**, 1253 (2006).

[1.99] V. Léveillé and S. Coulombe: Plasma Process. Polym. **3**, 587 (2006).

[1.100] Y. Sakurai, M. Yeo, H. Shirai, T. Kobayashi and Y. Hasegawa: J. Non-Cryst. Solids **352**, 989 (2006).

[1.101] Y. Shimizu, A. C. Bose, D. Mariotti, T. Sasaki, K. Kirihara, T. Suzuki, K. Terashima and N. Koshizaki: Jpn. J. Appl. Phys. **45**, 8228 (2006).

[1.102] M. Laroussi and T. Akan: Plasma Process. Polym. **4**, 777 (2007).

[1.103] J. F. Kolb, A.-A. H. Mohamed, R. O. Price, R. J. Swanson, A. Bowman, R. L. Chiavarini, M. Stacey and K. H. Schoenbach: Appl. Phys. Lett. **92**, 241501 (2008).

[1.104] Y. Sakiyama, D. B. Graves and E. Stoffels: J. Phys. D: Appl. Phys. **41**, 095204 (2008).

[1.105] S. Coulombe, V. Léveillé, S. Yonson and R. L. Leask: Pure Appl. Chem. **78**, 1147 (2006).

[1.106] E. Stoffels, Y. A. Gonzalvo, T. D. Whitmore, D. L. Seymour and J. A. Rees: Plasma Sources Sci. Technol. **16**, 549 (2007).

[1.107] J. Benedikt, K. Focke, A. Yanguas-Gil and A. von Keudell: Appl. Phys. Lett. **89**, 251504 (2006).

[1.108] H. Yoshiki: Rev. Sci. Instrum. **78**, 043510 (2007).

[1.109] R. Foest, E. Kindel, H. Lange, A. Ohl, M. Stieber and K. D. Weltmann: Contrib. Plasma Phys. **47**, 119 (2007).

[1.110] Y. Ito, K. Urabe, M. Kubo and K. Tachibana: *Proc. 18th Int. Symp. Plasma Chem.* 28P-65 (Kyoto, 2007).

Chapter 2

Fundamental Properties of Coaxial Dielectric Barrier Discharges

2.1 Introduction

Recently, plasma processes by use of atmospheric-pressure glow-like discharges (APGDs) have attracted much interest as an alternative to low-pressure plasma processes because such plasmas can be generated without vacuum chambers. In order to realize APGDs, several methods have been employed, such as dielectric barrier discharges [2.1, 2], hollow cathode discharges [2.3], and so on.

In this chapter, the fundamental properties of coaxial dielectric barrier discharges, which allow us to generate APGDs, are investigated. The coaxial dielectric barrier discharges are applied to plasma processes easily because the gas flow and the electric field are in the same direction. Our group has investigated a microplasma array, which is based on the coaxial dielectric barrier discharges, in helium without extending the plasmas to outside of the hollows [2.4, 5]. However, if this microplasma array is used in material processing, the information on the plasma extending from the hollows to the outside is essential. Therefore, the microplasma array in helium, extending the plasmas into ambient air, was investigated for material processing. In addition, to further analyze coaxial dielectric barrier discharges, an atmospheric-pressure plasma jet (APPJ) [2.6] was examined. It is similar to the microplasma array in terms of the structure

and allows the plasma to grow abnormally in operation with helium. The APPJ was proposed by Engemann's group, and they found that the plasma jet is not constant in time but rather a "plasma bullet" coming out of the tube at a velocity much higher than the gas velocity [2.6]. K. Kitano *et al.* suggested the "plasma bullet" is a moving ionization front, which is also known to exist in positive streamer corona discharges [2.7, 8]. Furthermore, by laser induced fluorescence (LIF) method, our group verified that the gas temperature in the APPJ is as low as 300 K and that the bullet-like plasma is driven by the ionization wave through the rare gas channel [2.9]. Therefore, in this study, the reactions in the APPJ were presented by optical emission spectroscopy (OES), and the density of $He^*(2^3S_1)$ metastable excited atoms in the APPJ was measured by laser absorption spectroscopy (LAS) [2.5, 10]. Finally, the extending mechanism of the coaxial dielectric barrier discharges were verified by measuring the length of the plasma plume.

2.2 Experimental Procedure

The experimental setup of the microplasma array is schematically shown in Fig. 2.1. Figure 2.1(a) shows a photograph of the microplasma array in helium and mesh electrodes used in this experiment. When helium gas velocity was below 1 m/s, the plasmas did not extend to the outside of the hollows but were generated only in them. Figure 2.1(b) shows a schematic of the front view of the microplasma array. The electrode consists of two metal plates with aligned rectangular hollows, whose size is 0.36×1 mm^2, covered with a dielectric layer of Al_2O_3 at a thickness of 0.3 mm. The overall view of the microplasma array and the cross sectional view are shown in Fig. 2.1(c). A bipolar impulse voltage at a frequency of 5 kHz, was applied through

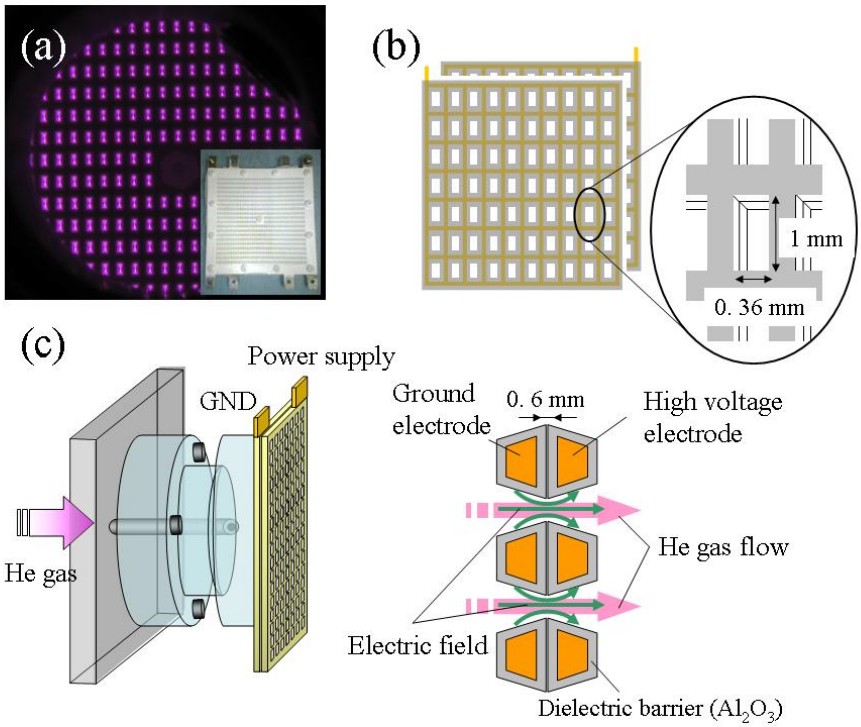

Figure 2.1 Schematics of microplasma array. Photograph of microplasma array in helium and appearance of mesh electrodes (a), illustration of the front view of mesh electrodes (b), and schematics of the overall view of our system and the cross sectional view of microplasma array (c).

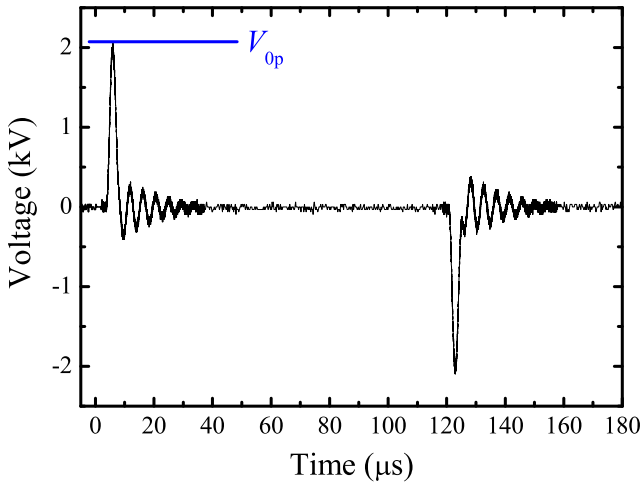

Figure 2.2 Typical waveform of applied voltage.

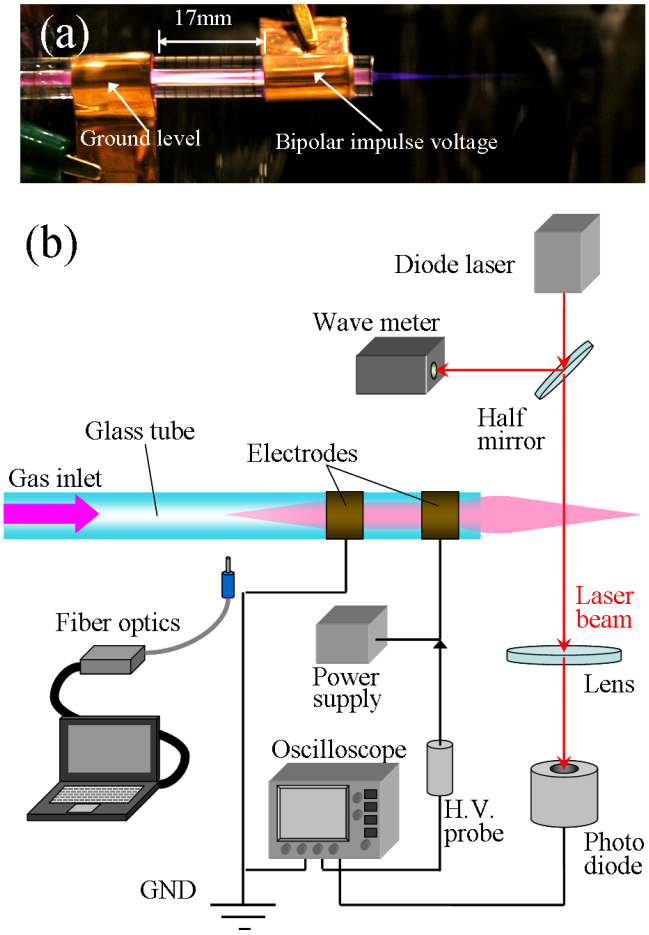

Figure 2.3 Schematics of APPJ: Photograph of APPJ (a) and schematic drawing of experimental setup for OES and LAS measurement of APPJ (b).

the dielectric layers along the gas flow path. The waveform of the applied voltage is shown in Fig. 2.2 [2.11], and the peak value of the applied voltage is designated by V_{0p}.

Figure 2.3 shows schematics of the APPJ used in this study. The appearance of the APPJ is shown in Fig. 2.3(a). The APPJ source, which consists of a glass tube with cylindrical metal electrodes, was driven by a bipolar impulse voltage at a frequency of 5 kHz, and helium gas flowed through the glass tube into ambient air. The APPJ was also operated as a coaxial dielectric barrier discharge in the same way as the microplasma array. For OES measurement of the APPJ, three different regions, where the visible light was emitted, were focused on:

the upstream site of the gas flow (upstream region), the region between electrodes (discharge region), and the downstream site in ambient air (downstream region).

Figure 2.3(b) shows a schematic diagram of OES and LAS measurement. The emission spectra in every region were measured by OES (USB2000, Ocean Optics Inc.) with an optical fiber, which was held normal to the direction of the gas flow as shown in Fig. 2.3(b). OES was conducted to obtain complementary information on the excited species present in the plasma. LAS measurement was used for estimation of the density of $He^*(2^3S_1)$ metastable excited atoms with a laser beam at a wavelength of 1083 nm, which is absorbed in $He^*(2^3S_1)$ metastable excited atoms and excites them to the $2^3P_J^\circ$ ($J = 0, 1, 2$) states[†]. A tunable diode laser (TEC-500, Sacher Lasertechnik) was used for the light source and a photo diode (G8370-03, Hamamatsu Photonics) was used for detection of the light. The laser beam, whose wavelength was monitored by a wavemeter (Wavemate^{TM} Deluxe, COHERENT) and tuned to 1083 nm, was passed through the plasma plume at right angles to the gas flow and received by the photo diode. The detected signals contained the variation in the density of $He^*(2^3S_1)$ metastable excited atoms caused only by excitation and deexcitation of them because the discharge duration was much shorter than the residence time of gas particles. The procedure used in estimating the density of $He^*(2^3S_1)$ metastable excited atoms was similar to that described by K. Tachibana *et al.* [2.5]. The energy levels and transitions of helium and nitrogen are shown in Figs. 2.4 and 2.5, and the significant transitions for this experiment are colored in red in the figures. N_2 2nd positive system bands appear very readily and are of frequent occurrence as an impurity, and N_2^+ 1st negative system occurs readily in the presence of excess helium.

[†]"$\circ$" in the upper right in the total orbital angular momentum quantum number "P" means that the wave function is an odd function with respect to the center of symmetry at the atomic nucleus.

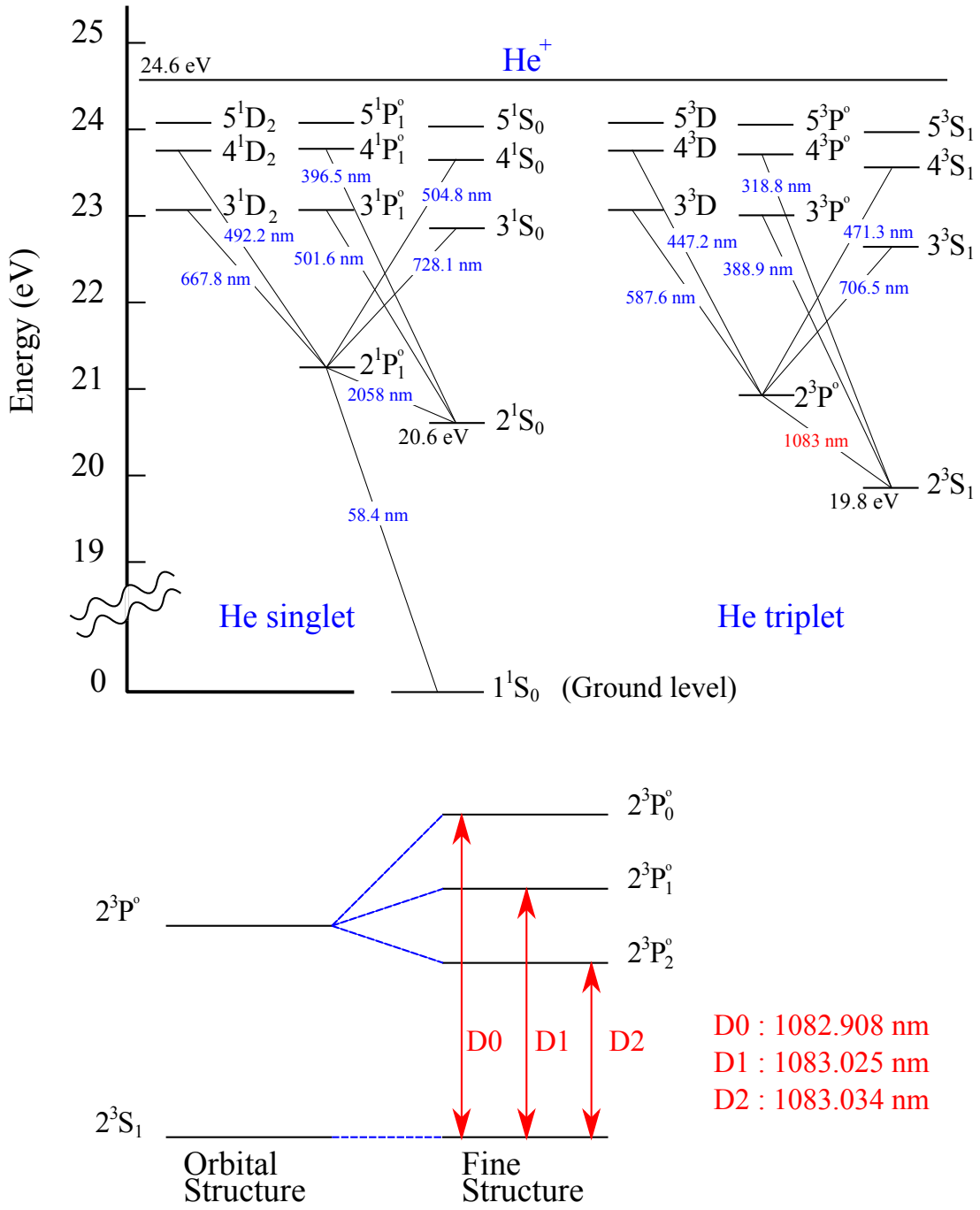

Figure 2.4 Energy level diagram of helium, divided according to the multiplicity 1 or 3 (upper) and energy level splitting of helium atoms (lower). Not drawn in scale. [2.12].

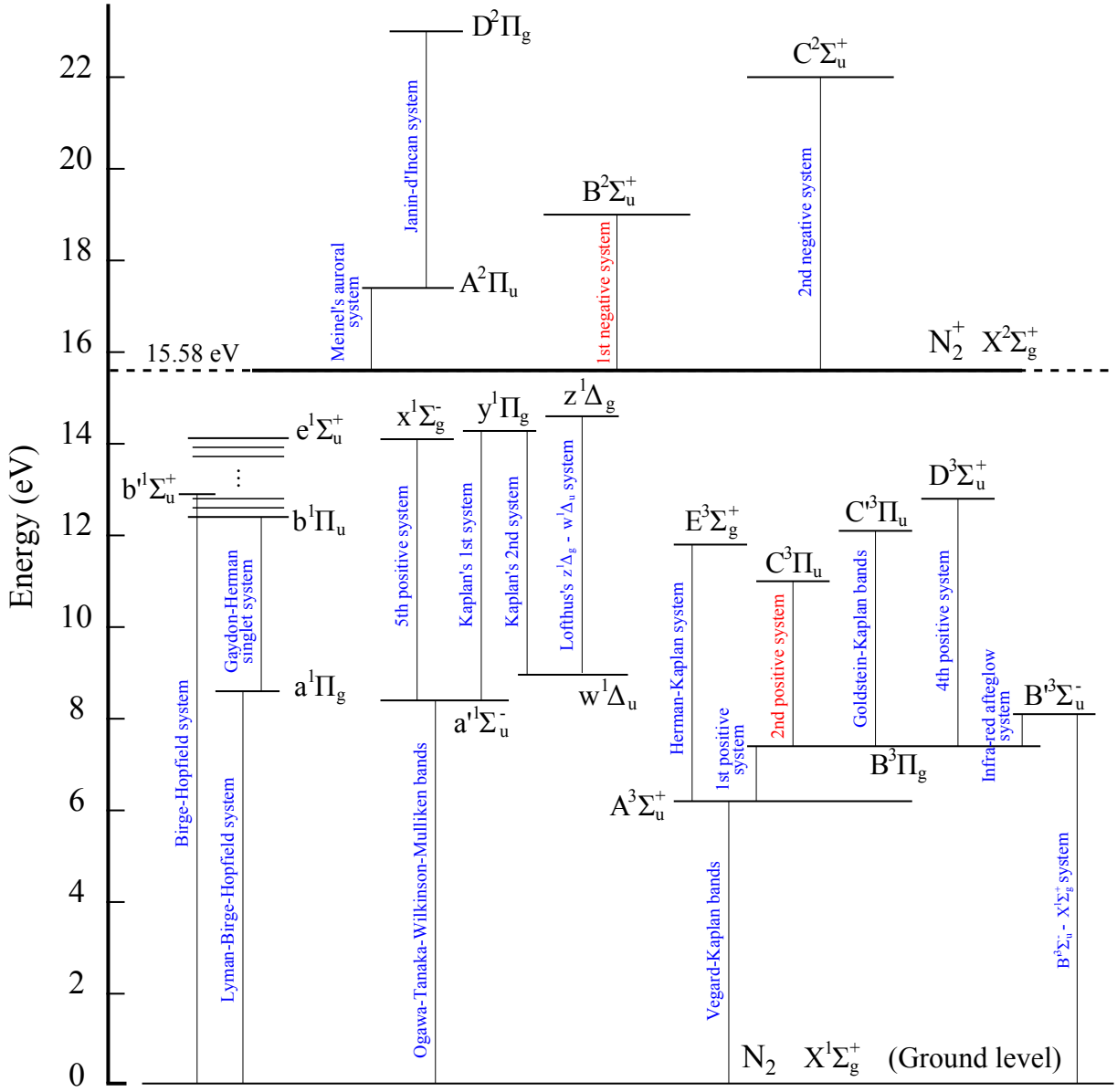

Figure 2.5 Energy level diagram of nitrogen molecule and ion [2.13].

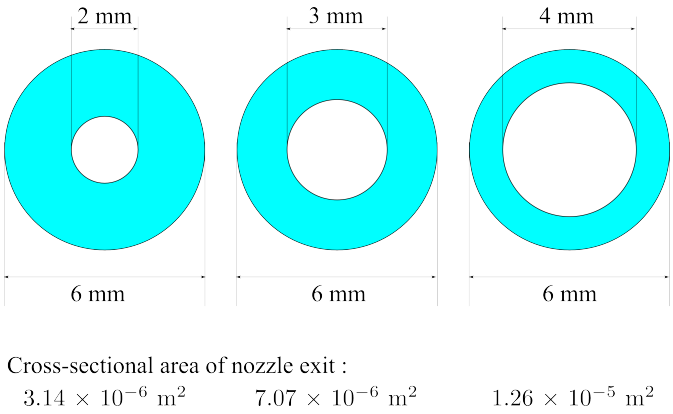

Figure 2.6 Cross sectional view of glass tubes.

Finally, for the measurement of the length of the plasma plume, three kinds of glass tubes, which had different inner diameters of 2, 3, and 4 mm while the outer diameter was constant at 6 mm, as shown in Fig. 2.6, were used. By changing the inner diameter, the flow velocity of helium gas can be changed widely.

2.3 Results and Discussion

2.3.1 Microplasma Array

Figure 2.7 shows photographs and emission intensity maps in a hollow of the microplasma array in helium and nitrogen. In the case of helium, bright spots were observed at the center of the hollow. On the other hand, in the case of nitrogen, emission was observed only from the vicinity of the wall of the hollow. It is thought that the difference in the position of emission between helium and nitrogen is due to the difference in their discharge mechanism. In the case of helium plasma, He_2 and He^*, which have long lifetime, diffuse from the vicinity of the wall to the center of the hollow, and then emission occurs at the center of the hollow. In addition, the

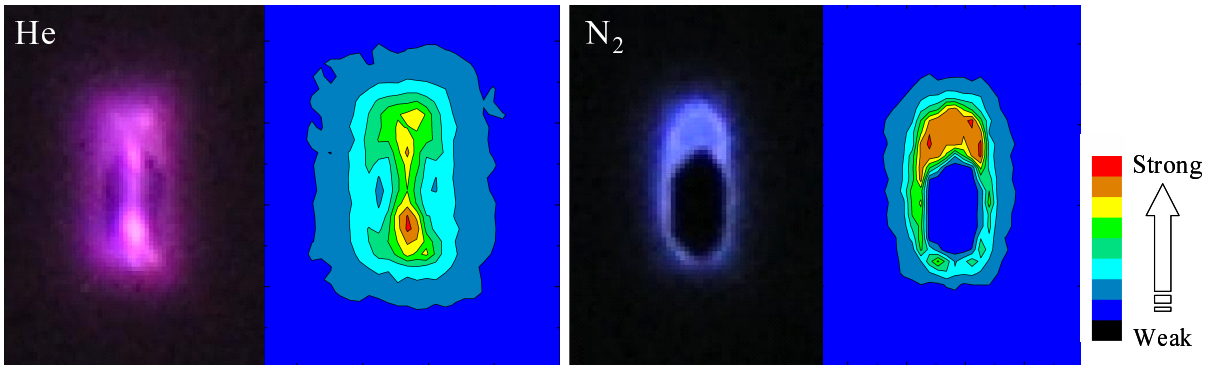

Figure 2.7 Photographs and emission intensity maps in a hollow of microplasma array in helium at V_{0p} = 0.86 kV, at a gas flow rate of 1800 sccm (standard cubic centimeter per minute) (left) and in nitrogen at V_{0p} = 2.38 kV, at a gas flow rate of 1800 sccm (right).

bright spots at the center might be caused also by the hollow cathode effect [2.14]. From this result, it is found that the microplasma array in helium is preferable to draw plasmas out of the hollows.

Figure 2.8(a) shows photographs of the microplasma array in helium effused from the hollows to ambient air. By partially bunging up the hollows of mesh electrodes with a dielectric sheet, high flow velocity of up to 45 m/s was obtained, and the plasmas extended from the hollows to the outside in their length of several mm. The length of the plasma plume effused to ambient air as a function of applied voltage is shown in Fig. 2.8(b) and as a function of helium flow velocity is shown in Fig. 2.8(c). The breakdown voltage was around 0.3 kV, and the length of the plasma plume increased almost linearly with increasing V_{0p} below 2 kV at a constant velocity of helium gas, as shown in Fig. 2.8(b). On the other hand, at the same voltage, the length of the plasma plume increased abruptly up to 10 m/s, above which it increased gradually as shown in Fig. 2.8(c). In this experiment, the Reynolds number was less than 150, so the helium flow was laminar flow in all conditions. That is, it is thought that the electric fields imposed a limitation on the length of the plasma plume. However, since the length of the plasma plume was shorter

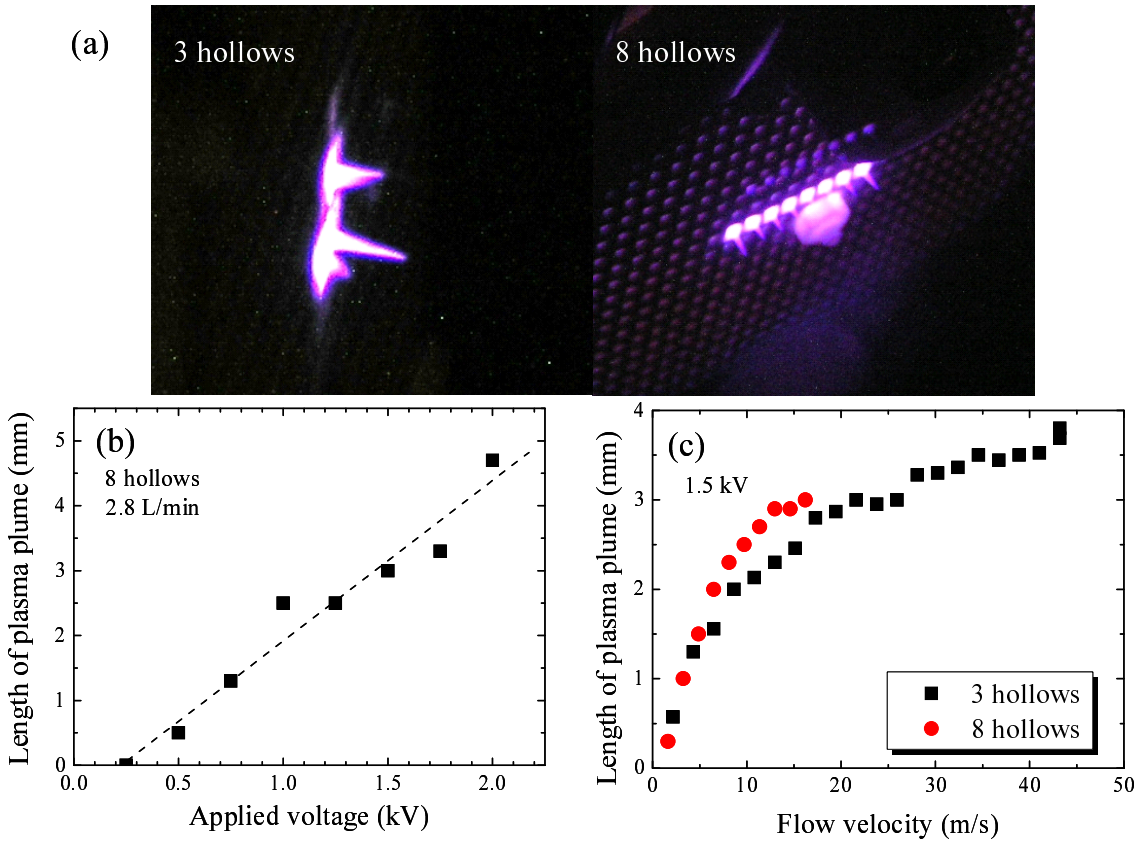

Figure 2.8 Photographs of microplasma array effused from three hollows (left) and eight hollows (right) (a), the length of plasma plume of microplasma array as a function of applied voltage at a flow velocity of 16 m/s (b) and as a function of helium flow velocity at V_{0p} = 1.5 kV (c).

than 5 mm, i.e., it is difficult to observe the plasma plume precisely, the detailed experiment by using the APPJ, which has several-cm length of the plasma plume, was carried out.

2.3.2 Atmospheric Pressure Plasma Jet

Figure 2.9 shows the waveform of applied voltage and high-speed photographs of the APPJ. The dielectric barrier discharge took place between the ring electrodes and the plasma jet was prolonged to the outside of the capillary along the electric field in the helium stream. When the polarity of the applied voltage was positive, the “plasma bullet” was observed, and the

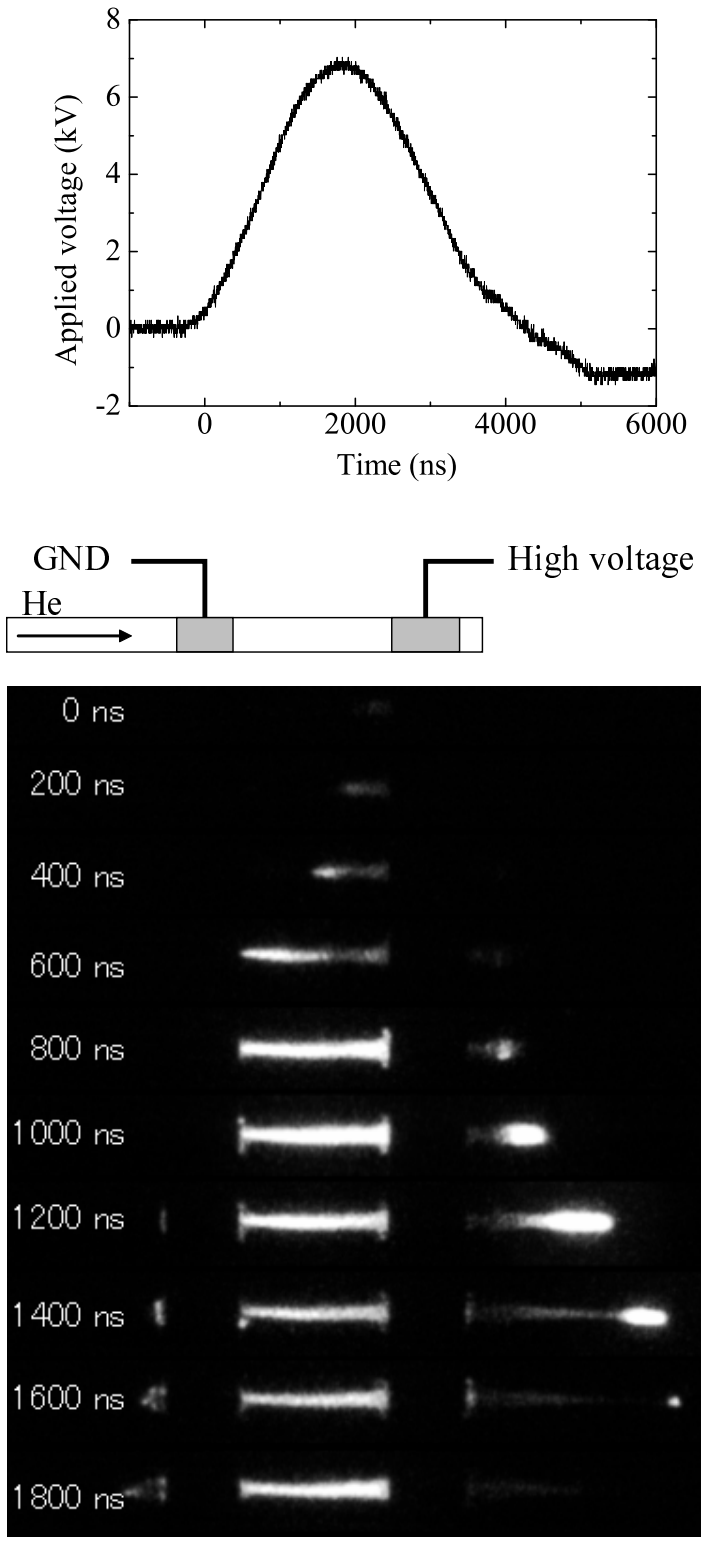

Figure 2.9 High-speed photograghs of the plasma extension into the ambient air (exposure time 100 × 100 ns) at V_{0p} = 7 kV and at 4-mm inner diameter of glass tube when the voltage was in positive phase.

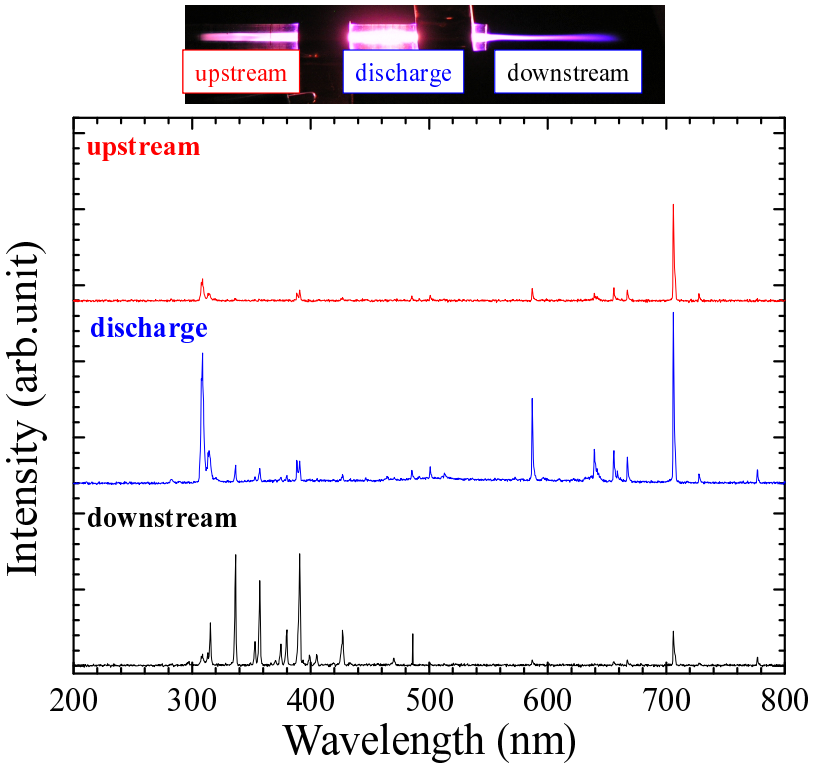

Figure 2.10 OES spectra of APPJ at three different points.

velocity was about 50 km/s. This value is about 10^4 times larger than the helium flow velocity. Furthermore, the “plasma bullet” was not observed when the applied voltage was in negative phase. Therefore, the plasma plume was not transported from the inside of the glass tube and effused to the outside by helium flow.

Figure 2.10 shows the OES spectra of the APPJ at three different points: upstream region, discharge region, and downstream region. In the upstream and the discharge regions, the emission spectra originating from helium (3^3D - 2^3P°: 706.5 nm, 3^3S_1 - 2^3P°: 587.6 nm, and so on) are mainly observed. In contrast, in the downstream region, the peaks originating from nitrogen, shown in Table 2.1, are observed, and these nitrogen molecules and ions are originated from ambient air. In particular, the peaks originated from N_2^+ 1st negative system bands ($B^2\Sigma_u^+$ - $X^2\Sigma_g^+$) indicate that the Penning ionization ($He^*(2^3S_1) + N_2 \rightarrow He + N_2^+(B^2\Sigma_u^+) + e$) occurs in

Table 2.1 Typical transition systems of nitrogen molecular and ion [2.13].

Wavelength (nm)	Transition system	v'	v''
313.60	N_2 (2nd Positive system)	2	1
315.93	N_2 (2nd Positive system)	1	0
337.13	N_2 (2nd Positive system)	0	0
353.67	N_2 (2nd Positive system)	1	2
356.39	N_2^+ (1st Negative system)	2	1
357.69	N_2 (2nd Positive system)	0	1
358.21	N_2^+ (1st Negative system)	1	0
371.05	N_2 (2nd Positive system)	2	4
375.54	N_2 (2nd Positive system)	1	3
380.49	N_2 (2nd Positive system)	0	2
389.46	N_2 (2nd Positive system)	3	6
391.44	N_2^+ (1st Negative system)	0	0
394.30	N_2 (2nd Positive system)	2	5
399.84	N_2 (2nd Positive system)	1	4
405.94	N_2 (2nd Positive system)	0	3
423.65	N_2^+ (1st Negative system)	1	2
427.81	N_2^+ (1st Negative system)	0	1
470.92	N_2^+ (1st Negative system)	0	2

the downstream region. Therefore, the discharge mechanism in the downstream region appears to be different from that in the glass tube.

In addition, the OES spectra at the downstream region of the APPJ with an auxiliary ground electrode placed at a distance of 2 cm from the nozzle exit of the jet are shown in Fig. 2.11. With the auxiliary ground electrode, the emission intensity from the plasma at the downstream region became stronger. However, the spectra were similar to those without the auxiliary ground electrode, i.e., there were some peaks originated from nitrogen molecules and nitrogen ions as shown in Fig. 2.11(a). Here, the gas temperature T_g was assumed to be in equilibrium with the rotational temperature T_{rot} of molecular nitrogen, and the value was estimated from the unresolved rotational structure in the 2nd positive system ($C^3\Pi_u$ - $B^3\Pi_g$) of the emission spectra [2.15, 16]. Actually, T_g easily reaches the same value of T_{rot} at atmospheric pressure.

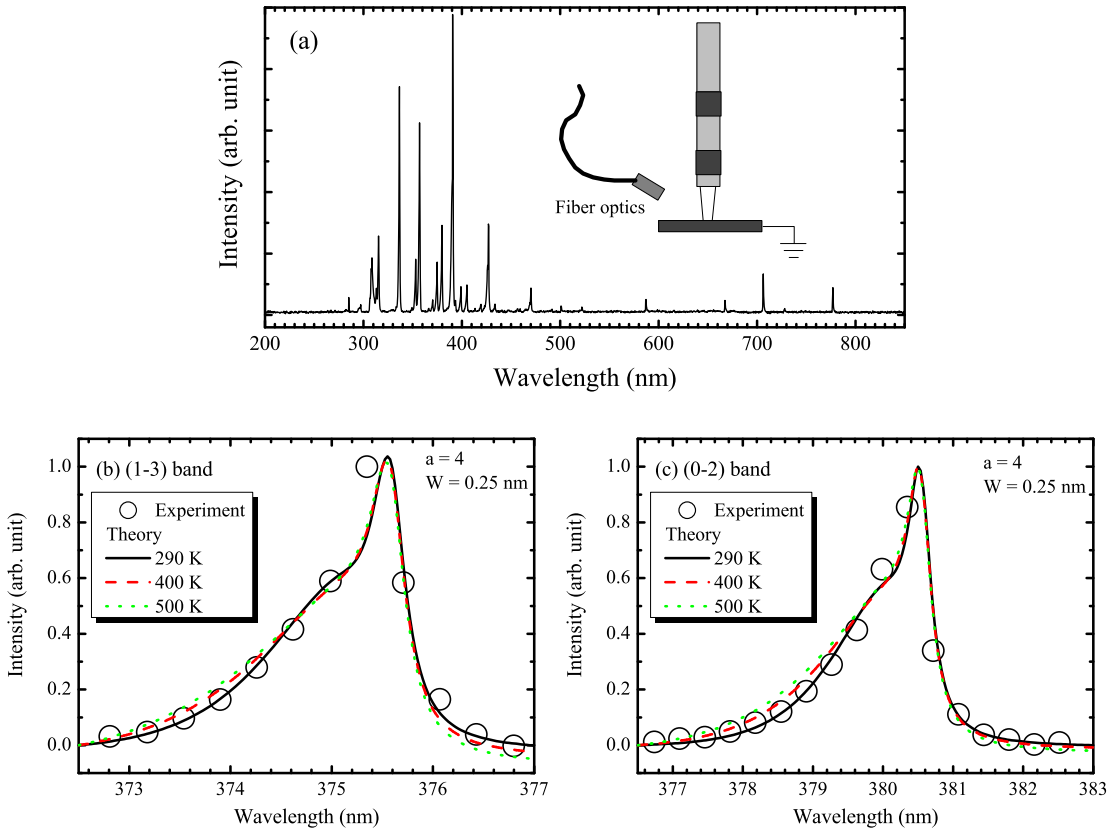

Figure 2.11 OES spectra at downstream of APPJ with an auxiliary ground electrode placed at a distance of 1.5 cm from the nozzle exit in the 200 nm to 850 nm range (a). Observed and simulated emission spectra of the 1' - 3" transition (b) and the 0' - 2" transition (c) in the 2nd positive N_2 system ($C^3\Pi_u$ - $B^3\Pi_g$).

The wavelength of the rovibronic transition C$v'J'$ - B$v''J''$ is derived from

$$\lambda^{\mathrm{C}v'J'}_{\mathrm{B}v''J''} = \left\{ N_{\mathrm{a}} \sum_{p=0}^{5} \sum_{q=0}^{2} Y^{\mathrm{C}}_{pq} \left(v' + \frac{1}{2} \right)^p \left[J' \left(J' + 1 \right) \right]^q - Y^{\mathrm{B}}_{pq} \left(v'' + \frac{1}{2} \right)^p \left[J'' \left(J'' + 1 \right) \right]^q \right\}^{-1}, \quad (2.1)$$

where N_{a} is the refractive index of air and Y_{pq} is the expansion coefficient in the Dunham series.

The radiant flux $F^{\mathrm{C}v'J'}_{\mathrm{B}v''J''}$ of the rotational transition is represented by

$$F^{\mathrm{C}v'J'}_{\mathrm{B}v''J''} = D \frac{S_J}{T_{\mathrm{rot}}} \exp \left[-hc\mathrm{B}_v J' \left(J' + 1 \right) / kT_{\mathrm{rot}} \right], \quad (2.2)$$

where D is a constant, S_J is the line intensity in the Hund's case (a) given by Budó [2.17]. In general, the slit width of the monochromator governs the width of a rotational line. Therefore, the finite line shape:

$$g(\Delta\lambda) = \frac{a - (2\Delta\lambda/W)^2}{a + (a-2)(2\Delta\lambda/W)^2} \tag{2.3}$$

was assumed for computational simplicity. Here, a is a constant and W is obtained as the resolution of the monochromator. From these expressions, T_{rot}, i.e., T_{g} can be estimated. Figures 2.11(b) and (c) provide the simulated emission spectra against several values of T_{rot} focused on the 1' - 3" transition and the 0' - 2" transition in the 2nd positive N_2 system, respectively. The constants for the calculation:

$$Y^{\mathrm{C}}_{pq} = \begin{pmatrix} 89136.88 & 2047.178 & -28.445 & 2.08833 & -0.5.35 & 0 \\ 1.82473 & -1.8683\times10^{-2} & -2.275\times10^{-3} & 7.33\times10^{-4} & -1.5\times10^{-4} & 0 \\ 0 & 0 & 0 & 0 & 0 & 0 \end{pmatrix},$$

$$Y^{\mathrm{B}}_{pq} = \begin{pmatrix} 59619.2 & 1733.391 & -14.1221 & -5.688\times10^{-2} & 3.612\times10^{-3} & -1.109\times10^{-4} \\ 1.6374 & -1.791\times10^{-2} & -7.647\times10^{-5} & 0 & 0 & 0 \\ 0 & 0 & 0 & 0 & 0 & 0 \end{pmatrix} \tag{2.4}$$

were taken from Ref. 2.18. The best-fit parameters were found to be W = 0.25 nm, a = 4, and T_{rot} = 290 K. The simulated spectra agree well with those observed in the experiment. Therefore, T_{g} was around 290 K, and this value is similar to that without the auxiliary ground electrode. This means that the gas flow effectively decreases the gas temperature even if the auxiliary ground electrode, e.g., a processing object, is installed.

Since the spectra of N_2^+ 1st negative system indicate the existence of $He^*(2^3S_1)$ metastable excited atoms, LAS measurement was performed to estimate the density of $He^*(2^3S_1)$ atoms. The absolute density of $He^*(2^3S_1)$ atoms n_{m} is given by integrating the absorption coefficient $k_{12}(\nu)$ of one component, e.g., D2 transition ($2^3S_1 \rightarrow 2^3P_2^\circ$) with the largest absorption, over the

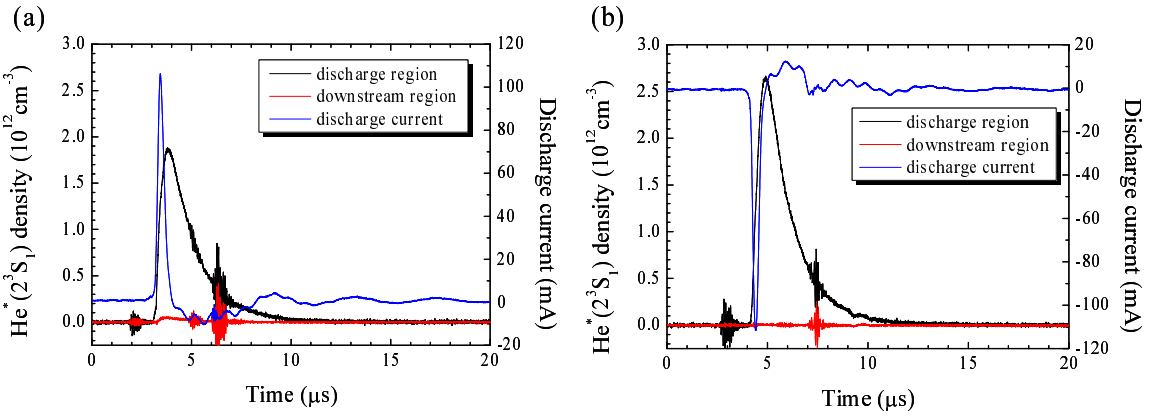

Figure 2.12 Time evolution of $He^*(2^3S_1)$ density in discharge region, that in downstream region, and discharge current with (a) positive and (b) negative impulse voltage applied.

frequency ν as follows [2.5]:

$$n_{\mathrm{m}} = \frac{8\pi g_1}{\lambda_0^2 g_2 A_{21}} \int k_{12}(\nu) d\nu, \qquad k_{12}(\nu) = -\frac{1}{l} \ln \frac{I}{I_0}, \tag{2.5}$$

where I_0 and I are the incident and transmitted laser intensities, l is the diameter of the plasma, λ_0 is the wavelength (= 1083 nm), $g_i = 2J_i + 1$ is the statistical weight of the lower ($i = 1$) and upper ($i = 2$) states, and A_{21} is the transition probability (= 1.022×10^7 s^{-1}). Figure 2.12 provides the $He^*(2^3S_1)$ densities in the discharge and downstream regions, depending on the polarity of the applied voltage. In the downstream region, the laser beam passed through a point 1 cm away from the nozzle exit of the jet. When the polarity of the applied voltage was positive, the measured density of $He^*(2^3S_1)$ atoms in the discharge region was on the order of 10^{12} cm^{-3}, whereas the density in the downstream region was around 10^{10} cm^{-3}, as shown in Fig. 2.12(a). Additionally, in the downstream region, the $He^*(2^3S_1)$ atoms were observed only when positive voltage was applied. Therefore, the majority of $He^*(2^3S_1)$ atoms in the downstream region were not transported from the discharge region by the gas flow but produced in the downstream

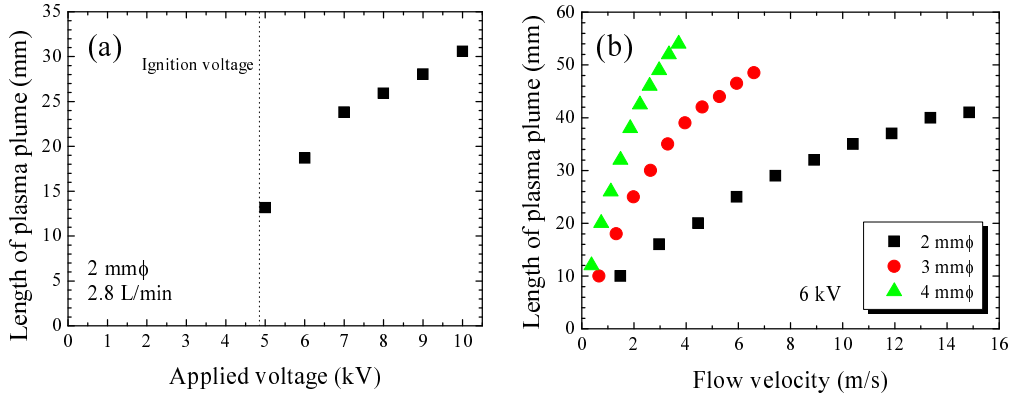

Figure 2.13 Length of plasma plume of APPJ as a function of applied voltage at a flow velocity of 15 m/s (a) and helium flow velocity at V_{0p} = 6 kV (b).

region, only when the voltage was positive. This indicates that active species such as $He^*(2^3S_1)$ and N_2^+ are generated in the downstream region and the plasma in the downstream region is maintained through the Penning ionization of N_2 via $He^*(2^3S_1)$ atoms.

Figure 2.13 shows the length of the plasma plume effused into ambient air as a function of the applied voltage, shown in Fig. 2.13(a), and as a function of helium flow velocity with various inner diameters of the glass tube, shown in Fig. 2.13(b). The ignition voltage was 4.8 kV at a flow velocity of 15 m/s. At a constant flow velocity, the length of the plasma plume was increased as the applied voltage was increased up to V_{0p} = 10 kV as shown in Fig. 2.13(a). At the same voltage, the length of the plasma plume was increased with increasing flow velocity at every inner diameter of the glass tube, and a larger inner diameter of the glass tube led to a longer plasma plume.

Figure 2.14(a) shows photographs of the APPJ with three different inner diameters of the glass tube, i.e., 2, 3 and 4 mm. V_{0p} was 6 kV and the helium flow rate was 2.8 L/min. In the case of 2 mm, the plasma plume stretched straight ahead, but in the case of 4 mm, the plasma

plume turned up slightly. Figure 2.14(b) shows the calculated profiles of helium concentration in a nitrogen atmosphere. The numerical analysis of helium gas flow distribution was performed by a solver for computational fluid dynamics (PHOENICS version 3.5.1, Concentration Heat & Momentum Limited) [2.19]. The helium flow rate was 2.8 L/min. From this calculation, the helium flow channel went up in the case of 4-mm inner diameter, and the plasma plume extended along the helium flow. In the downstream region, the Penning reaction is the main process of ionization, and thus the concentration of nitrogen in helium affected the discharge mechanism.

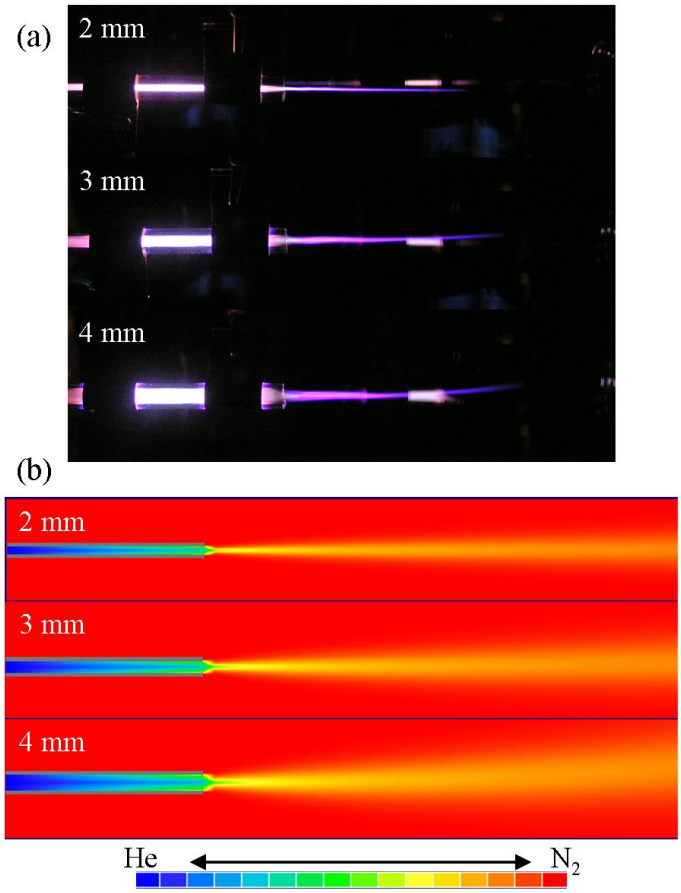

Figure 2.14 (a) Photographs of APPJ using three different glass tubes with inner diameters of 2, 3 and 4 mm. V_{0p} is 6 kV and the helium flow rate is 2.8 L/min. (b) Calculated profiles of helium concentration in nitrogen; helium flow rate is 2.8 L/min.

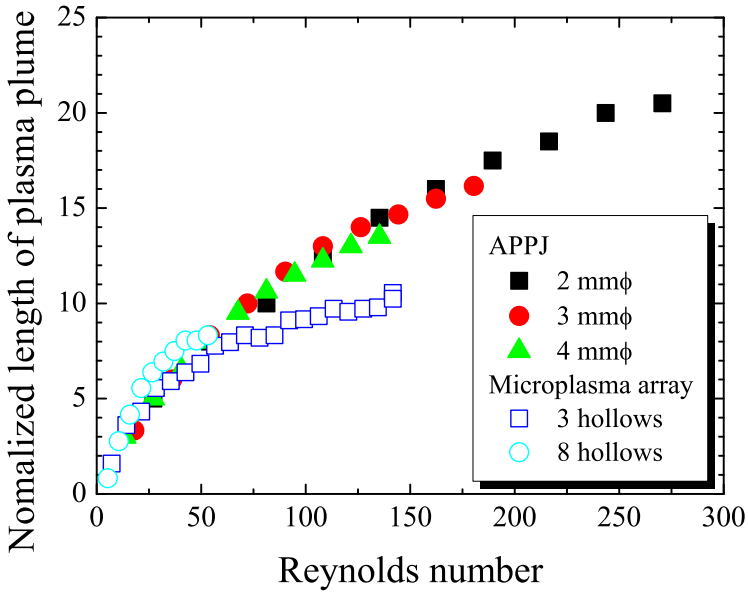

Figure 2.15 Normalized length of plasma plume of microplasma array and APPJ as a function of Reynolds number. Normalized length is the length of the plasma plume divided by the inner diameter (0.36 mm in the case of microplasma array).

Figure 2.15 shows the normalized length of plasma plume as a function of the Reynolds number of coaxial dielectric barrier discharges. The normalized length is the length of the plasma plume divided by the inner diameter of the nozzle exit. In the case of the microplasma array, the inner diameter was regarded as 0.36 mm. Reynolds number *Re* is expressed by the equation:

$$Re = \frac{\rho U d}{\mu}, \tag{2.6}$$

where U is the mean fluid velocity, d is a characteristic length, ρ is the density of the fluid, and μ is the dynamic viscosity of the fluid. The Reynolds number determines whether the fluid is laminar or turbulent. In every case, the Reynolds number was less than 300, showing that the helium flow was laminar. The Reynolds number also represents the length of the helium

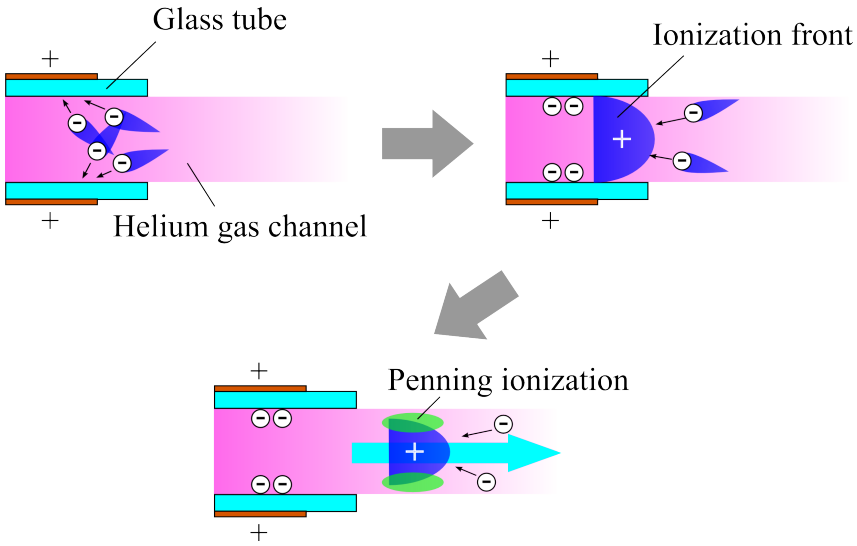

Figure 2.16 Extending mechanism of plasma plume in ambient air.

channel, i.e., larger Reynolds number means that the distance of the helium channel is longer. At a small Reynolds number, the normalized length of the plasma plume overlapped with each other in all cases. At a high Reynolds number, the normalized length overlapped with each other in the same applied voltage cases. That is, it is thought that the electric field determined the maximum length of the plasma plume. From this result, the normalized length of the plasma jet was determined by the Reynolds number and the applied voltage:

$$\frac{L}{d} \propto f(E) \times g(Re), \tag{2.7}$$

where d is inner diameter of the nozzle exit, L is the length of the plasma plume, and E is the electric field. Therefore, the plasma plume is propagated by the electric field along the helium channel, where the plasma can be glow-like, as shown in Fig. 2.16. The avalanches of electrons produce the ionization front containing helium ions and active species like $He^*(2^3S_1)$ in the vicinity of the electrode. Then, another avalanches of electrons occurs in front of the ionization

front, and it moves forward along the helium gas channel. Finally, $He^*(2^3S_1)$ atoms produced in the plasma cause the Penning ionization with nitrogen molecules, and the plasma becomes glow-like.

2.4 Summary

OES spectra and LAS signals from the APPJ were measured, and it was found that the discharge mechanism of the APPJ was different between its parts: inside and outside of the glass tube. OES and LAS reveal that the direct and stepwise ionization reactions affect the generation of plasmas in the discharge region, but the $He^*(2^3S_1)$ atoms play an important role in producing plasmas by the Penning ionization with nitrogen in the downstream region. The density of $He^*(2^3S_1)$ atoms in the discharge region was on the order of 10^{12} cm^{-3} and that in the downstream region was 10^{10} cm^{-3}. By measuring the length of the plasma plume, it was found that the plasma at the downstream region is propagated by the electric field along the helium flow and that the Reynolds number is one of the significant factors determining the extension of the plasma plume.

References

[2.1] S. Kanazawa, M. Kogoma, T. Moriwaki and S. Okazaki: J. Phys. D: Appl. Phys. **21**, 838 (1988).

[2.2] S. Okazaki, M. Kogoma, M. Uehara and Y. Kimura: J. Phys. D: Appl. Phys. **26**, 889 (1993).

[2.3] K. H. Schoenbach, M. Moselhy, W. Shi and R. Bentley: J. Vac. Sci. Technol. A **21**, 1260 (2003).

[2.4] O. Sakai, Y. Kishimoto and K. Tachibana: J. Phys. D: Appl. Phys. **38**, 431 (2005).

[2.5] K. Tachibana, Y. Kishimoto and O. Sakai: J. Appl. Phys. **97**, 123301 (2005).

[2.6] M. Teschke, J. Kedzierski, E. G. Finantu-Dinu, D. Korzec and J. Engemann: IEEE Trans. Plasma Sci. **33**, 310 (2005).

[2.7] G. V. Naidis: J. Phys. D: Appl. Phys. **29**, 779 (1996).

[2.8] K. Kitano and S. Hamaguchi: *Proc. 18th Int. Symp. Plasma Chem.* 27A-a5 (Kyoto, 2007).

[2.9] K. Urabe, Y. Ito, K. Tachibana and B. N. Ganguly: Appl. Phys. Express **1**, 066004 (2008).

[2.10] M. W. Millard, P. P. Yaney, B. N. Ganguly and C. A. D. Jr: Plasma Sources Sci. Technol. **7**, 389 (1998).

[2.11] T. Somekawa, T. Shirafuji, O. Sakai, K. Tachibana and K. Matsunaga: J. Phys. D: Appl. Phys. **38**, 1910 (2005).

[2.12] *NIST Atomic Spectra Database*, http://physics.nist.gov/PhysRefData/ASD/.

[2.13] R. E. B. Pearse and A. G. Gaydon: *The Identification of Molecular Spectra 4th edition* (Chapman and Hall, London, 1976).

[2.14] C. C. V. Voorhis and A. G. Shenstone: Rev. Sci. Instrum. **12**, 257 (1941).

[2.15] D. M. Phillips: J. Phys. D: Appl. Phys. **9**, 507 (1976).

[2.16] S. Momose, T. Nakamura and K. Tachibana: Jpn. J. Appl. Phys. **39**, 555 (2000).

[2.17] A. Budó: Z. Physik **105**, 579 (1937).

[2.18] K. P. Huber and G. Herzberg: *Molecular Spectra and Molecular Structure IV. Constants of Diatomic Molecules* (Van Nostrand Reinhold Company, New York, 1979).

[2.19] S. Patankar and D. Spalding: Int. J. Heat Mass Transfer **15**, 1787 (1972).

Chapter 3

Measurement of Electron Density in Microplasma Array[†]

3.1 Introduction

Atmospheric pressure glow-like discharges (APGDs) have attracted considerable interest in recent years for their potential applications in material processes such as surface modification [3.1, 2], dry etching [3.3, 4], and thin-film deposition [3.5, 6], because APGDs can be generated without vacuum systems and can lead to low-cost fabrications. Various schemes, such as diffusive glow discharges with forced gas flow [3.7], short pulsed discharges [3.8], and dielectric barrier discharges (DBDs) [3.9], have been investigated for the generation of APGDs since the discharges at atmospheric-pressure tend to shift to arc discharges. These methods suppress energy transfer from electrons into heavy particles, which are neutral particles and ions, in order to prevent APGDs from changing into arc discharges or filamentary discharges. As a result, plasmas can maintain their thermal non-equilibrium state. However, it is still difficult to keep the atmospheric pressure discharge uniform over a large area due to its complicated internal and external energy and particle transport processes. For instance, in many cases APGDs are prone to converge into many filaments or form self-organized structures [3.10, 11].

[†]This Chapter, in slightly altered form, is published in: Y. Ito, O. Sakai and K. Tachibana, "Measurement of electron density in a microdischarge-integrated device operated in nitrogen at atmospheric pressure using a millimetre-wave transmission method", Plasma Sources Science and Technology **19**, 025006 (2010).

Here, a change in thinking gives us the technology of microplasmas to get high electron density in a small region [3.12, 13]. When we diagnose microplasmas, it is difficult to use a Langmuir probe in order to measure the electron density because of their smallness. For measurement of the plasma parameters, such as electron density and electron temperature, of microplasmas, laser-aided and electromagnetic-wave-aided diagnostics can be useful methods [3.14–16].

On the other hand, our group have produced a large-area device using a two-dimensional array of small coaxial dielectric barrier discharges, called “microplasma array”. It can generate a pseudo-uniform atmospheric-pressure plasma in various gases, and each component can have higher plasma density than in typical APGDs [3.12, 17]. The microplasma array is formed by stacking two insulated metal meshes with vertically aligned hollows. Their characteristics in pure helium and helium admixed with a small amount of nitrogen have been analyzed so far and the electron density on the order of 10^{12} cm^{-3} was measured successfully [3.18–20]. In addition, plasma photonic crystals with this integrated structure have been developed for the control of electromagnetic waves [3.20, 21], and also the deposition of SiO_2 thin films has been carried out using the microplasma array with tetraethoxysilane as a source material [3.22]. To improve these applications, the electron density in the microplasma array in various gases should be measured. In particular, it is more practical to use it in atmospheric nitrogen or air in many industrial and biomedical applications. Aiming at these purposes, in this chapter, the performance of the microplasma array in nitrogen without and with a small amount of water and oxygen admixtures are investigated. The characteristic feature of each microplasma was observed by an intensified charge-coupled device (ICCD) camera and the electron density in the microplasma array was measured by a millimeter-wave transmission method, which had

been developed in our group's previous experiments [3.18–20].

In Section 3.2, the theoretical background of the millimeter-wave transmission method is briefly reviewed, and the experimental setup is described. The experimental results are addressed in Section 3.3. In Section 3.4, the results of the diagnostics are discussed in comparison with the theoretical predictions. Section 3.5 summarizes this chapter.

3.2 Experimental Procedure

3.2.1 Millimeter-Wave Transmission Method

The electron plasma frequency ω_{pe} determines the response of the plasma to an external electric field of a wave at angular frequency ω. That is, as mentioned in Chapter 1, if $\omega \gg \omega_{pe}$, the electromagnetic wave can propagate through the plasma. On the other hand, if $\omega \ll \omega_{pe}$, the electromagnetic wave cannot go through and is reflected by the plasma. Those effects take place in collision-less plasmas which have unlimited length. In the cases of collisional plasmas which have finite length, the wave is not reflected perfectly; its phase changes due to the real part of the refractive index of the plasma, and its amplitude attenuates through the plasma via electron elastic collisions. Microwave interferometry measurement is well known as a method which can measure electron density n_e in plasmas by detecting the phase shift [3.23, 24]. A wave whose frequency is close to ω_{pe} is strongly affected by the plasmas in amplitude. Therefore we have used millimeter waves as an extended method of microwave interferometry to the microplasma array, which is of the order of hundreds of μm in size and have $\omega_{pe}/2\pi$ slightly below the millimeter waves. In fact, the electron density also affects the phase shift of the waves, although wave attenuation itself is a good monitor of the electron density.

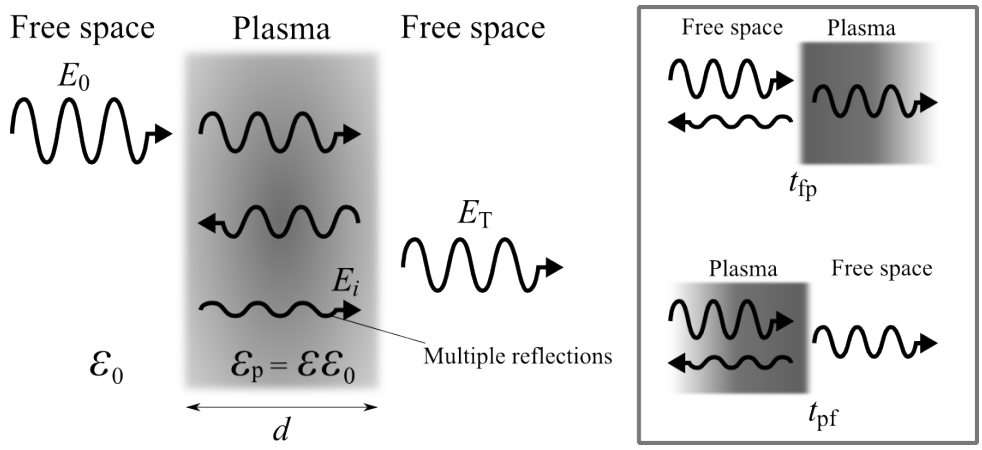

Figure 3.1 Schematic draw of transimssion of electromagnetic wave in plasma.

Bachynski *et al.* have derived a set of equations for transmission of electromagnetic waves in finite plasmas [3.25]. Let us consider a planar wave incident perpendicular to the surface of the slab plasma, as shown in Fig. 3.1. From Maxwell's equations, we obtain

$$\nabla^2 \boldsymbol{E} - \frac{1}{\varepsilon_0}\nabla q - \mu_0 \frac{\partial \boldsymbol{i}}{\partial t} = \frac{1}{c^2}\frac{\partial^2 \boldsymbol{E}}{\partial t^2}, \tag{3.1}$$

where $\boldsymbol{E}$ is an alternating electric field. ε_0, μ_0 and c are the permittivity, the magnetic permeability, and the velocity of light in vacuum, q is charge density and $\boldsymbol{i}$ is current density. $\boldsymbol{E}$ is expressed in terms of time and space:

$$\boldsymbol{E} = E_0 \exp\left[j\left(\omega t - \boldsymbol{k}\cdot\boldsymbol{r}\right)\right], \tag{3.2}$$

where j is the imaginary unit, $\boldsymbol{k}$ and $\boldsymbol{r}$ are a wave number vector and a position vector of the wave. Since the plasmas we consider now are weakly ionized plasmas, we can approximate $q \cong 0$ and $\boldsymbol{i} \cong 0$. Neglecting the contribution of ions to current and assuming purely elastic

collisions, $\partial \boldsymbol{i}/\partial t$ is expressed by

$$\frac{\partial \boldsymbol{i}}{\partial t} = \frac{n_e e^2}{m_e} \frac{j\omega \boldsymbol{E}}{\nu_m + j\omega} = j\omega\sigma \boldsymbol{E}. \tag{3.3}$$

Here e and m_e are the elementary charge and the electron mass. And ν_m and σ are the elastic collision frequency and the complex electric conductivity in the plasma. By applying these approximations and the law of conservation of charge, we get the following equation:

$$\nabla^2 \boldsymbol{E} - j\omega\mu_0\sigma \boldsymbol{E} = \frac{1}{c^2} \frac{\partial^2 \boldsymbol{E}}{\partial t^2}. \tag{3.4}$$

Assuming that the electromagnetic wave propagates in the x direction and the electric field oscillates in the y direction, that is $E_y = E_0 \exp[j(\omega t - kx)]$, equation (3.4) can be solved for the wave number k:

$$k^2 = \frac{\omega^2}{c^2} \left\{ 1 - \frac{\omega_{pe}^2}{\omega^2} \left[\frac{1 + j(\nu_m/\omega)}{1 + (\nu_m/\omega)^2} \right] \right\}. \tag{3.5}$$

By assuming the relative magnetic permeability in the plasma is 1, we also obtain the complex permittivity in plasma ε:

$$\varepsilon = 1 - \frac{\omega_{pe}^2}{\omega^2} \left[\frac{1 + j(\nu_m/\omega)}{1 + (\nu_m/\omega)^2} \right]. \tag{3.6}$$

Figure 3.2 shows the theoretical plots of ε in collisional and collision-less plasmas. The real part of the complex permittivity ε_r is less than 1, and it decreases and becomes negative when ω is sufficiently smaller than ω_{pe}. In this region, the plasma can be dealt with like bulk metal. Whereas, the imaginary part of that ε_i is consistently 0 in the case of collision-less plasmas, and

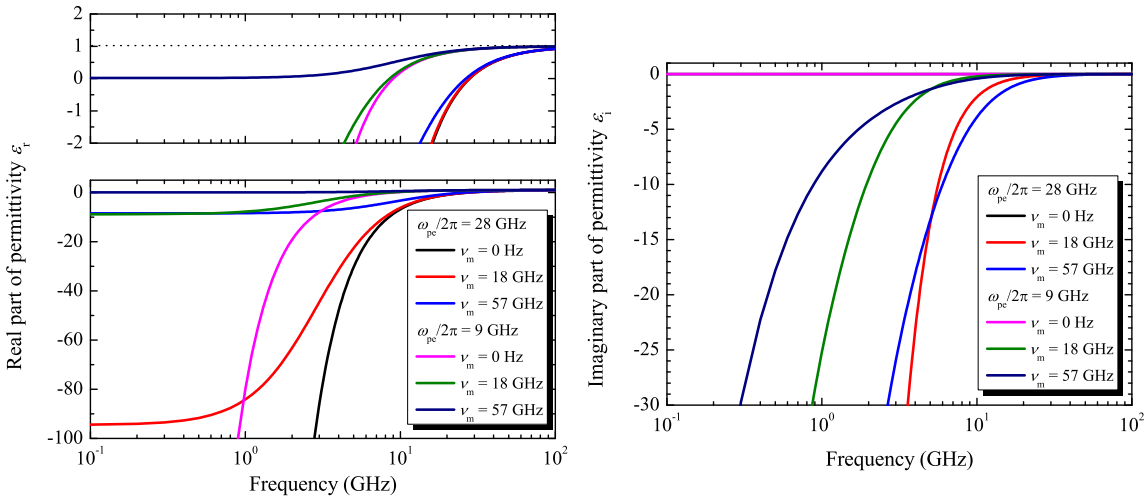

Figure 3.2 Theoretical plots of real and imaginary parts of permittivity in plasma ε as a function of $\omega/2\pi$. When the electron density n_e is 10^{13} and 10^{12} cm^{-3}, the electron plasma frequency ω_{pe} is 28 and 9 GHz, respectively. And when the electron temperature T_e is 1.0 and 10.0 eV in nitrogen plasma at a pressure of 101 kPa and at a temperature of 300 K, the elastic collision frequency ν_m is 18 and 57 GHz, respectively.

it is negative in collisional plasmas at $\omega < \omega_{pe}$.

Besides the transmission coefficient from free space to the plasma t_{fp}, the one from the plasma to free space t_{pf} and the reflectivity coefficient for the boundary with free space in plasma r_{pf} are described as

$$t_{fp} = \frac{2}{1+N_p}, \quad t_{pf} = \frac{2N_p}{N_p+1}, \quad r_{pf} = \frac{N_p-1}{N_p+1}. \tag{3.7}$$

Here, N_p (= $\sqrt{\varepsilon}$) is the complex refractive index in the plasma.

Considering multiple reflections at the boundary with free space in plasma, whose length is d, the electric field of the wave transmitted after $i-1$ reflections in the plasma is obtained as

$$E_i = t_{fp}t_{pf}E_0 \exp(-jkd)\left[r_{pf}\exp(-jkd)\right]^{2(i-1)}. \tag{3.8}$$

Hence total transmission wave amplitude is written as

$$E_{\mathrm{T}} = \sum_{i=1}^{\infty} E_i = \frac{t_{\mathrm{fp}} t_{\mathrm{pf}} E_0 \exp(-jkd)}{1 - {r_{\mathrm{pf}}}^2 \exp(-j \cdot 2kd)}. \tag{3.9}$$

From these equations, we obtain the following equations:

$$\frac{E_{\mathrm{T}}}{E_0} = \{\cosh[(\alpha + j\beta)d] + (Z_{\mathrm{r}} - jZ_{\mathrm{i}}) \sinh[(\alpha + j\beta)d]\}^{-1}, \tag{3.10}$$

$$Z_{\mathrm{r}} = \frac{1}{2}\frac{\beta}{k_0}\frac{|\varepsilon| + 1}{|\varepsilon|}, \quad Z_{\mathrm{i}} = \frac{1}{2}\frac{\alpha}{k_0}\frac{|\varepsilon| - 1}{|\varepsilon|}.$$

Here, k_0 is the wave number in the free space, and α and β are the attenuation coefficient and the phase coefficient of the wave in the plasma, respectively. Therefore, the wave number in the plasma is expressed as $k = \beta - j\alpha$.

In this experiment, the transmitted signals are detected as electrical power. That is, the transmittance T is written as

$$T = \left|\frac{E_{\mathrm{T}}}{E_0}\right|^2 = \left|\cosh[(\alpha + j\beta)d] + (Z_{\mathrm{r}} - jZ_{\mathrm{i}}) \sinh[(\alpha + j\beta)d]\right|^{-2}. \tag{3.11}$$

Since ν_{m} is a function of the electron temperature T_{e}, by assuming the electron temperature T_{e} and the dimension of the plasma d, we can obtain ω_{pe} which is defined generally by

$$\omega_{\mathrm{pe}} \equiv \sqrt{\frac{n_{\mathrm{e}} e^2}{\varepsilon_0 m_{\mathrm{e}}}}. \tag{3.12}$$

From this equation, n_{e} is derived and is in proportion to the square of ω_{pe}.

This method allows us to get the spatially averaged density of electrons. At high pressure,

the sheath is very thin, and since the electron density in this experiment is not so high, the contribution of the grad q term is negligible. And, by decreasing the size of the discharge cell, the plasma diffuses in the cell sufficiently and fills it up. Therefore, plasmas which are generated in the following experiment can be dealt with as homogeneous ones. Additionally, since the metallic electrodes work as a Faraday shield, the electromagnetic waves are transmitted only in the plasmas and thereby the plasmas can be regarded as a bulk material.

As described above, the configuration, which is an assembly of microplasmas with mesh electrodes, is suitable for the electromagnetic-wave transmission method, and a sufficient absorption of millimeter waves is expected because the thickness of the plasmas are in a submillimeter range, which is a sufficient length compared with the wavelength of the millimeter waves.

3.2.2 Experimental Setup

The electrode configuration of a microplasma array is illustrated in Fig. 3.3 in front view, shown in Fig. 3.3(a), and in cross sectional view, shown in Fig. 3.3(b). The electrode of the microplasma array consists of two metallic meshes, whose size is $50 \times 50 \times 1$ mm^3, coated with alumina. They are in close contact with each other through ceramic screws. Gases, such as nitrogen, water vapor, and oxygen, flowed through the hollows, which confined discharge cells with inlets and outlets, of the electrode to the other side. Each hollow had a length of 1400 μm, a width of 200 μm, and a depth of 1.5 mm. By applying a bipolar pulse voltage, DBDs took place in the hollows. The bipolar pulse voltage, which had a peak value of $V_{0\mathrm{p}}$, was driven continuously, and the intermittent time between positive and negative pulses was fixed as 1 μs. The repetition frequency of this pulse train was adjusted to 5 kHz, and the waveforms observed in the experiment were averaged waveforms of 100 cycles. Figure 3.3(c) shows a photograph of

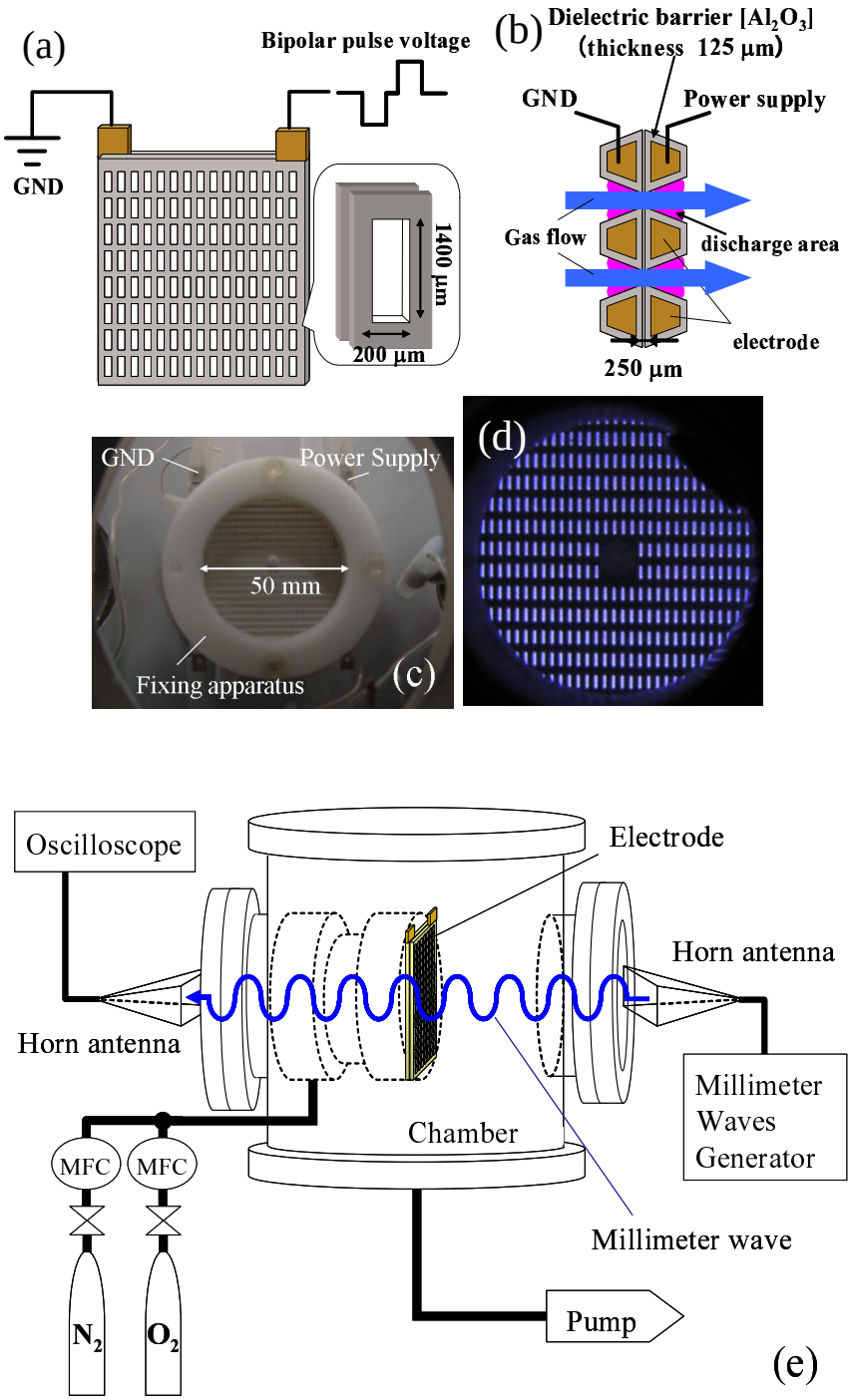

Figure 3.3 Schematic of electrode composition of microplasma array in front view (a) and in cross sectional view (b). Photograph of the electrode with a fixing apparatus (c) and discharge appearance in nitrogen at V_{0p} = 2.05 kV and at a gas flow rate of 1300 sccm (d). (e) shows schematic draw of experimental setup.

the electrode set in the chamber with a doughnut-shaped supporter, so the microplasma array is observed in a circle due to the shape of the supporter as Fig. 3.3(d) shows. Figure 3.3(e) shows a schematic drawing of the experimental setup. To launch and detect millimeter waves, two horn antennas (SGH-10, Millitech Inc.) were used. The transmitting antenna was connected to a wave control unit (83624B, Agilent Technology) through a wave generator (83555A, Agilent Technology). Since the receiving antenna was connected to a detector, which was terminated in an impedance of 1 MΩ, a fast response time of the order of ns were obtained. In this study, the millimeter wave at a frequency of 48.45 GHz was used. To maximize the effect of an equivalent Faraday shield, the oscillation direction of the electric fields of the incident waves was aligned with a direction parallel to the short side of the hollows.

The gas flow rate was controlled by the mass flow controllers (MFCs) in Fig. 3.3(e) and the total gas flow rate was fixed at 1300 sccm (standard cubic centimeter per minute). In the case of admixing water vapors, the gas flowed through a water-bubbling chamber, which was inserted between the MFC and the vacuum chamber. When the water-bubbling chamber was used, water droplets formed on the inside of the tube between the water-bubbling chamber and the vacuum chamber, that is, the water vapor at the saturation level was carried to the vacuum chamber. The saturated vapor pressure of water e_s is obtained by Tetens's equation [3.26]:

$$e_s(t_s) = 0.611 \times 10^{7.5t_s/(t_s+237.3)} \quad \text{kPa}, \tag{3.13}$$

where t_s is the temperature of the system in ℃. The saturated vapor pressure curve of water is shown in Fig. 3.4.

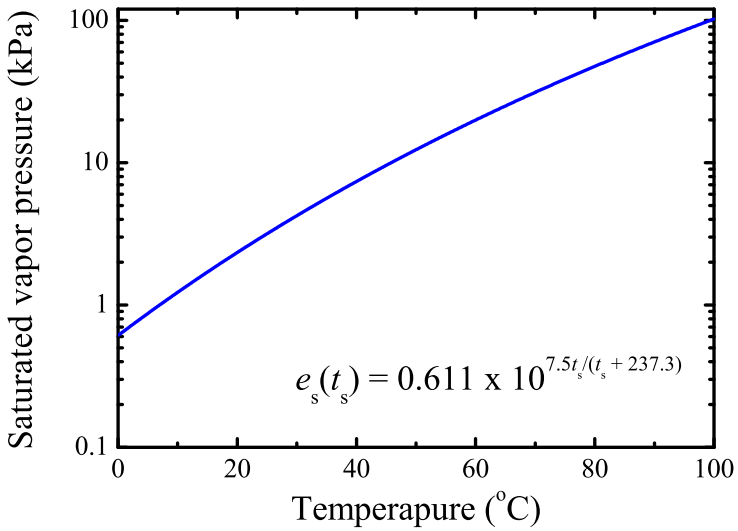

Figure 3.4 Saturated vapor pressure curve of water.

3.3 Experimental Results

3.3.1 Electron Density of Microplasma Array in Pure Nitrogen

Figure 3.5 shows the appearances of a microplasma in the microplasma array with different sizes of hollows in nitrogen and helium. The ignition voltages in nitrogen and in helium at atmospheric pressure were about 0.4 and 1 kV, respectively. In the case of nitrogen, the plasmas stay up against the walls and there is a darker space at the center of the hollow. On the other hand, in the case of helium, the light at the center of the hollow is stronger than that in the vicinity of walls of the hollow. Under this condition, the gas flow prevents impurity particles, such as nitrogen and oxygen detached from the hollow walls, from entering the discharge region; not Penning ionization but the direct and/or the stepwise ionization mainly took place in helium discharges [3.18]. Therefore, the different emission patterns observed for nitrogen and

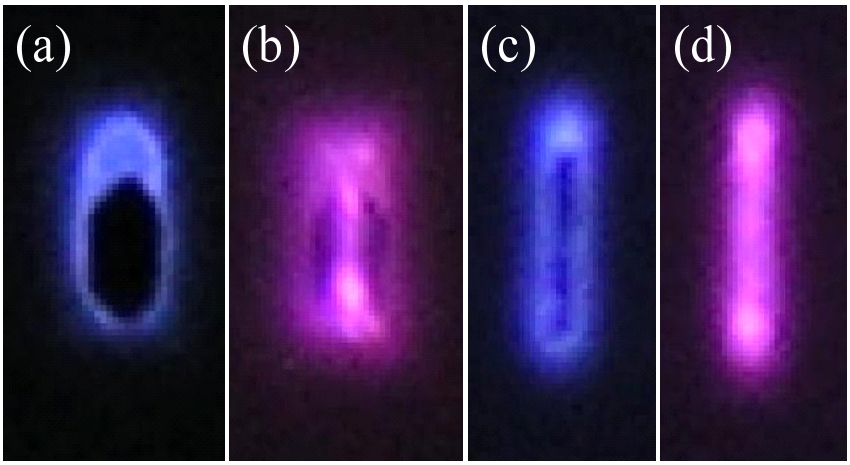

Figure 3.5 Appearances of microplasma at atmospheric pressure with nitrogen in a hollow whose size is 360 × 1000 μm^2 (a), with helium (b), one whose size is 200 × 1400 μm^2 with nitrogen (c), and with helium (d).

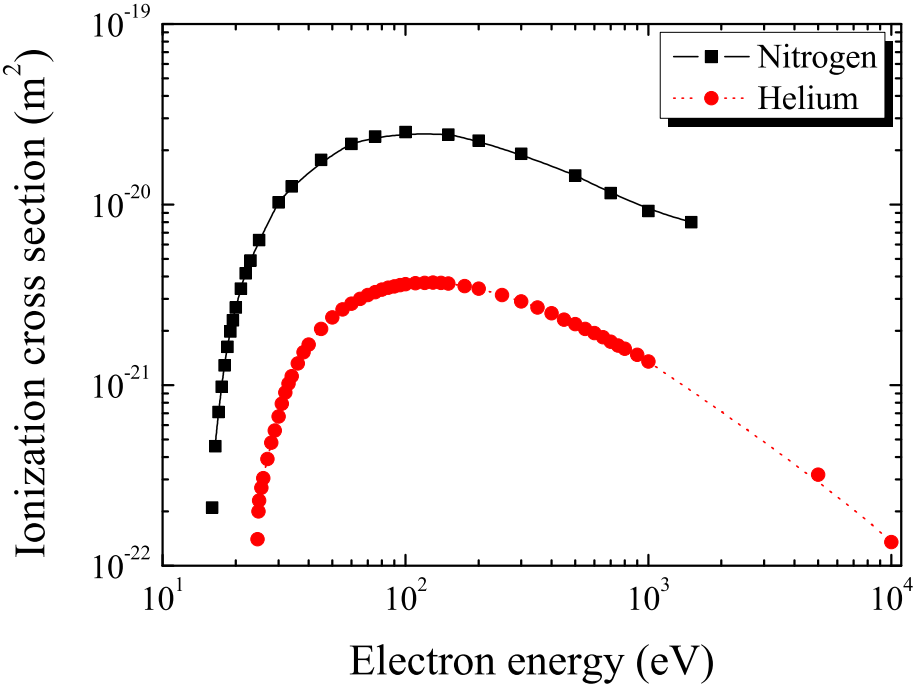

Figure 3.6 Ionization cross section of nitrogen and helium [3.27–29].

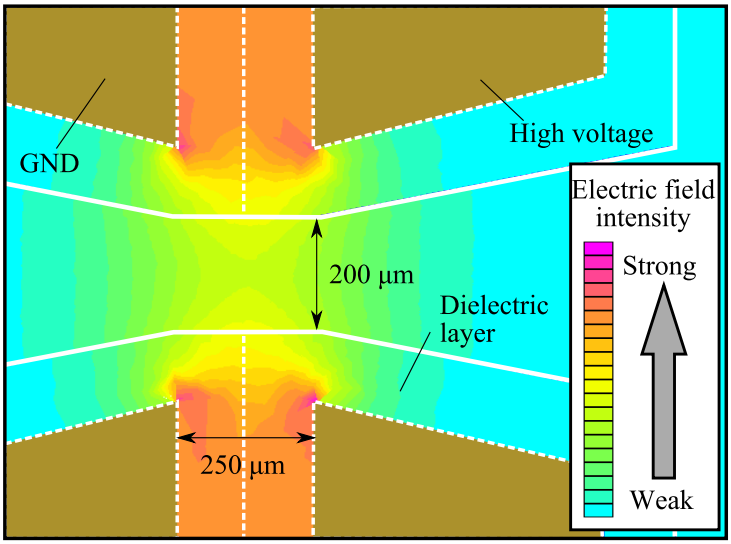

Figure 3.7 Electric field intensity map in a hollow of microplasma array in cross sectional view without plasmas.

helium microplasmas can be explained by the difference in the ionization cross section between nitrogen and helium. The ionization cross section of nitrogen is around ten times higher than that of helium, as shown in Fig. 3.6 [3.27–29]. It means that high energetic electrons that are localized in the bright emission area cannot reach the center of the hollow because discharges in nitrogen take place easily and electrons lose their energy by ionization and excitation of nitrogen molecules. Therefore, by narrowing the hollow, high energetic electrons tend to reach the center of the hollow and discharges take place in almost the entire area of the hollow as Fig. 3.5(c) shows. Hence n_e in nitrogen plasma was measured with the narrow hollow, whose size is 200×1400 μm^2, to investigate more precisely the electron density in it, although the dark space adjacent to the bright emission area might be a bulk plasma region. The electric field intensity map in a hollow of the microplasma array is shown in Fig. 3.7, which was calculated by FEMM (Finite Element Method Magnetics) software package [3.30]. The caluculation condition is shown in Table 3.1. The electric field intensity was relatively large at distances in the

Table 3.1 Calculation condition of electric field intensity map.

High voltage	:	1 kV (Electrostatic field)
Dielectric layer	:	Alumina (Relative permittivity: 3)
Discharge space	:	Air (Relative permittivity: 1)

range 250 - 750 μm centering on the boundary of two mesh electrodes, although this was in a state before the discharges took place. From this result, the thickness of the plasma d was estimated to be 500 μm.

Figures 3.8(a) and (b) show the time evolution of the transmittance T and the electron density n_e in the microplasma array in nitrogen at 40 kPa against the electron temperature T_e = 0.5, 2.0, and 10.0 eV. In Fig. 3.8(a), T was decreased by the plasmas as soon as the discharge current was observed. The decrease when a negative voltage was applied was greater than that when a positive one was applied. This was responsible for the increase in n_e due to the enhancement of the effective electric field by accumulated charges on the surfaces of the dielectric layer. The decay time of n_e was also different between positive and negative phases. The decay time in the positive phase was about 1.1 μs and the one in the negative phase was about 0.5 μs. It is thought that this difference was due to the change in the density profile of ions in the discharge space which affects three-body recombination. In Fig. 3.8(b), n_e was not so sensitive to the value of T_e because the electron elastic collision cross section is proportional to the square root of T_e. Therefore, in what follows, 0.5 eV was selected as the moderate value of T_e. In the case of T_e = 0.5 eV, the electron elastic collision cross section was set to 1.1×10^{-15} cm^2. The peak value of n_e was 1.5 - 2 $\times 10^{13}$ cm^{-3}, which was about 10 times higher than the value of the microplasma array in helium, as shown in Fig. 3.9 [3.18, 19]. In the case of helium plasma, n_e decreased gradually after the discharge current stopped because electrons are produced not

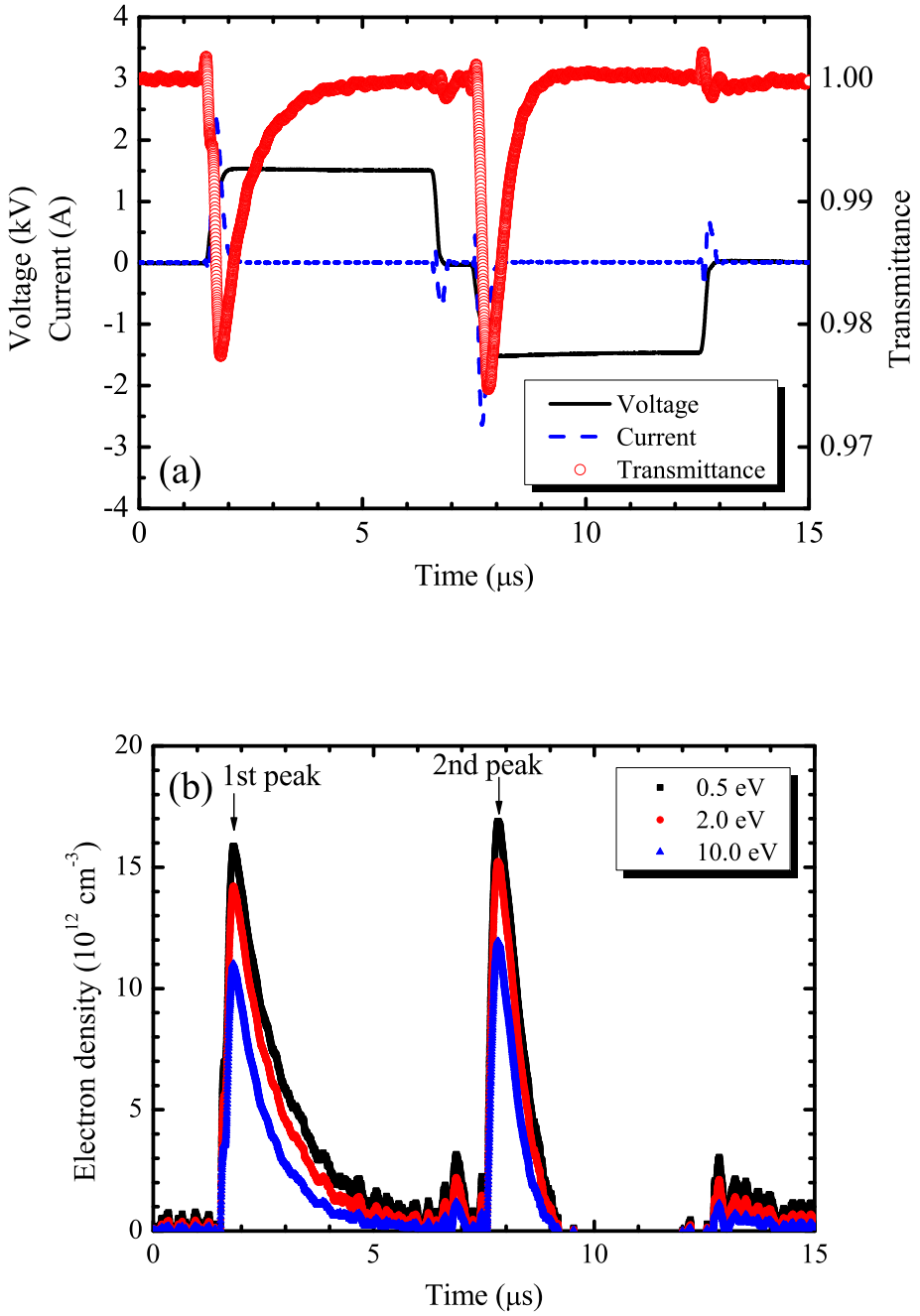

Figure 3.8 Time evolution of transmittance of millimeter waves through microplasma array in nitrogen (a) and calculated electron density in that (b) at 40 kPa and V_{0p} = 1.52 kV against the electron temperature of 0.5, 2.0 and 10.0 eV.

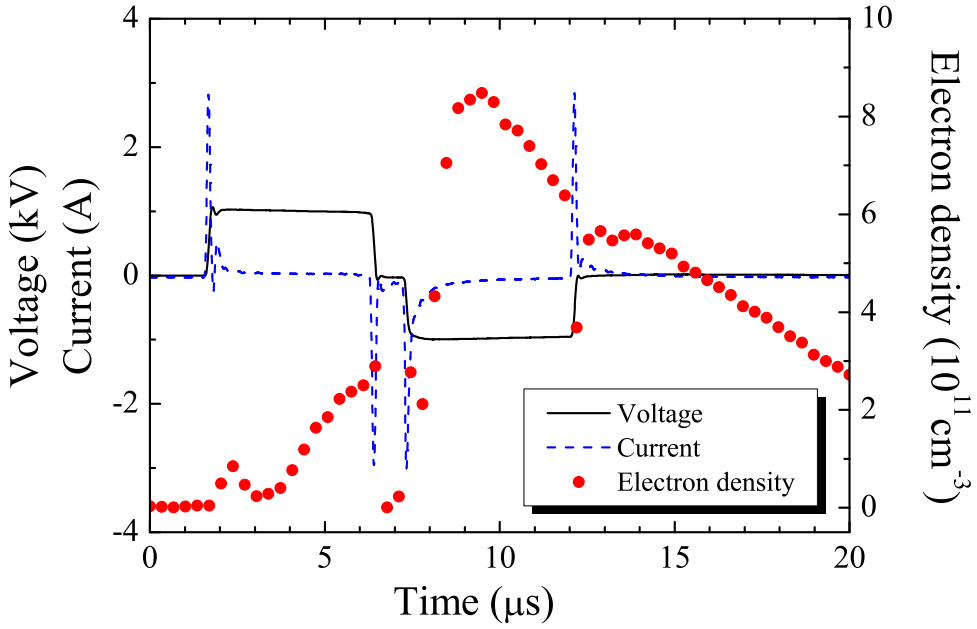

Figure 3.9 Calculated electron density in microplasma array in helium at atmospheric pressure at V_{0p} = 1.06 kV and at a gas flow rate of 2000 sccm.

only by the direct ionization from the ground state of helium atoms but also by other processes, such as the Penning processes as long as the metastable atoms remain in the afterglow phase [3.17, 19]. In contrast, in the case of nitrogen plasma, the decrease in T arose and disappeared instantaneously. This fact indicates that the main mechanism of the generation and the loss of electrons is the direct ionization of nitrogen molecules and the recombination of nitrogen ions. The particle balance in nitrogen plasmas will be discussed with ionization and recombination processes in Section 3.4.

Figure 3.10 shows T through the microplasma array in nitrogen at low pressure. V_{0p} was 2.14, 1.94, and 1.74 kV at 80, 53, and 27 kPa, respectively. On the leading edge of pulse voltages, there were slight noises of transmittance signals originating from the change in the conductance in the discharge region whether the plasma existed or not. However, the noises

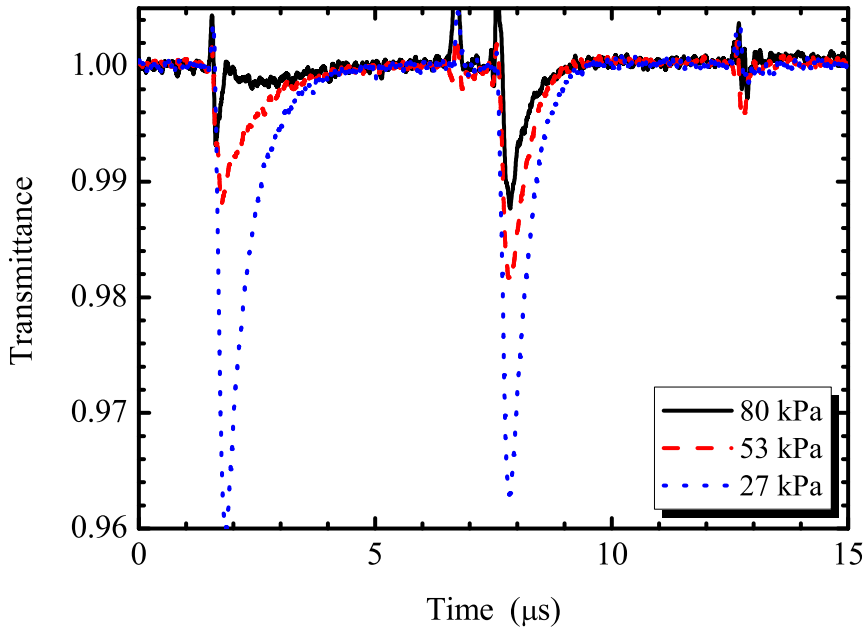

Figure 3.10 Transmittance of millimeter waves through microplasma array in nitrogen at low pressure.

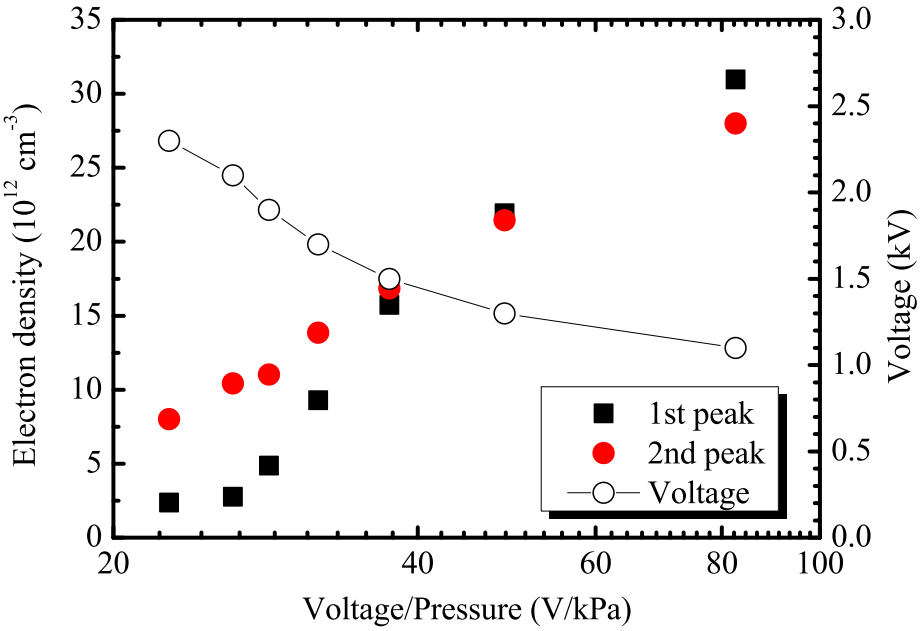

Figure 3.11 Electron density in microplasma array as a function of V/p in nitrogen.

hardly affected the calculation of the maximum of n_e because their influence was small at the peaks of T. From this figure, the absorbance of the millimeter wave increased with a decrease in pressure. This is due to reduction in the ionization collision frequency and enhancement of the reduced electric field E/p by a decrease in pressure. At high pressure, T was weak because the spatially averaged electron density was lower than that at lower pressure. However, the 2nd peak at every pressure and the 1st peak at low pressure were clear with enough signal-to-noise ratio. Therefore the value is validated particularly at the 2nd peak.

From this result, n_e in the microplasma array in nitrogen as a function of quotient of voltage and pressure V/p was calculated as shown in Fig. 3.11. n_e at atmospheric pressure was estimated to be 5×10^{12} cm^{-3}, and increased monotonously with V/p. And n_e at the 1st and 2nd peaks reached almost the same value at high V/p. This might be because the recombination of the wall charge reduced as p became lower, that is, V/p became higher.

3.3.2 Electron Density of Microplasma Array in Nitrogen with Water Vapor

T through the microplasma array in nitrogen with H_2O is shown in Fig. 3.12. In this case, the partial pressure of H_2O was estimated to be 3.1 kPa from the saturated vapor pressure of H_2O at room temperature as shown in Fig. 3.4, and the applied voltages were similar to those in the case of pure nitrogen. As in the case without H_2O, the absorbance of millimeter waves increased when total pressure decreased. This is due to the lower collision frequency and enhancement of E/p by decrease in total pressure. However, with H_2O, the absorbance of millimeter waves is smaller than that without H_2O.

Figure 3.13 shows n_e in the microplasma array in nitrogen with H_2O as a function of V/p. In this case, n_e was of the order of 10^{12} cm^{-3} and increased with larger V/p. However, the rate of

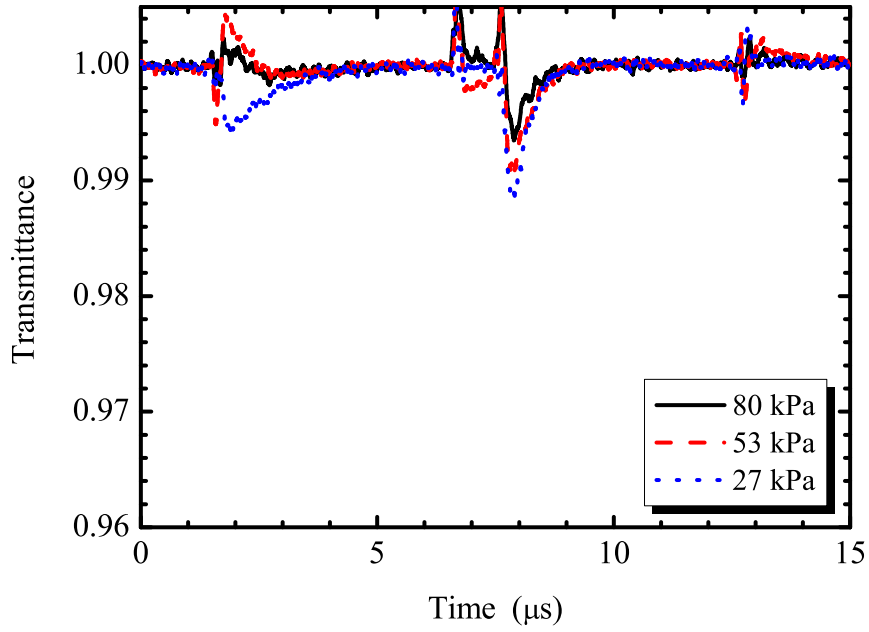

Figure 3.12 Transmittance of millimeter waves through microplasma array in nitrogen at low pressure with addition of H_2O of 3.1 kPa.

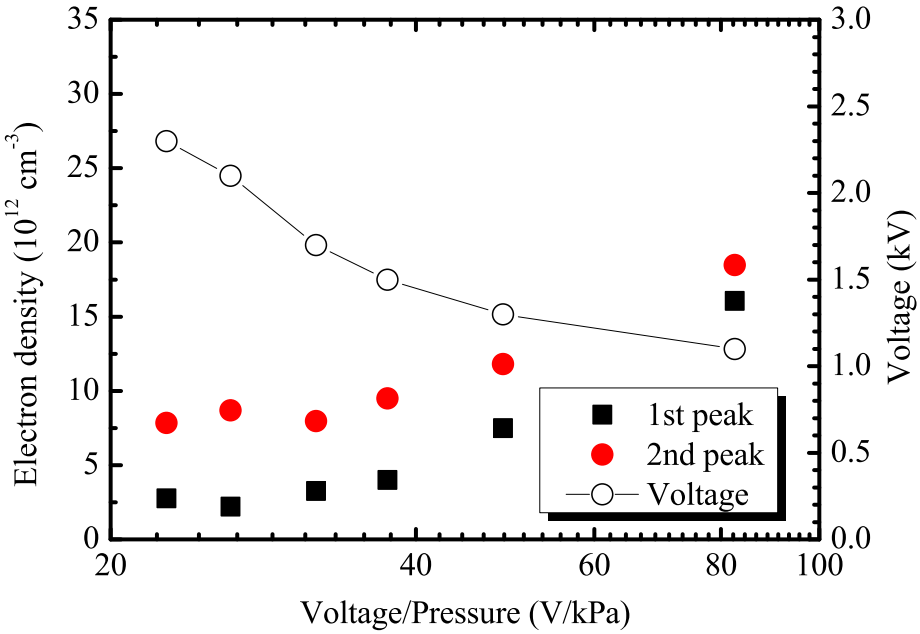

Figure 3.13 Electron density in microplasma array as a function of V/p with addition of H_2O of 3.1 kPa.

increase of n_e with V/p was smaller than that without H_2O, and n_e with H_2O at $V/p = 82$ V/kPa was only about half of that with H_2O. This is due to the relative increase in the partial vapor pressure because the partial pressure of H_2O was a constant value of 3.1 kPa. Consider only the elastic collision for the sake of simplicity since usually elastic scattering cross sections are much larger than inelastic collision cross sections. The mean free path of an electron in N_2 and H_2O is calculated as 3.6×10^{-5} and 2.4×10^{-5} cm from the kinetic theory at room temperature and at atmospheric pressure [3.31]. Therefore, an increase in the partial vapor pressure will lead to a decrease in energetic electrons. This effect and the effect of E/p give rise to the minimum of n_e when V/p is around 30 V/kPa. Furthermore, H_2O works as an electronegative gas and undergoes electron attachment. These effects might cause the restraining of the increase in n_e.

3.3.3 Electron Density of Microplasma Array in Nitrogen with Oxygen

Figure 3.14 shows n_e in the microplasma array in nitrogen with a small admixture of O_2 at atmospheric pressure. V_{0p} was 2.36 kV, which was similar to that in the case of pure nitrogen at atmospheric pressure. In this figure, the 1st peak means n_e when the positive pulse voltage was applied to the microplasma array and the 2nd peak means that when the negative pulse voltage was applied. In both cases, n_e decreased with increasing O_2 flow fraction except for around 0.5%. According to Mankelevich *et al.* [3.32], the following reactions are effective at less than 1% O_2 flow fraction:

$$N(^2P) + O(^3P) \rightarrow NO^+ + e, \tag{3.14}$$

$$N(^4S) + O(^1S) \rightarrow NO^+ + e. \tag{3.15}$$

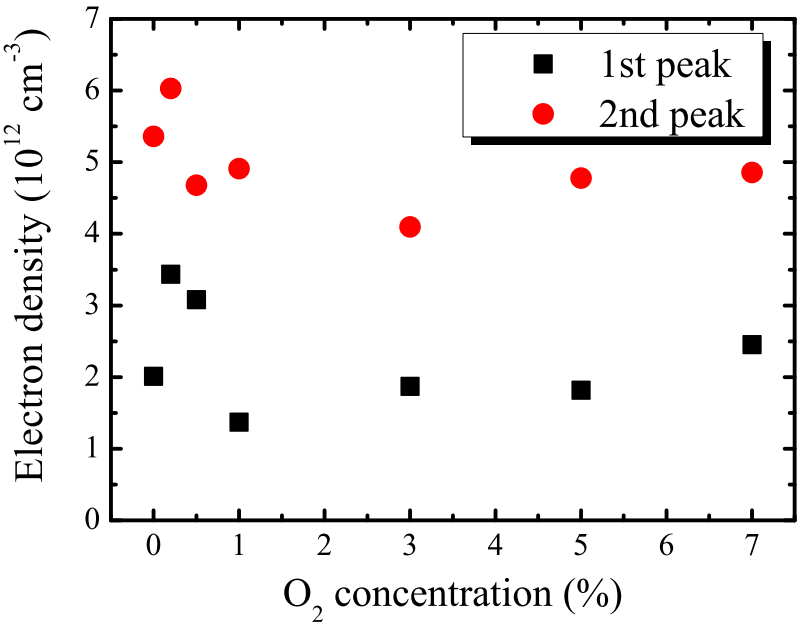

Figure 3.14 Electron density in microplasma array in nitrogen with small admixtures of oxygen.

As the concentration of O_2 increased, n_e decreased because of the quenching of O atoms through the formation of O_3 molecules and the effect of electron attachment by oxygen.

3.4 Discussion

3.4.1 Particle Balance Model in Nitrogen Plasma

In the case of nitrogen discharge, the generation of electrons is mainly by direct ionization:

$$N_2 + e \rightarrow N_2^+ + 2e \qquad K_{3.16} = f(E/p). \tag{3.16}$$

In the afterglow discharge in nitrogen at atmospheric pressure, the possible main reactions of recombination are

$$N_4^+ + e \rightarrow N_2(C^3\Pi_u) + N_2 \qquad K_{3.17} = 2.0 \times 10^{-6} \left(\frac{T_g}{T_e}\right)^{0.5} \text{cm}^3/\text{s}, \tag{3.17}$$

$$N_2^+ + N_2 + e \rightarrow 2N_2 \qquad K_{3.18} = 6.0 \times 10^{-27} \left(\frac{T_g}{T_e}\right)^{1.5} \text{cm}^6/\text{s}. \tag{3.18}$$

Here T_g is gas temperature, and T_e and T_g are in kelvin. A N_4^+ ion is generated by the following reaction:

$$N_2^+ + 2N_2 \rightarrow N_4^+ + N_2 \qquad K_{3.19} = 5.0 \times 10^{-29} \text{cm}^6/\text{s}. \tag{3.19}$$

The rate coefficients used here are taken from Kossyi *et al.*'s report [3.33]. For simplifying, it is assumed that n_e and the density of positive ions are 10^{13} cm^{-3} by the electroneutrality condition. The decay time of N_2^+ by equation (3.18) on the assumption that T_g = 300 K and T_e = 1 eV at atmospheric pressure is 1.5×10^{-4} s. On the other hand, the decay time of N_2^+ by equation (3.19) is 2.7×10^{-11} s, and that of N_4^+ and electrons by equation (3.17) is 3.1×10^{-7} s. Therefore the loss process of electron is governed mainly by equation (3.17).

Figure 3.15 shows the rate coefficient of reactions (3.16) and (3.17). $K_{3.16}$ was computed by the Boltzmann code BOLSIG [3.34]. As E/p increases, the rate coefficient of reaction (3.16), corresponding to the generation of the electron, increases drastically. On the other hand, reaction (3.17), corresponding to the loss of the electron, decreases as E/p increases. This tendency causes n_e to increase with increasing V/p as Fig. 3.11 shows. In this case, n_e was calculated

[†] Although the reduced electric field E/p is generally expressed in V/cm/Torr (1 Torr ≈ 0.133 kPa), it is expressed in V/cm/kPa in this dissertation.

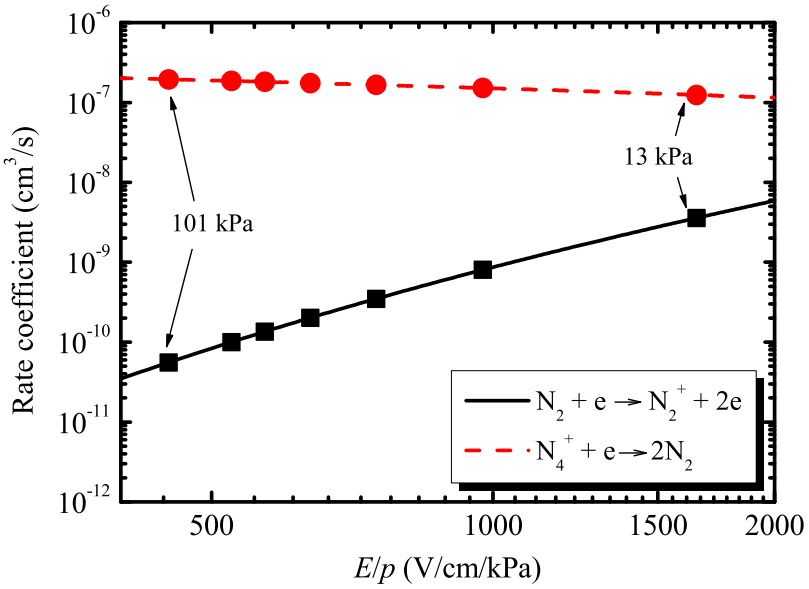

Figure 3.15 Rate coefficient of reactions as a function of E/p[†].

by these rate coefficients by assuming T_e = 1.3 eV under the steady-state condition, and was estimated to be 5.2×10^{12} cm^{-3} at atmospheric pressure. Although this estimation is rough because there are the effects of wall charge and some excited states of nitrogen molecules and atomic nitrogen, that is, detailed calculation is required considering those effects to understand the mechanism of the microplasma array in nitrogen, this value fairly agrees with the experimental value. Consequently, the validity of the millimeter-wave transmission method for the measurement of electron density in nitrogen near and at atmospheric pressure was confirmed.

3.4.2 Effects of Small Admixture of Water Vapor and Oxygen

In the case of a small admixture of H_2O, at high pressure, the effect of H_2O is negligible and the discharge mechanism is the same as the case without H_2O. Meanwhile, at low pressure, the dissociative attachment reactions cause the decrease in n_e because of the increase in partial

pressure of H_2O:

$$H_2O + e \rightarrow H + OH^-, \tag{3.20}$$

$$H_2O + e \rightarrow H_2 + O^-, \tag{3.21}$$

$$H_2O + e \rightarrow H^- + OH. \tag{3.22}$$

These reactions are effective over the range from 5 to 15 eV [3.35]. Generally, at high E/p, T_e is also high. This fact leads to the difference between n_e with and without H_2O. However, various species, such as O, OH, H radicals, and positive and negative ions, are generated by the disassociation of H_2O. Thus the reactions in nitrogen with H_2O are complicated, and thereby more data of T_e are required to investigate n_e quantitatively. Nevertheless, the reduction in n_e by the addition of H_2O can be explained by the dissociative attachment reactions, and n_e was obtained without considering those complicated reactions by the millimeter-wave transmission method.

In the case with oxygen, the following reactions affect n_e:

$$O_2 + e \rightarrow O_2^+ + 2e \qquad K_{3.23} = f(E/p), \tag{3.23}$$

$$O_2 + e \rightarrow O^- + O \qquad K_{3.24} = f(E/p), \tag{3.24}$$

$O_2 + O_2 + e \rightarrow O_2^- + O_2$

$$K_{3.25} = 1.4 \times 10^{-29} \left(\frac{T_g}{T_e}\right) \exp\left(-\frac{600\,\mathrm{K}}{T_g}\right) \times \exp\left[\frac{700\,\mathrm{K} \times (T_e - T_g)}{T_e T_g}\right] \mathrm{cm}^6/\mathrm{s}, \tag{3.25}$$

$O_2 + N_2 + e \rightarrow O_2^- + N_2$

$$K_{3.26} = 1.07 \times 10^{-31} \left(\frac{T_g}{T_e}\right)^2 \exp\left(-\frac{70\,\mathrm{K}}{T_g}\right) \times \exp\left[\frac{1500\,\mathrm{K} \times (T_e - T_g)}{T_e T_g}\right] \mathrm{cm}^6/\mathrm{s}. \tag{3.26}$$

The rate coefficients of reactions (3.23) and (3.24) are almost the same value at around E/p = 525 V/cm/kPa. Therefore, reactions (3.25) and (3.26) affect n_e, and the time evolution of n_e is calculated by

$$\frac{dn_e}{dt} = K_{3.16}[N_2]n_e - K_{3.17}[N_4^+]n_e - K_{3.25}[O_2]^2 n_e - K_{3.26}[O_2][N_2]n_e. \tag{3.27}$$

From this equation, τ of the decay time of n_e is

$$\tau = \left\{K_{3.16}[N_2] - K_{3.17}[N_4^+] - K_{3.25}[O_2]^2 - K_{3.26}[O_2][N_2]\right\}^{-1}. \tag{3.28}$$

Therefore, in the case of admixture of O_2 in nitrogen, n_e decreases with an increase in the ratio of O_2. At a small concentration of O_2, reactions (3.25) and (3.26) are not effective, and the peak of n_e at less than 1% of O_2 can be explained as mentioned in Section 3.3.3. Although the limited data obtained in this experiment cannot confirm the mechanism in detail, it is obvious that a small amount of O_2 affects n_e of microdischarges in nitrogen.

At high H_2O and O_2 concentrations, there might be a significant number of negative ions. However, the negative ions are heavy as well as positive ions, and the total charge of ions including negative ions and that of electrons are equal if electroneutrality is maintained. Therefore, the negative ions do not affect the measurement of ω_{pe}.

3.5 Summary

The electron density in the microplasma array in nitrogen with a small admixture of H_2O and O_2 at atmospheric pressure was measured by the millimeter-wave transmission method.

Thereby, it was found that the electron density in nitrogen was about 5×10^{12} cm^{-3}, which was confirmed by a simple particle-balance model. And in the case of a small admixture of H_2O, the electron density was not much affected by H_2O. However, as the partial pressure of H_2O increased, the electron density became lower. On the other hand, in the case of a small admixture of O_2 at less than 1% in nitrogen, the electron density was increased, and more than 1% of O_2 decreased the electron density by electron attachment. Finally, in every case, the electron density was of the order of 10^{12} - 10^{13} cm^{-3} in the microplasma array, and the millimeter-wave transmission method was suitable to diagnose these plasmas at atmospheric pressure.

References

[3.1] G. Borcia, A. Chiper and I. Rusu: Plasma Sources Sci. Technol. **15**, 849 (2006).

[3.2] S. Y. Moon, J. W. Han and W. Choe: Thin Solid Films **506-507**, 355 (2006).

[3.3] T. Ideno and T. Ichiki: Thin Solid Films **506-507**, 235 (2006).

[3.4] M.-H. Jung and H.-S. Choi: Thin Solid Films **515**, 2295 (2006).

[3.5] X. Xu, L. Li, S. Wang, L. Zhao and T. Ye: Plasma Sources Sci. Technol. **16**, 372 (2007).

[3.6] H. Liang and R. G. Gordon: J. Mater. Sci. **42**, 6388 (2007).

[3.7] Y. S. Akishev, M. E. Grushin, I. V. Kochetov, A. P. Napartovich, M. V. Pan'kin and N. I. Trushkin: Plasma Phys. Rep. **26**, 157 (2000).

[3.8] C. Yang, K. Ingeneri and W. W. Harrison: J. Anal. At. Spectrom. **14**, 693 (1999).

[3.9] S. Okazaki, M. Kogoma, M. Uehara and Y. Kimura: J. Phys. D: Appl. Phys. **26**, 889 (1993).

[3.10] T. Somekawa, T. Shirafuji, O. Sakai, K. Tachibana and K. Matsunaga: J. Phys. D: Appl. Phys. **38**, 1910 (2005).

[3.11] S. N. Abolmasov, T. Shirafuji and K. Tachibana: IEEE Trans. Plasma Sci. **33**, 941 (2005).

[3.12] K. Tachibana: IEEJ Trans. Electr. Electron. Eng. **1**, 145 (2006).

[3.13] F. Iza, G. J. Kim, S. M. Lee, J. K. Lee, J. L. Walsh, Y. T. Zhang and M. G. Kong: Plasma Process. Polym. **5**, 322 (2008).

[3.14] S. Hassaballa, K. Tomita, Y. K. Kim, K. Uchino, H. Hatanaka, Y. M. Kim, C. H. Park and K. Muraoka: Jpn. J. Appl. Phys. **44**, L442 (2005).

[3.15] M. N. Shneider and R. B. Miles: J. Appl. Phys. **98**, 033301 (2005).

[3.16] X. P. Lu and M. Laroussi: Appl. Phys. Lett. **92**, 051501 (2008).

[3.17] K. Tachibana, Y. Kishimoto, S. Kawai, T. Sakaguchi and O. Sakai: Plasma Phys. Control. Fusion **47**, A167 (2005).

[3.18] O. Sakai, Y. Kishimoto and K. Tachibana: J. Phys. D: Appl. Phys. **38**, 431 (2005).

[3.19] K. Tachibana, Y. Kishimoto and O. Sakai: J. Appl. Phys. **97**, 123301 (2005).

[3.20] O. Sakai, T. Sakaguchi, Y. Ito and K. Tachibana: Plasma Phys. Control. Fusion **47**, B617 (2005).

[3.21] O. Sakai, T. Sakaguchi and K. Tachibana: Appl. Phys. Lett. **87**, 241505 (2005).

[3.22] O. Sakai, K. Tachibana, K. Tatsugawa, K. Ohishi and R. Inoue: Trans. Mater. Res. Soc. Jpn. **31**, 453 (2006).

[3.23] J. D. Swift and M. J. R. Schwar: *Electrical Probes for Plasma Diagnostics* (Iliffe Books, London, 1970).

[3.24] I. H. Hutchinson: *Principles of Plasma Diagnostics* (Cambridge University Press, Cambridge, 1990).

[3.25] M. P. Bachynski and K. A. Graf: RCA Rev. **25**, 3 (1964).

[3.26] O. Tetens: Z. Geophys. **6**, 297 (1930).

[3.27] D. Rapp and P. Englander-Golden: J. Chem. Phys. **43**, 1464 (1965).

[3.28] R. G. Montague, M. F. A. Harrison and A. C. H. Smith: J. Phys. B: At. Mol. Phys. **17**, 3295 (1984).

[3.29] A. V. Phelps and L. C. Pitchford: Phys. Rev. A **31**, 2932 (1985).

[3.30] *FEMM*, http://femm.foster-miller.net (2006).

[3.31] E. E. McDaniel: *Collision Phenomena in Ionized Gases* (Wiley, New York, 1964).

[3.32] Y. A. Mankelevich, A. F. Pal', N. A. Popov, T. V. Rakhimova and A. V. Filippov: Plasma

Phys. Rep. **27**, 979 (2001).

[3.33] I. A. Kossyi, A. Y. Kostinsky, A. A. Matveyev and V. P. Silakov: Plasma Sources Sci. Technol. **1**, 207 (1992).

[3.34] G. J. M. Hagelaar and L. C. Pitchford: Plasma Sources Sci. Technol. **14**, 722 (2005).

[3.35] Y. Itikawa: *Molecular Processes in Plasmas* (Springer, Berlin, 2007).

Chapter 4

Effects of Capacitance in Deposition System Using Atmospheric-Pressure Plasma Jet†

4.1 Introduction

Plasma-processing techniques at atmospheric pressure are of strong practical interest because they have high potential to simplify material processes by avoiding the use of vacuum systems. However, plasmas at atmospheric pressure tend to be constricted and localize, and it is usually difficult to apply them to large-area processes. To avoid the difficulty, the investigation of small plasmas (microplasmas) [4.1] as the plasma sources in material processing has been progressing by integrating [4.2–4] or scanning [4.5] them.

Recently, various studies have been performed on atmospheric-pressure plasma jets (APPJs), since they are useful in material processes [4.6–8]. The APPJ used in this study is similar to that of Engemann's group [4.9], and is generated in a helium gas flow by supplying a high AC voltage with a kHz-order frequency. As shown in Chapter 2, the discharge mechanism in the helium gas channel has been proved to be similar to a positive corona discharge, and the gas temperature of the APPJ remains as low as 300 K [4.10, 11]. This is beneficial for performing material processes at low temperature to avoid thermal damage. The APPJ can also produce a

†This Chapter, in slightly altered form, is published in: Y. Ito, Y. Fukui, K. Urabe, O. Sakai and K. Tachibana, "Effect of Series Capacitance and Accumulated Charge on a Substrate in a Deposition Process with an Atmospheric-Pressure Plasma Jet", Japanese Journal of Applied Physics **49**, 066201 (2010).

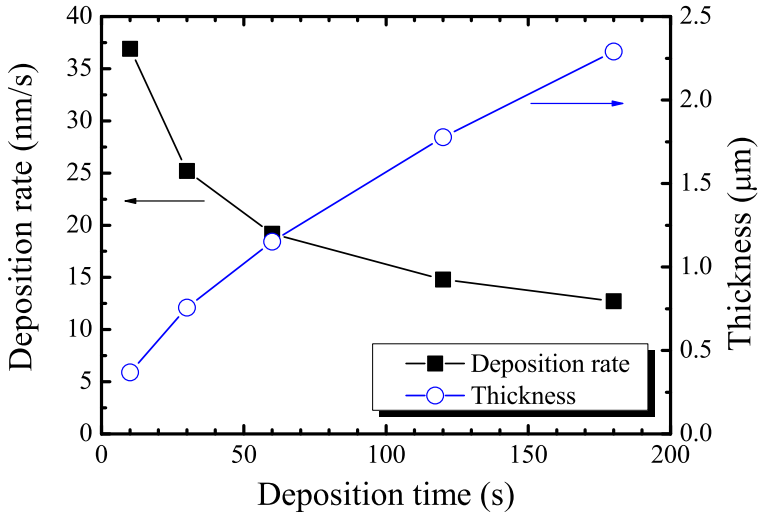

Figure 4.1 Deposition rate of SiO_2 film obtained from TEOS by PE-CVD with APPJ onto a fixed point on the Si substrate at the substrate temperature of 140℃.

large number of radicals in the ambient air; Furusho *et al.* have applied the APPJ to the synthesis of gold nanoparticles [4.12]. When a grounded electrode is placed about 5 cm away from the exit of the plasma jet, the discharge mechanism changes from the positive corona mode to the dielectric-barrier discharge (DBD) mode after the streamer head reaches the electrode above a certain applied voltage.

This APPJ have been applied to the plasma enhanced chemical vapor deposition (PE-CVD) of oxide materials from organic sources, and it was reported that it is possible to deposit SiO_2 thin films at a deposition rate of as high as 300 nm/s [4.13]. Therefore, the PE-CVD system is a useful tool for high-speed and localized maskless deposition of oxide materials.

However, a substrate covered by an insulating layer is charged up during PE-CVD with the APPJ, which prevents the progress of the deposition process when a low-frequency power supply is used. Actually, when SiO_2 thin-film deposition was carried out onto an insulating substrate, or continuous deposition at a point of a conductive substrate, the deposition rate markedly

Table 4.1 Deposition condition.

Configuration	:	Cross (vertical APPJ and tilted TEOS, shown in Chapter 5)
Power source	:	Bipolar impulse (V_{0p} =6 kV, 5 kHz)
Substrate temperature	:	140℃
Helium for APPJ	:	2 L/min
TEOS	:	0.1 g/min
Carriage gas	:	Helium (2.8 L/min)

decreased with increasing deposition time as shown in Fig. 4.1, and the deposition condition is listed in Table 4.1. From this fact, it is suspected that the plasma jet is affected by the accumulated charge on the substrate surface, which depends on the capacitance formed on the substrate surface.

In this chapter, the discharge current flowing into a conductive substrate connected to a variable capacitor in series and placed at a certain distance downstream of the APPJ was measured to clarify the effect of the accumulated charge on the deposition process. From this experiment, the accumulated charge, which varied with the total capacitance of the system was estimated. And its effect on the deposition of oxide materials was investigated by a comparison with the measured deposition rate. In practice, the deposition rate of SiO_2 onto a Si substrate was measured. The substrate was placed on a metal plate with an insulating spacer composed of thin glass plates, the number of which determined the capacitance. In addition, an equivalent circuit model of the system was considered to theoretically verify the validity of the supposition.

4.2 Experimental Setups

Figures 4.2(a) and (b) show the system used for the measurement of the accumulated charge on the substrate surface. The plasma jet consisted of a glass capillary of 3-mm inner diameter

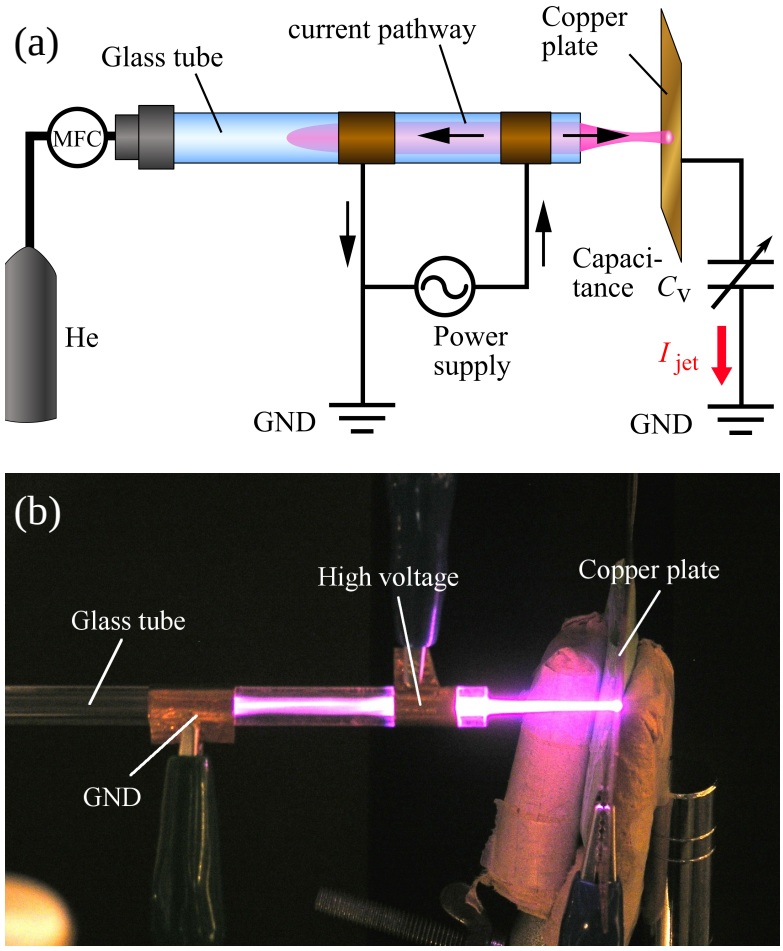

Figure 4.2 Scheme and photograph of the experimental setup: scheme for measuring the discharge current I_{jet} (a) and appearance of APPJ at V_{0p} = 7 kV (b).

and 6-mm outer diameter, and two tubular electrodes. One electrode of 10-mm length was placed 5 mm from a nozzle exit of the plasma jet for use as a high-voltage electrode, to which a bipolar impulse-voltage train was applied at a frequency of 10 kHz [4.14]. The waveform had an impulse peak with a ringing tail. The other electrode of 13-mm length was used as a grounded electrode and was placed 25 mm from the high-voltage electrode. A copper plate connected to the grounded potential through the capacitance C_v was located 20 mm from the exit of the plasma jet. By supplying helium gas at a flow rate of 2 L/min into the glass capillary and applying a bipolar impulse voltage with an amplitude V_{0p} of more than 5 kV between two

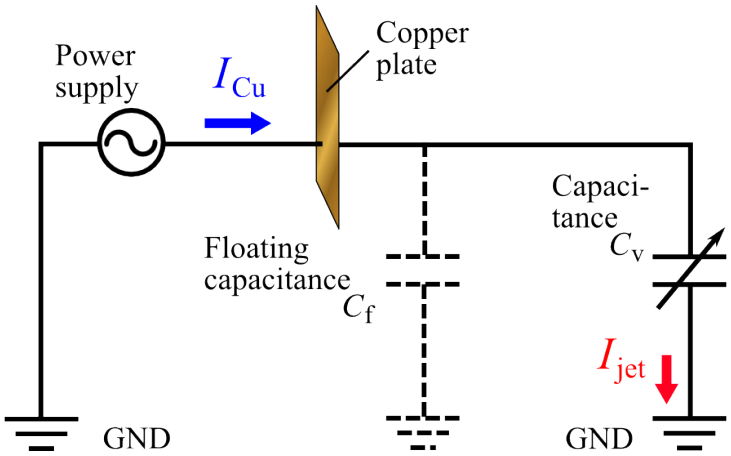

Figure 4.3 Schematic draw of circuit diagram for estimating the floating capacitance.

tubular electrodes, a plasma column was generated inside the capillary and a long thin plasma plume propagated into the ambient air.

The discharge current had two paths: one was between the two tubular electrodes inside the glass capillary and the other was between the front (high-voltage) tubular electrode and the copper plate through the plasma plume. These discharge paths were independent of each other, i.e., the charge accumulated on the wall as a result of the DBD between the two tubular electrodes was constant at a given applied voltage even when the discharge current between the high-voltage electrode and the copper plate I_{jet} was changed with the series capacitance C_v. Thus, the accumulated charge Q can be changed independently by varying C_v. Q was calculated by integrating I_{jet} over the impulse peak in the positive phase of the applied voltage while ignoring the effect of the ringing tail, where Q is defined by the following expression:

$$Q = \int I_{jet}(t)\, dt. \tag{4.1}$$

Figure 4.3 is a schematic drawing of the apparatus used for estimating the floating capacitance

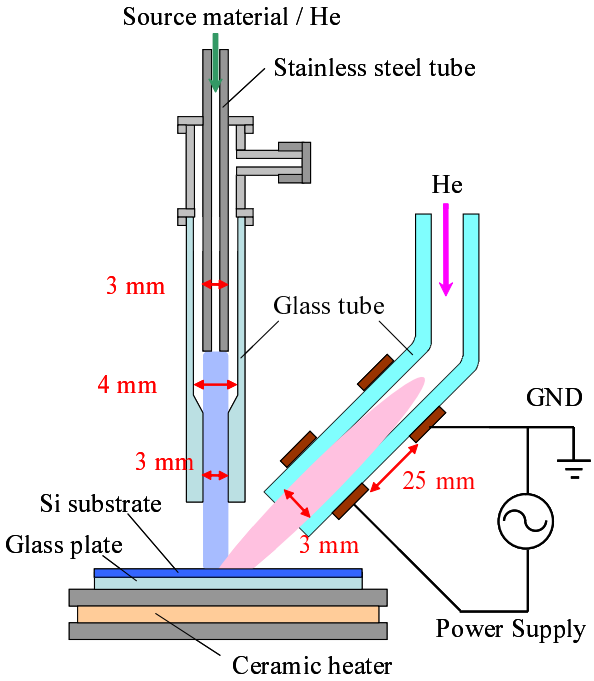

Figure 4.4 Experimental setup for measuring the deposition rate of SiO_2.

C_f. The bipolar impulse voltage of V_{0p} = 500 V was applied to the copper plate directly, and the total current that flowed into the copper plate I_{Cu}, and the discharge current I_{jet} flowing through the variable capacitor were measured separately.

Figure 4.4 shows the experimental setup for the measurement of the deposition rate of SiO_2 onto a Si substrate placed on a spacer consisting of glass plates. Tetraethoxysilane (TEOS) was used as the source material. The procedure for the PE-CVD was the same as that described previously [4.13]; the vaporized TEOS was carried by helium gas at a flow rate of 2.8 L/min and the helium flow rate for the APPJ was 2 L/min. The number of the glass plates composing the spacer between the substrate and the stage, each of which had a thickness of 0.12 mm, was changed to vary the value of C_v. In this experiment, the deposition of SiO_2 was carried out at a fixed point without moving the stage.

4.3 Experimental Results

4.3.1 Accumulated Charge on Substrate

Figure 4.5 shows waveforms of the discharge current I_{jet} measured at various values of V_{0p}. The charge balance in the entire system was maintained and the exchange of charges occurred between two tubular electrodes, leading to the discharge current I_{jet} at a positive applied voltage being larger than that when the applied voltage was negative. In the positive phase of the applied voltage, the peak value of I_{jet} increased with increasing V_{0p}. In addition, the timing when I_{jet} becomes 0 is almost the same at all values of C_v from 5 to 1000 pF. In the positive phase, a positive corona discharge took place from the high-voltage electrode to the copper plate through the helium gas channel when the applied voltage reached about 5 kV. To be precise, I_{jet} began to increase about 1 μs after the applied voltage reached 5 kV. Supposing that the traveling speed of the streamer head of the positive corona discharge is 20 km/s based on the previous measurement [4.11], then it takes 1 μs to travel the 2 cm between the nozzle exit of the plasma jet and the copper plate. Therefore, the timing when I_{jet} begins to rise coincides closely with the time when the streamer head reaches the copper plate. On the other hand, in the negative phase, I_{jet} increased abruptly with time when V_{0p} was 6.5 kV or higher. This indicates that I_{jet} flows in the DBD following the positive corona discharge in the positive phase of the applied voltage even when V_{0p} is 6 kV or lower. In contrast, in the negative phase, the DBD does not take place until the applied voltage reaches a certain threshold value. Additionally, I_{jet} decreased as C_v was reduced, especially below 100 pF.

Figure 4.6(a) shows the time evolution of I_{jet} and the accumulated charge Q calculated by

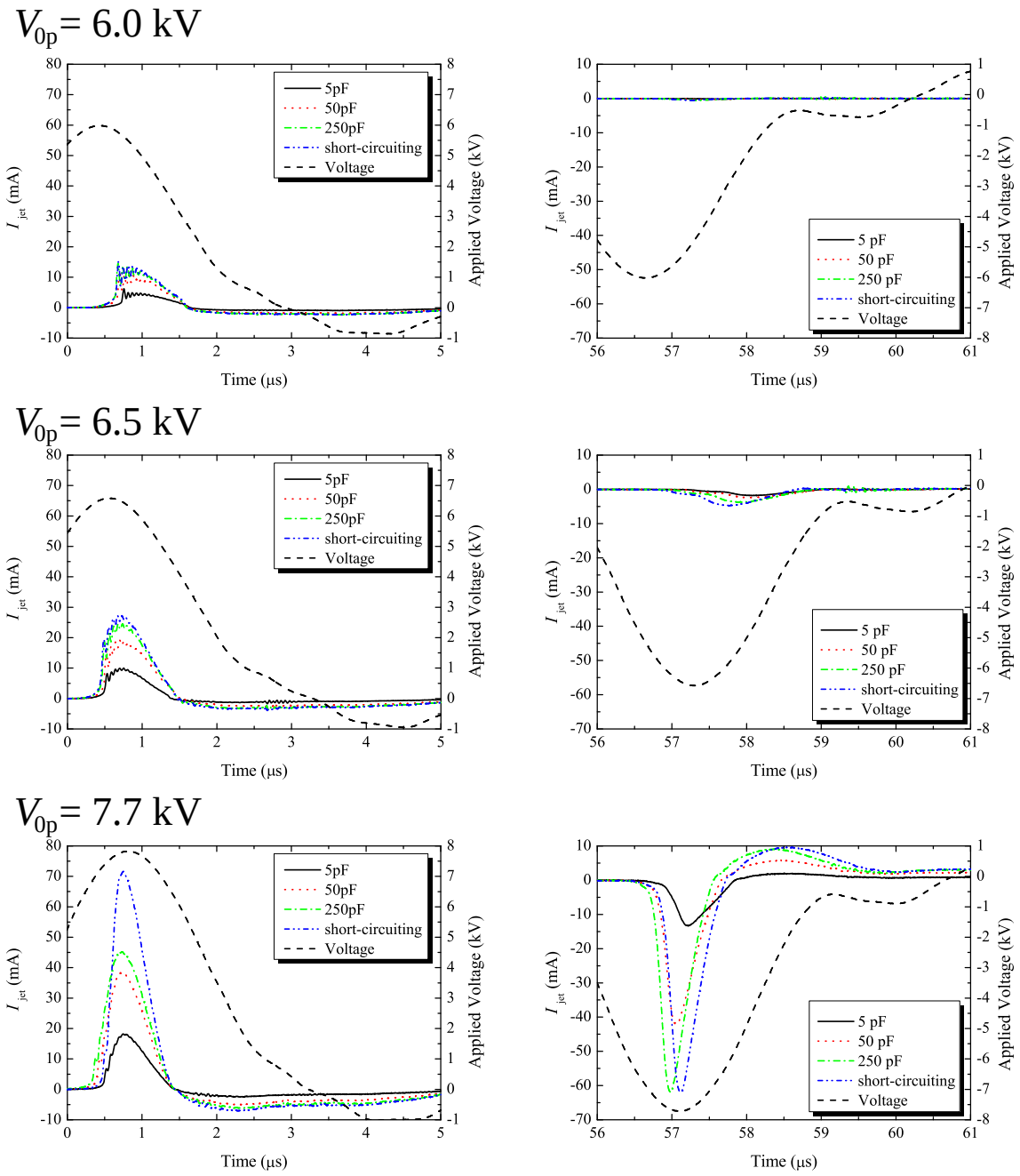

Figure 4.5 Time evolutions of discharge current I_{jet} measured at various values of capacitance C_v in the positive phase (left column) and in the negative phase (right column) of applied voltage.

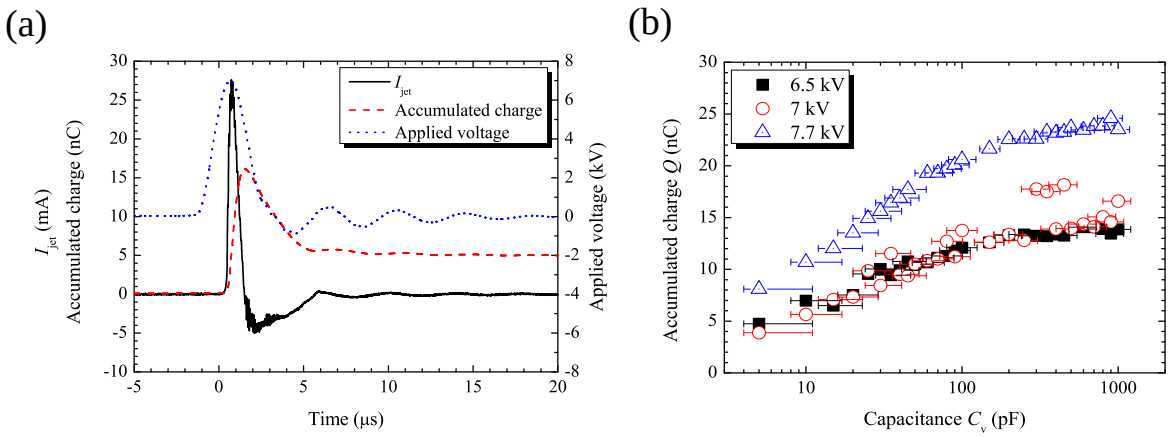

Figure 4.6 Typical waveforms of applied voltage, discharge current, and accumulated charge at C_v = 100 pF and V_{0p} = 7 kV (a), and accumulated charge Q measured as a function of capacitance C_v (b). The error bars in (b) show the effect of floating capacitance and the estimated error of ± 20% for each value of C_v.

equation (4.1). Q had a maximum value when I_{jet} became 0. Some negative current containing fluctuations with a short time period flows, possibly owing to inductance-capacitance resonance in the equivalent circuit. Additionally, in this system, since there were dielectric barrier layers, such as the glass tube and variable capacitor, the accumulated charge was discharged to the discharge space as the applied voltage decreased. This caused the negative current, i.e., self-erasing discharge, in the positive phase of the applied voltage; the phenomenon is usually observed in DBDs. Figure 4.6(b) shows the maximum value of Q plotted against the capacitance C_v. Q increased at a decreasing rate with respect to C_v up to 100 pF, above which the increase in Q slowed at all applied voltages. This leads us to conclude that the plasma disappears with the decrease in the apparent voltage between the electrodes due to the increase in Q in the low-capacitance region (C_v < 100 pF), while the plasma can survive until the decrease in the applied voltage in the high-capacitance region (C_v > 100 pF). Alternatively, the residual capacitor voltage was obtained after the discharge extinguished by dividing Q with C_v. When C_v was smaller

than 10 pF, the capacitor voltage was approximately 1 kV at all applied voltages, whereas when C_v was larger than 100 pF, the capacitor voltage was less than 100 V. In other words, the capacitance was sufficiently large in the latter case to accumulate I_{jet} without affecting the applied voltage until the plasma was extinguished.

4.3.2 Estimation of Floating Capacitance

The effect of the floating capacitance C_f was also determined by changing the capacitance C_v from 5 to 100 pF as shown in Fig. 4.3. In this situation, I_{Cu} and I_{jet} are expressed by the following equations:

$$I_{Cu}\left(t-\frac{\pi}{2}\right)=\frac{V(t)}{\omega(C_f+C_v)},\qquad I_{jet}\left(t-\frac{\pi}{2}\right)=\frac{V(t)}{\omega C_v}. \tag{4.2}$$

Here, $V(t)$ is the applied voltage and the phase shift of $\pi/2$ in the current is caused by the capacitance. The impulse part of the applied voltage was roughly approximated as $V(t) = 500\sin\omega t$ with an angular frequency of $\omega = 6.98\times10^5$ rad/s, estimated by the pulse width of the applied voltage. By using these equations, C_f was calculated to be about 5 pF. The error bars in the positive direction in Fig. 4.6(b) correspond to this floating capacitance, and error bars in both directions include the estimated error of ±20% for the value of C_v.

4.3.3 Dependence of Deposition Rate on Capacitance

Figure 4.7 shows the average deposition rate of SiO_2 during initial 15 s upon inserting glass plates between the Si substrate and the grounded metal plate as a capacitance. The capacitance was calculated from the total thickness and relative permittivity of the glass plates and the area

exposed to the plasma jet. The deposition rate increased with increasing capacitance up to 100 pF. This tendency agrees with the results obtained from the measurement of the accumulated charge shown in Fig. 4.6(b).

When the number of inserted glass plates was 12, i.e., the capacitance was 18 pF, the total thickness of the glass plates was about 1.5 mm. In this case, the distance between the plasma jet and the substrate was less than that in the case without the capacitance. Therefore, the electric field was expected to be enhanced at least by 8% at the capacitance of 18 pF. However, the deposition rate was lower than that without the capacitance. This suggests that the electric field (or the gap voltage) is reduced by the accumulated charge on the surface, which suppresses the current I_{jet} at a smaller value of C_v than about 100 pF. In contrast, with increasing C_v the deposition rate asymptotically approaches the ultimate value without the capacitance. This

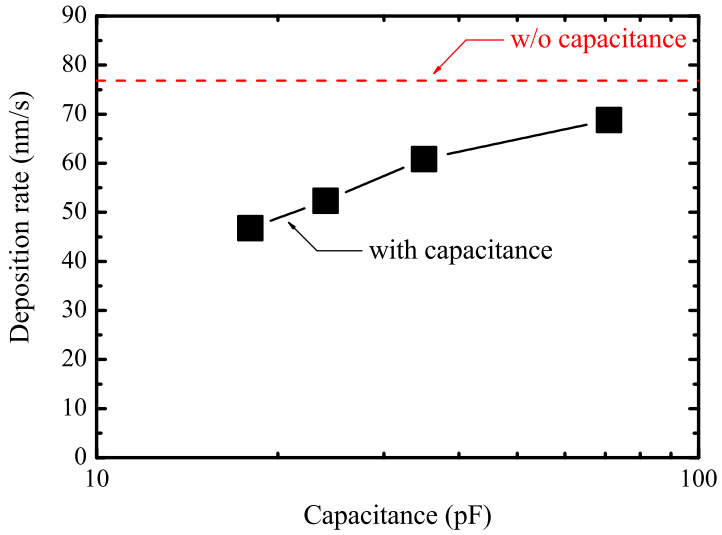

Figure 4.7 Measured deposition rate of SiO_2 films versus inserted capacitance during initial 15 s. The dashed line shows the deposition rate without the capacitance C_v.

observation demonstrates that the accumulated charge produces no noticeable voltage on the variable capacitor to reduce the gap voltage.

4.4 Discussion

To consider the effect of the accumulated charge, it is assumed that the system is expressed by a simple equivalent circuit as shown in Fig. 4.8. The capacitance of the glass tube C_g is roughly estimated to be 4 pF from the relative permittivity of the glass, the thickness of the glass tube of 1.5 mm, and the area of the tubular electrode. Moreover, the plasma is represented by a resistance R because I_{jet} was measured as the conductive current by subtracting the displacement current. Additionally, the switch is turned on after the streamer head of the positive corona discharge reaches the copper plate at time $t = 0$. Assuming this equivalent circuit, we can

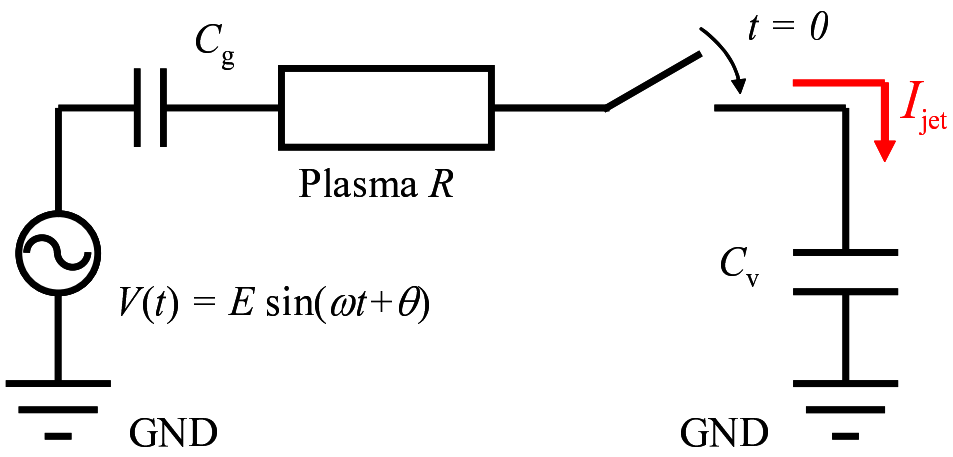

Figure 4.8 Equivalent circuit of plasma jet and substrate with capacitance. The switch is turned on at $t = 0$ when the streamer of the APPJ reaches the copper plate.

obtain the following equation:

$$R\frac{dQ(t)}{dt} + \frac{Q(t)}{C_{\mathrm{T}}} = E\sin(\omega t + \theta), \quad \frac{1}{C_{\mathrm{T}}} = \frac{1}{C_{\mathrm{g}}} + \frac{1}{C_{\mathrm{v}}}. \tag{4.3}$$

Here, $Q(t)$ is the accumulated charge on the variable capacitor and the glass tube, and the waveform of the positive-impulse part of the applied voltage corresponds to a half cycle of a sine wave. And, θ is the initial phase when the discharge takes place. By solving this equation, assuming the initial charge $Q(0) = 0$, we obtain the discharge current I_{jet} as follows:

$$I_{\mathrm{jet}}(t) = \frac{E\left[\cos(\omega t + \theta - \varphi) + \dfrac{\sin(\theta - \varphi)}{\omega C_{\mathrm{T}} R}\exp\left(-\dfrac{t}{C_{\mathrm{T}} R}\right)\right]}{\sqrt{R^2 + \left(\frac{1}{\omega C_{\mathrm{T}}}\right)^2}}, \quad \varphi = \arctan(\omega C_{\mathrm{T}} R). \tag{4.4}$$

By comparing the relaxation times of I_{jet} obtained by measurement and by calculation without C_{v} and with $C_{\mathrm{g}} = 4$ pF, R was estimated to be 6.0×10^4 and 8.3×10^4 Ω when $V_{0\mathrm{p}}$ was 7.7 and 6.5 kV, respectively. On the other hand, R is given by the following expression:

$$R = \rho(E/p)\frac{L}{S} = \frac{1}{e\mu(E/p)\, n_{\mathrm{e}}(E/p)}\frac{L}{S}. \tag{4.5}$$

Here, ρ is the resistivity of the plasma, L and S are the length and cross-sectional area of the plasma, respectively, e is the elementary charge, μ is the mobility of electrons, and n_{e} is the electron density in the plasma. In accordance with the experimental conditions, L was taken as 2 cm, and the diameter of the plasma was assumed to be 2 mm from the visual observation. μ was estimated as a function of the electric field by the Boltzmann code BOLSIG [4.15]. Upon the assumption of a homogeneous electron density in the plasma, the maximum electron density

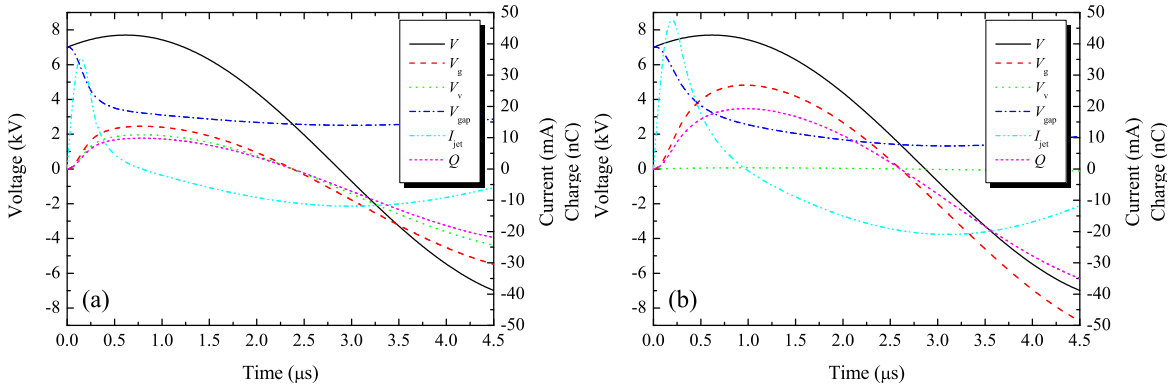

Figure 4.9 Calculated results of time evolution of discharge current I_{jet}, accumulated charge Q, induced voltages V_g and V_v, and gap voltage V_{gap} at two values of C_v (5 pF (a) and 300 pF(b)) with a fixed V_{0p} of 7.7 kV.

at the time when I_{jet} was greatest was estimated to be 7.3×10^{12} and 5.3×10^{12} cm^{-3} when V_{0p} was 7.7 and 6.5 kV, respectively. These values agreed well with the reported data of Lu and Laroussi [4.16] and Sakai *et al* [4.17]. Regarding the data of Ref. 17, the measured density of helium metastable atoms is almost the same as that in the present case [4.7, 18]. Therefore, the agreement of the electron density may be reasonable, considering that in the afterglow the majority of electrons are produced by the Penning ionization process of helium metastable atoms with nitrogen molecules in the ambient air.

In order to calculate I_{jet}, it was assumed that the electron density increases linearly from zero to the maximum value at the time when the experimental I_{jet} reaches its peak value. Figure 4.9 shows the calculated results of the discharge current I_{jet}, the accumulated charge Q, the induced voltages V_g and V_v on C_g and C_v, respectively, and the gap voltage (across R), $V_{gap} = V - V_g - V_v$ at two values of C_v (5 and 300 pF) with a fixed V_{0p} of 7.7 kV. It is seen that the peak value of I_{jet} increases with increasing C_v owing to the second term of equation (4.4). The calculated waveforms of I_{jet} accurately depict the features of the experimental data shown in Fig. 4.5. In the case of small C_v (= 5 pF), Q accumulates faster and V_v reduces V_{gap} rapidly, so that

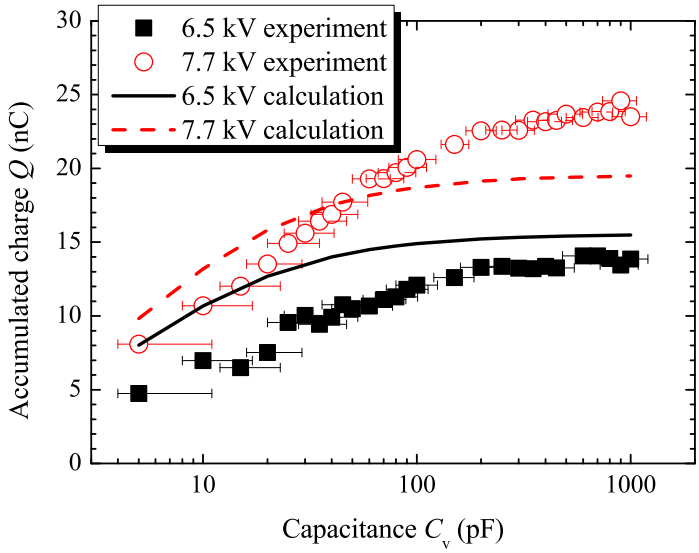

Figure 4.10 Calculated results of accumulated charge as a function of capacitance C_v in comparison with measured results at V_{0p} of 6.5 and 7.7 kV.

I_{jet} decreases faster with a smaller peak. However, owing to the smaller current, it takes a considerable time to charge C_g and C_v. On the other hand, at a large C_v (= 300 pF), the effect of V_v cannot be seen, even though I_{jet} is larger; thus, V_{gap} decreases more slowly with a larger current tail. The decrease in the applied voltage accelerates the decrease in V_{gap}, causing the current to decrease to zero. Afterwards, a reverse (negative) current flows owing to the decrease in the applied voltage. This current erases the accumulated charge.

The calculated results obtained by combining equations (4.1) and (4.4) are shown in Fig. 4.10. From this figure, it can be seen that the calculated results are in close agreement with the experimental data presented in section 4.3. The difference between the experimental data and the calculated results may be due to the spread of the accumulated charge on the glass tube surface and on the substrate surface in the experiment, causing the increase in the capacitance. Comparing the cases of V_{0p} = 6.5 and 7.7 kV, this effect becomes greater as V_{0p} increases. Actually, the gap voltage, estimated from $V_{gap} = V - Q/C_g - Q/C_v$ using the measured Q, becomes negative owing to the underestimation of these capacitances. Additionally, we assumed

that R was constant even during the afterglow period. This caused the calculated results of the accumulated charge to be larger than the experimental results.

From Figs. 4.7 and 4.10, it can be concluded that the deposition rate of SiO_2 is correlated with the accumulated charge on the surface. This shows that the deposition rate is governed by the peak value of I_{jet} because the duration of I_{jet} was almost the same at all C_v in the range from 5 to 1000 pF as seen in Fig. 4.5. The discharge current is related to the densities of electrons and excited species, which cause the decomposition of source molecules and the formation of film precursors to be shown in Chapter 5.

If the capacitance of the glass tube wall is increased by replacing it with a material of higher relative permittivity, by increasing the area of the electrode, or by decreasing the thickness of the capillary, the effect of the accumulated charge on the substrate can be reduced, which may lead to the enhancement of the deposition rate of metal oxide films.

4.5 Summary

The effect of accumulated charge on a substrate surface has been investigated by measuring the discharge current. By comparing results obtained by measurement and using on equivalent model of the plasma jet system, it has been clarified that the accumulated charge on the substrate strongly affected the deposition rate when the capacitance was less than 100 pF. Moreover, the capacitance of the glass capillary also affected the timing of the discharge current. Furthermore, the effect of the accumulation of charge was ascertained through the measurement of the deposition of SiO_2 on a Si substrate, and the results were consistent with the fact that the discharge current, which is determined by the capacitance, governs the deposition rate.

References

[4.1] K. Tachibana: IEEJ Trans. Electr. Electron. Eng. **1**, 145 (2006).

[4.2] O. Sakai, K. Tachibana, K. Tatsugawa, K. Ohishi and R. Inoue: Trans. Mater. Res. Soc. Jpn. **31**, 453 (2006).

[4.3] K. Takaki, Y. Hatanaka, K. Arima, S. Mukaigawa and T. Fujiwara: Vacuum **83**, 128 (2008).

[4.4] Z. Cao, J. L. Walsh and M. G. Kong: Appl. Phys. Lett. **94**, 021501 (2009).

[4.5] H. Bhuyan, M. Favre, E. Valderrama, G. Avaria, E. Wyndham, H. Chuaqui, J. Baier, H. Kelly, D. Grondona and A. Marquez: Appl. Surf. Sci. **255**, 3558 (2009).

[4.6] T. Ideno and T. Ichiki: Thin Solid Films **506-507**, 235 (2006).

[4.7] Y. Ito, K. Urabe, M. Kubo and K. Tachibana: *Proc. 18th Int. Symp. Plasma Chem.* 28P-65 (Kyoto, 2007).

[4.8] M. Čada, P. Virostko, Š. Kment and Z. Hubička: Vacuum **83**, 738 (2009).

[4.9] M. Teschke, J. Kedzierski, E. G. Finantu-Dinu, D. Korzec and J. Engemann: IEEE Trans. Plasma Sci. **33**, 310 (2005).

[4.10] K. Kitano and S. Hamaguchi: *Proc. 18th Int. Symp. Plasma Chem.* 27A-a5 (Kyoto, 2007).

[4.11] K. Urabe, Y. Ito, K. Tachibana and B. N. Ganguly: Appl. Phys. Express **1**, 066004 (2008).

[4.12] H. Furusho, K. Kitano, S. Hamaguchi and Y. Nagasaki: Chem. Mater. **21**, 3526 (2009).

[4.13] Y. Ito, K. Urabe, N. Takano and K. Tachibana: Appl. Phys. Express **1**, 067009 (2008).

[4.14] T. Somekawa, T. Shirafuji, O. Sakai, K. Tachibana and K. Matsunaga: J. Phys. D: Appl.

Phys. **38**, 1910 (2005).

[4.15] G. J. M. Hagelaar and L. C. Pitchford: Plasma Sources Sci. Technol. **14**, 722 (2005).

[4.16] X. P. Lu and M. Laroussi: Appl. Phys. Lett. **92**, 051501 (2008).

[4.17] O. Sakai, T. Sakaguchi, Y. Ito and K. Tachibana: Plasma Phys. Control. Fusion **47**, B617 (2005).

[4.18] K. Tachibana, Y. Kishimoto and O. Sakai: J. Appl. Phys. **97**, 123301 (2005).

Chapter 5

Deposition and Analysis of SiO_2 Films[†]

5.1 Introduction

Non-thermal plasma jets at atmospheric pressure have received considerable attention in recent years for their potential applications to various material processes such as surface modification [5.1–3], dry etching [5.4, 5], and plasma enhanced chemical vapor deposition (PE-CVD) [5.6, 7]. These plasma jets can generate active species for the processes but have a range of gas temperatures low enough not to damage the substrate materials. However, only a few groups have reported on material depositions with the glow-like plasma jets, taking care of relatively high frequency discharge and high gas flow rate not only to spout a plasma plume but also to restrain the increase in gas temperature and prevent the transition to arc discharges [5.6–8].

The aim of this study is to develop a method of high-speed deposition of SiO_2 films, which are widely used as insulators in electronic devices, onto a narrow (one-dimensional) substrate like a flattened glass fiber. To achieve this purpose, the deposition from $Si(OC_2H_5)_4$ (tetraethoxysilane : TEOS), shown in Fig. 5.1, has been carried out using an atmospheric-pressure plasma jet (APPJ) based on coaxial dielectric barrier discharge operated in a glass tube with helium gas flow [5.9]. By using TEOS, good step coverage of SiO_2 films is obtained because TEOS has

[†]This Chapter, in slightly altered form, is published in: Y. Ito, K. Urabe, N. Takano and K. Tachibana, "High Speed Deposition of SiO_2 Films with Plasma Jet Based on Capillary Dielectric Barrier Discharge at Atmospheric Pressure", Applied Physics Express **1**, 67009 (2008).

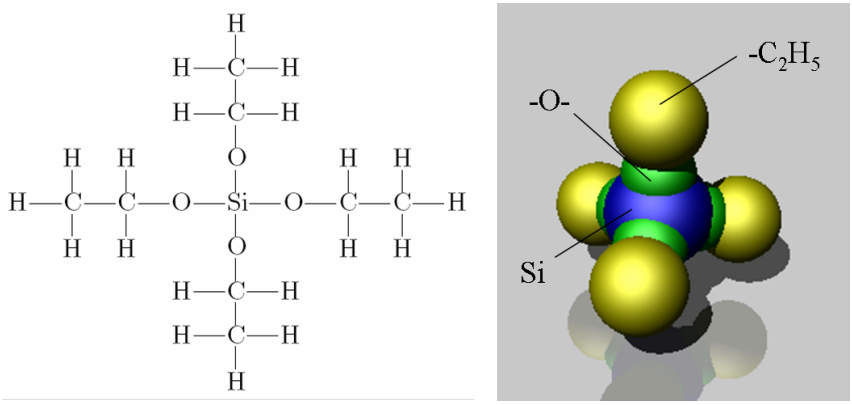

Figure 5.1 Chemical structure of TEOS.

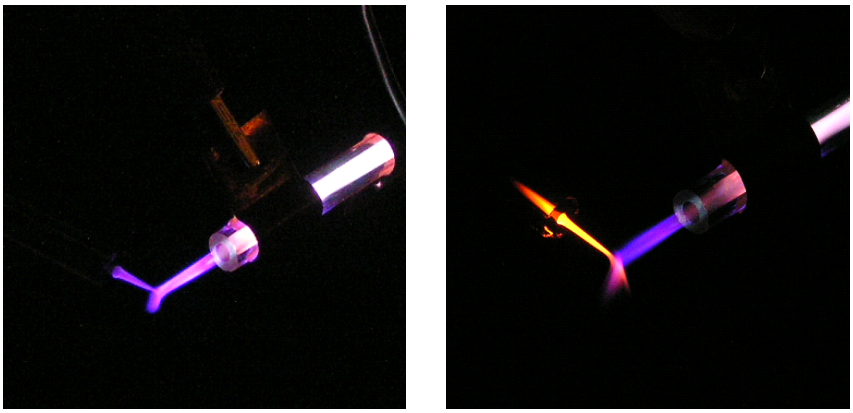

Figure 5.2 Photographs of cross jets, which consist of the APPJ based on coaxial dielectric barrier discharge with an additional helium flow (a) and neon flow (b).

low reactive sticking probability [5.10].

This type of a simple plasma jet driven at kHz order with atmospheric pressure of helium has been developed and analyzed by Engemann *et al.* [5.11] to have a long plume composed of “plasma bullets” effused into the ambient air, shown in Chapter 2. The behavior of the plasma bullets have been further analyzed by laser induced fluorescence spectroscopy and it was revealed that the temperature of the plasma jet stays near room temperature and the apparent fast-movement of the bullet is due to the ionization wave similar to a streamer in positive corona discharge by the previous work [5.12]. The plasma jet is prolonged toward the axial direction of

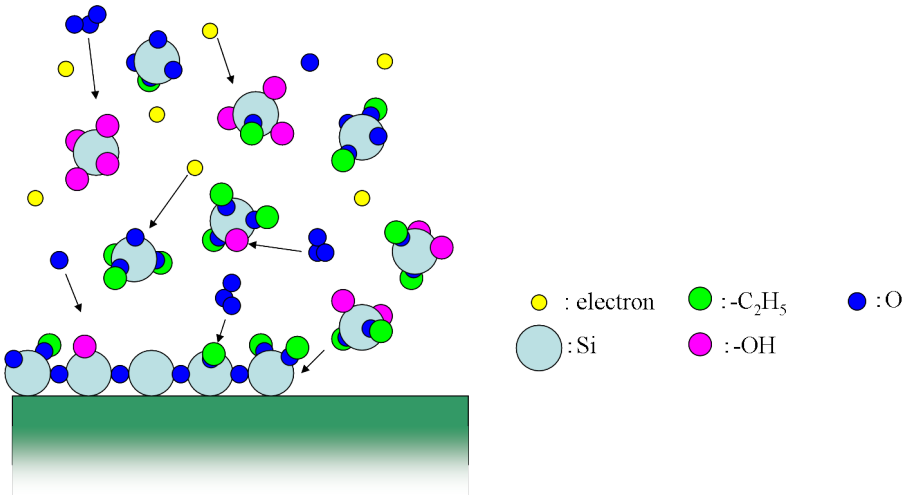

Figure 5.3 Schematic of reactions of TEOS in the plasma.

the capillary along the electric field in the helium stream, in which the discharge at the ionization wave front can take place more easily than in the surrounding air.

K. Kitano reported that, in a crossed configuration of the plasma jet with another helium gas flow, the plasma jet can ignite the discharge in the gas flow to form another jet [5.13]. The behavior have been ascertained and it was found that it can occur in neon gas flow too, as shown in Fig. 5.2. With a hint from this effect, an idea to apply the crossed beam configuration of a plasma jet with another gas flow to the PE-CVD of thin films has been given rise to. In the crossed configuration, the source material, in this case TEOS, can be separately supplied through the other nozzle crossed with the plasma jet, expecting its activation at the crossed point near or on the substrate. TEOS can be dissociated by electrons and ions in the plasma as well as O atoms, and O_3 molecules [5.14], which are sourced from ambient air, and forms SiO_2 on the substrate. The schematic draw of the reactions of TEOS with active species in the plasma is shown in Fig. 5.3 and the reactions are listed in Table 5.1. The bond energies of C-O and Si-O bands are 3.7 and 4.7 eV, respectively. Therefore these reactions easily take place.

Table 5.1 Reactions of precursors in gas phase and on surface [5.14].

Gas phase
$Si(OC_2H_5)_n(OH)_{4-n} + e \rightarrow Si(OC_2H_5)_{n-1}(OH)_{4-n+1} + C_2H_4 + e$
$Si(OC_2H_5)_n(OH)_{4-n} + O \rightarrow Si(OC_2H_5)_{n-1}(OH)_{4-n+1} + CH_3CHO$
$Si(OC_2H_5)_n(OH)_{4-n} + O_3 \rightarrow Si(OC_2H_5)_{n-1}(OH)_{4-n+1} + CH_3CHO + O_2$
n = 1 - 4
Surface
$Si(OC_2H_5)_3OH + 18O \rightarrow SiO_2 + 6CO_2 + 8H_2O$
$Si(OC_2H_5)_3OH + 18O_3 \rightarrow SiO_2 + 6CO_2 + 8H_2O + 18O_2$
$Si(OC_2H_5)_2(OH)_2 + 12O \rightarrow SiO_2 + 4CO_2 + 6H_2O$
$Si(OC_2H_5)_2(OH)_2 + 12O_3 \rightarrow SiO_2 + 4CO_2 + 6H_2O + 12O_2$
etc ...

5.2 Experimental Procedure

Figure 5.4 shows a schematic diagram and an appearance of the PE-CVD system (PD-0-1, Japan Pionics Co., Ltd.) used in this experiment. Liquid TEOS (0.1 g/min) was pumped to the vaporizer, in which it was vaporized, and carried by helium (at less than 3 SLM) through a stainless pipe heated at 170℃ because the boiling temperature of TEOS is around 170℃. The plasma jet configurations for this PE-CVD system are illustrated in Fig. 5.5 together with a coaxial configuration of TEOS supply, shown in Fig. 5.5(a), for a comparative study. Two different setups were tried in the crossed configuration; one was the vertical plasma jet crossed with the tilted TEOS supply nozzle at 45°, shown in Fig. 5.5(b), and the other was the tilted plasma jet with the vertical TEOS supply nozzle, shown in Fig. 5.5(c). The plasma jet shown in Figs. 5.5(a) and (b) consisted of a glass tube of 4-mm inner diameter, equipped coaxially with a stainless steel tube of 3-mm outer diameter, of which the exit region was pinched to 3-mm inner diameter to form the plasma jet with a tubular copper electrode of 10-mm length wound on the glass tube. In the configuration of Fig. 5.5(c) a simple glass tube of 3-mm inner diameter was used for the plasma jet. TEOS was supplied coaxially through a stainless tube in

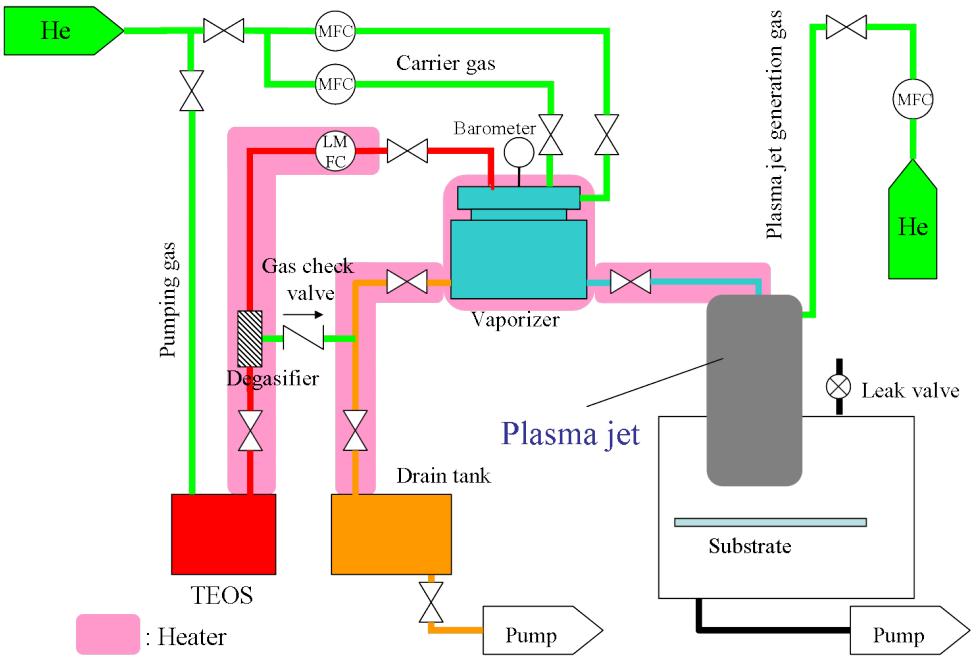

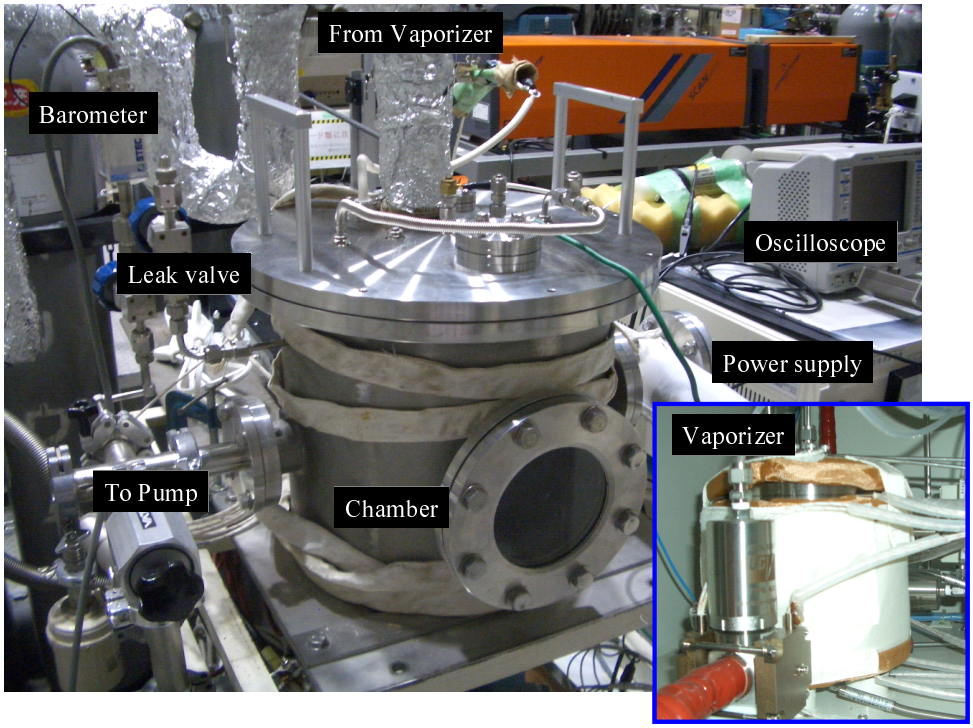

Figure 5.4 Schematic diagram (upper) and Appearance (lower) of PE-CVD system.

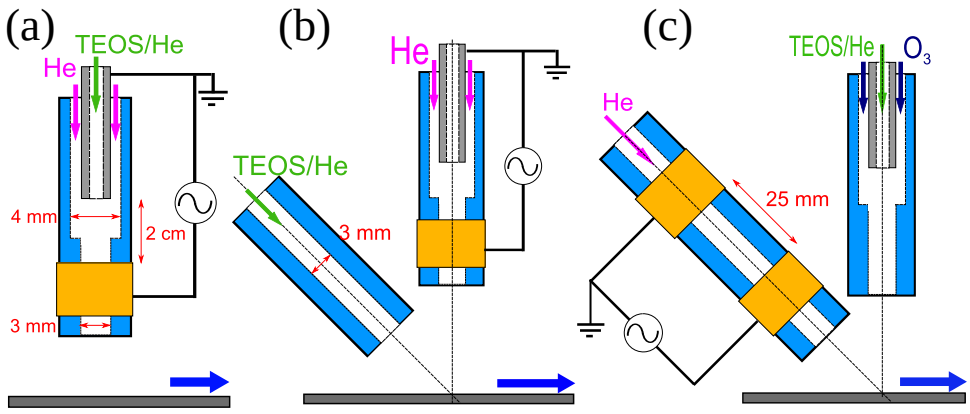

Figure 5.5 Schematics of the plasma enhanced chemical vapor deposition system: coaxial configuration (a), crossed configuration with vertical plasma jet and tilted TEOS supply (b), and crossed configuration with tilted plasma jet and vertical TEOS supply (c). Arrows show the direction of substrate scanning.

the configuration of Fig. 5.5(a), while it was supplied separately in the crossed configurations as shown in Figs. 5.5(b) and (c). The plasma jet was generated using a bipolar impulse power supply at frequency range of 2.5 to 30 kHz [5.15]. The length of the plasma plume effused into ambient air was adjustable from 10 to 70 mm according to the applied peak voltage V_{0p} and the gas flow rate Q as shown in Chapter 2. At a typical set of values of V_{0p} = 6 kV and Q = 2 SLM (standard litter per minute) used in the present experiments, the plasma plume was about 50 mm in free space. Here, the Reynolds number of helium gas flow in both the plasma jet and the TEOS supply was around 300, so that it was in the range of laminar flow. The linear deposition was carried out on a silicon substrate held on a stage heated up to 140℃ with the movement of the stage at a constant speed of 1 or 4 cm/min. Figure 5.6 shows the photographs of the coaxial configuration in (a)-(c), and the tilted jet configuration in (d). By comparing Figs. 5.6(b) and (c), it is seen that the color of the plasmas changed whether with or without TEOS, and the shape of the plasmas in the glass tube with TEOS was thinner than that without TEOS.

In both types of the crossed configuration, the direction of the movement of the stage and two

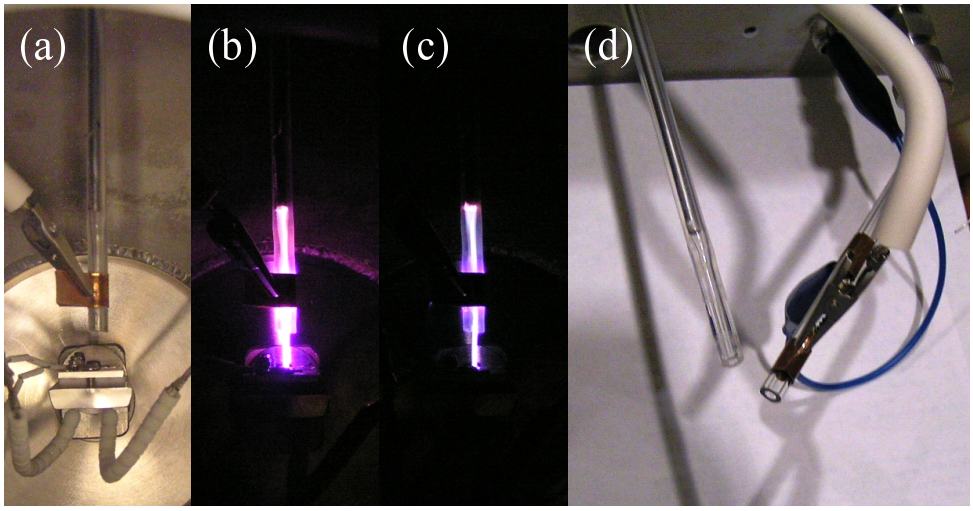

Figure 5.6 Photographs of coaxial configuration and tilted jet configuration; (a) shows the appearance of the coaxial configuration, (b) shows the photograph of the plasma jet with the coaxial configuration, and (c) is that with TEOS. (d) is appearance of the tilted jet configuration.

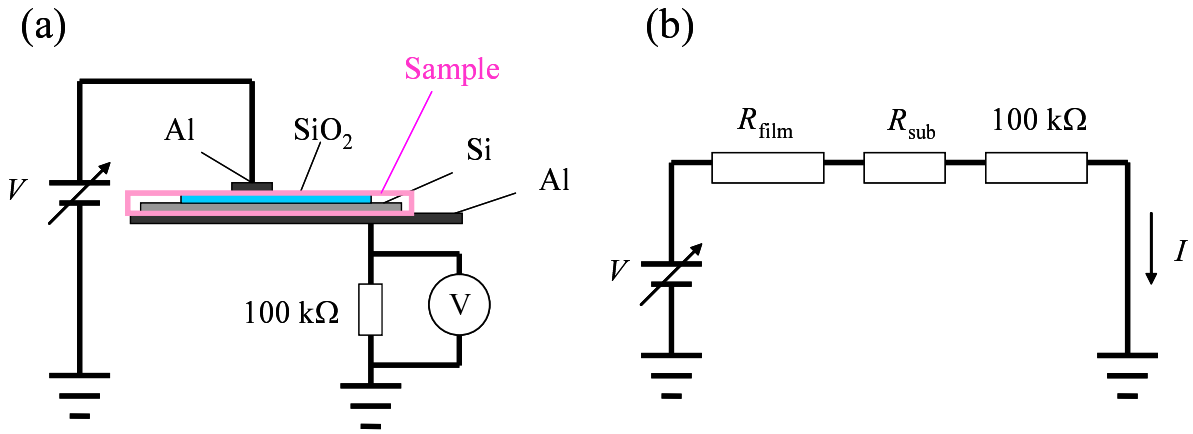

Figure 5.7 Schematics of beakdown test of deposited films: Experimental setup (a) and equivalent circuit (b). Resistance of the deposited films R_{film} is much higher than that of the substrate R_{sub}.

glass tubes were arranged in the same plane as shown in Fig. 5.5. Because it has been known that O_3 molecules play an important role in the formation of SiO_2 films [5.14, 16], O_3 was generated by a home built ozonizer system and was supplied into the vertical glass tube through the annular space between the glass tube and the stainless steel tube in the configuration of Fig. 5.5(c). Here, the density of O_3 molecules in the source gas flow was estimated from the

generation rate to be on the order of 10^{16} cm^{-3}.

Figure 5.7 shows the schematic draws of the breakdown test of deposited films. The aluminum electrode was evaporated on the top of the deposited films and was connected to a constant-voltage source. The Si substrate was connected to a resistor of 100 kΩ and the value of current was estimated by measuring the voltage applied to the resistor. In this setup, the resistance of the deposited films R_{film} is much higher than that of the substrate R_{sub}, i.e., almost all the voltage is applied to the deposited films.

5.3 Experimental Results

5.3.1 High-Speed Deposition of SiO_2 Films

Figure 5.8 shows the appearance of the deposited film on a Si substrate. The deposited films had cross-sectional profiles nearly expressed by a Gaussian shape, and the maximum height varied depending on the deposition conditions from several hundreds to thousands nm with a

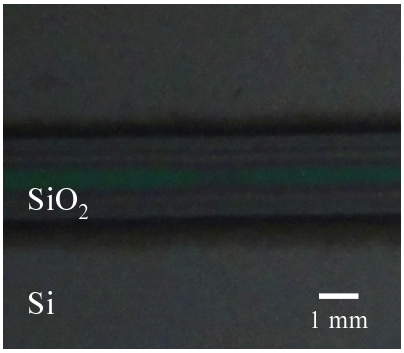

Figure 5.8 Appearance of deposited film.

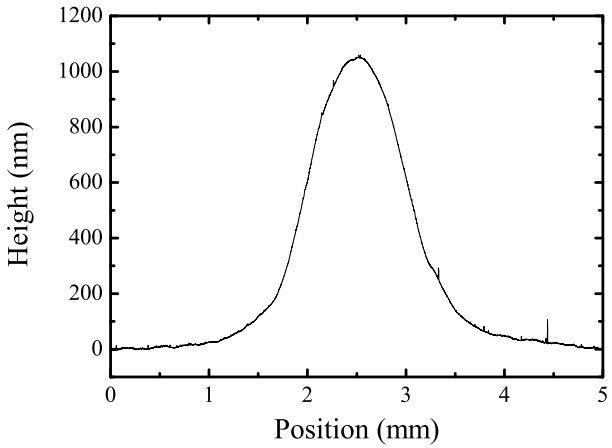

Figure 5.9 Typical cross-sectional profile of deposited film at a scanning speed of the substrate of 4 cm/min and a driving frequency of 30 kHz.

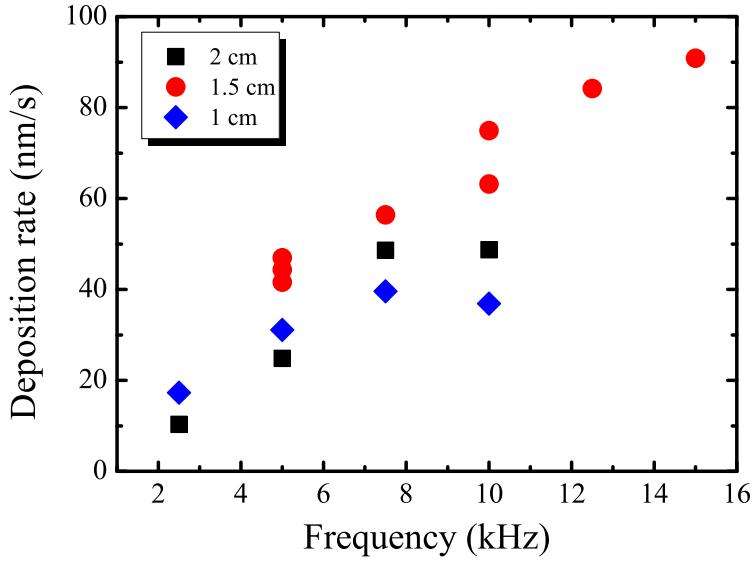

Figure 5.10 Deposition rate of SiO_2 films with coaxial supply configuration, dependent on the distance between the jet exit and the substrate at a scanning speed of substrate of 1 cm/min, as a function of driving frequency.

full width at half maximum (FWHM) of about 1 mm, shown in Fig. 5.9. The deposition rate was determined from the maximum height by multiplying with the scan speed and dividing with the diameter of the plasma jet which was assumed to be equal to the FWHM of the deposited film profile.

As shown in Fig. 5.10, the deposition rate of SiO_2 films with coaxial supply configuration increases with an increase in the driving frequency in a range from 2.5 to 15 kHz. It appears that the deposition rate for the coaxial supply configuration is not so much sensitive to the distance between the jet exit and the substrate. But the FWHM of the deposited film thickness increases with a decrease in the substrate distance due to the change in the diameter of the plasma plume. The maximum deposition rate of SiO_2 film in this configuration was about 90 nm/s at a frequency of 15 kHz and at a distance of 1.5 cm.

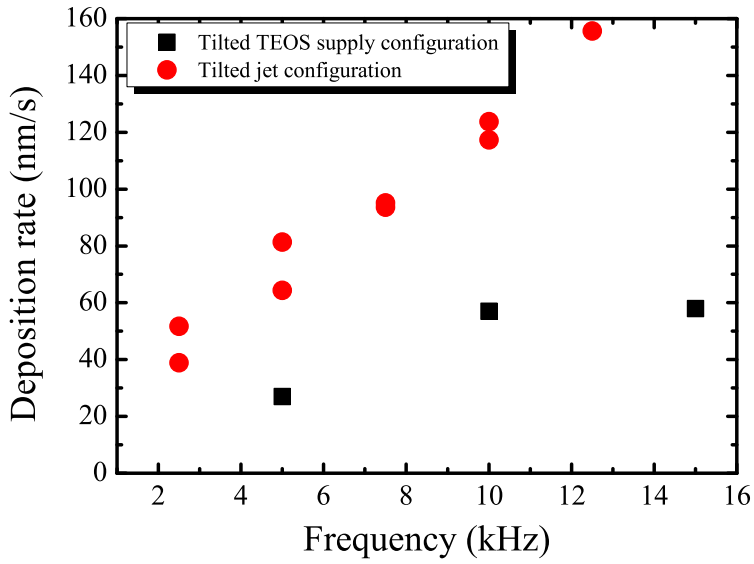

Figure 5.11 Deposition rate of SiO_2 films with tilted TEOS supply configuration with the distance between the jet exit and substrate of 1.5 cm, and tilted jet configuration with the distance of 1 cm at a scanning speed of substrate of 1 cm/min as a function of driving frequency.

Figure 5.11 shows the deposition rate of SiO_2 films versus the driving frequency with the tilted TEOS supply configuration and the tilted jet one corresponding to Figs. 5.5(b) and 5.5(c), respectively. In both cases, the deposition rate increases monotonically with the driving frequency as in the case of the coaxial configuration. From Figs. 5.10 and 5.11, it is seen that the deposition rate for the tilted TEOS configuration is the lowest and that for the tilted jet one is the highest. This is probably due to the difference in the density of precursors transported or generated at the substrate surface. In the coaxial configuration, TEOS flows through inter-electrode plasma region, with higher electron density, where TEOS molecules are decomposed largely. However, in the transport to the substrate, the precursors may be coagulated partially to form clusters or powders and blown out of the deposition region. This assumption is discussed in Section 5.4. On the other hand, in the case of tilted jet or tilted TEOS supply configuration,

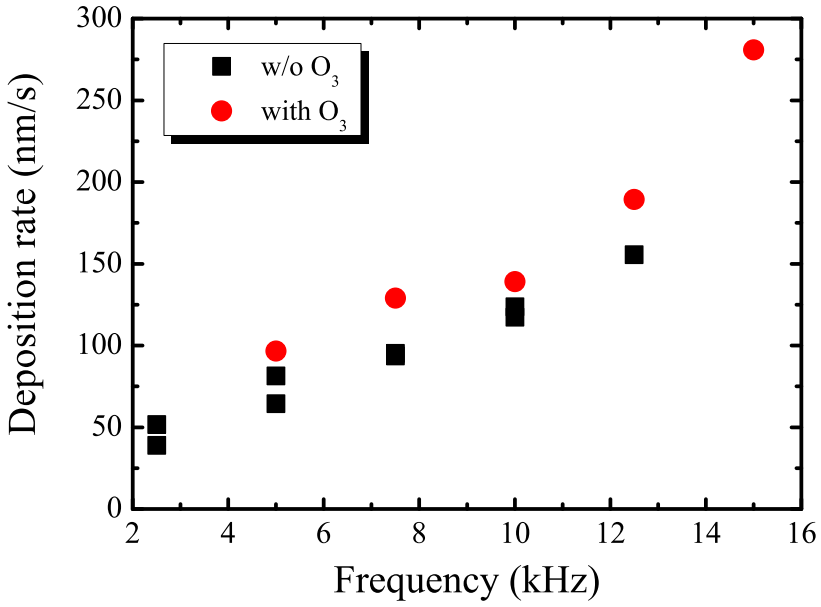

Figure 5.12 Deposition rate of SiO_2 films with tilted jet configuration with and without O_3 at a scanning speed of substrate of 1 cm/min as a function of driving frequency.

the plasma jet activates the separately transported TEOS molecules to proceed the SiO_2 deposition on the substrate. The much higher deposition rate observed with the tilted jet configuration may be attributed to the longer interaction distance due to the plasma spread along the substrate surface. A value of 150 nm/s in Fig. 5.11 realized at a frequency of 12.5 kHz is more than 10 times as high as that reported in conventional methods at low pressure.

Figure 5.12 shows the deposition rate in the tilted jet configuration with and without O_3 supply. In the case of O_3 addition, the deposition rate is larger than that without O_3 at any frequency in the range from 5 to 12.5 kHz by about 10 to 20%. This fact indicates that O_3 molecules contribute to the production of precursors from TEOS. In this case, the maximum deposition rate of about 280 nm/s was obtained at a frequency of 15 kHz.

Figure 5.13 shows the deposition rate with the tilted jet configuration with O_3 supply at a

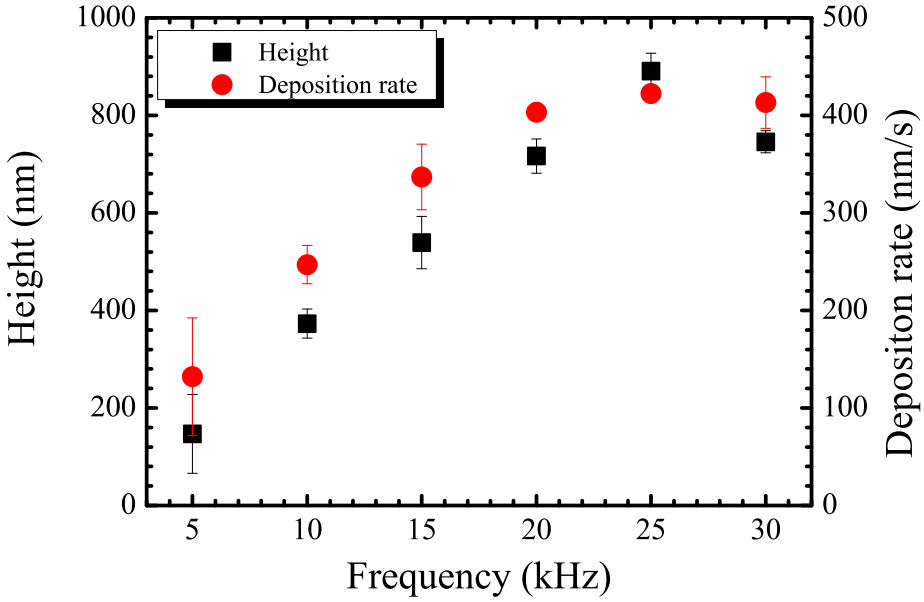

Figure 5.13 Deposition rate of SiO_2 films with tilted jet configuration with O_3 at a scanning speed of substrate of 4 cm/min as a function of driving frequency.

scanning speed of the substrate of 4 cm/min. The deposition rate of SiO_2 films increased with an increase in the driving frequency in the range from 5 to 30 kHz. Comparing with Fig. 5.12, the deposition rate was strongly enhanced, and the maximum deposition rate of about 400 nm/s was obtained at a frequency of around 30 kHz. This is due to the shortening of the duration of deposition time. As identified in Chapter 4, the long deposition time, i.e., the low capacitance on the substrate leads to the low deposition rate by the effect of accumulated charge on the substrate. Therefore, as increasing the driving frequency, i.e., the thickness of the films become larger, the rate of increase in deposition rate decreases. Thus, for a certain speed of the substrate, there is an optimal driving frequency.

In a comparison, there is a reported result on the SiO_2 deposition rate of 5 nm/s obtained by an RF-driven plasma jet with TEOS source [5.6]. This very low value might be due to the

small TEOS supply given by the admixed pressure up to 1 Pa. In a different situation with a microplasma integrated system, our group have ever tried the deposition at atmospheric pressure and obtained a typical rate of 4 nm/s over a larger area [5.17]. The data in this experiment are extremely larger than those previous results.

5.3.2 Analysis of SiO_2 Films

Figure 5.14 shows the spectrum of X-ray photoelectron spectroscopy (XPS) of a deposited film prepared by the coaxial configuration at a driving frequency of 5 kHz. The concentration of carbon was 1.55 mole %. Therefore, the deposited film contained little carbon fraction. And, since the ratio of Si and O was near 1 to 2, the deposited film was thought of as SiO_2 film.

Figure 5.15(a) shows the cross-sectional view of the deposited film prepared by the tilted jet configuration at a driving frequency of 30 kHz and the scanning speed of the substrate of 4 cm/min. From this SEM image, it was found that SiO_2 was smoothly deposited on a Si substrate

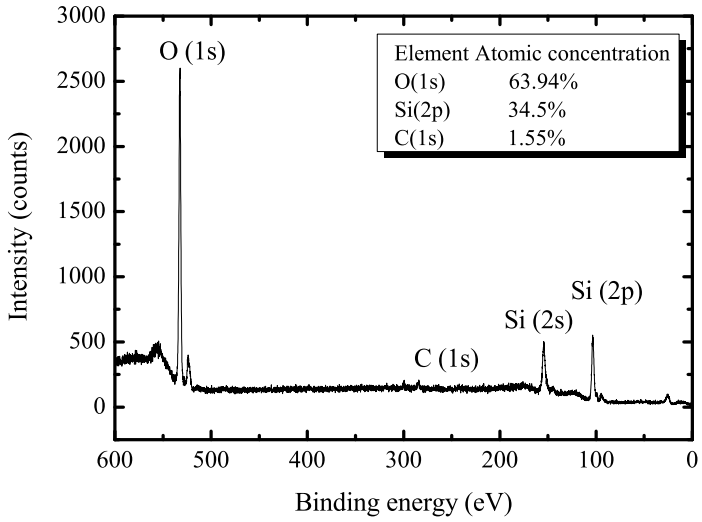

Figure 5.14 XPS spectrum of deposited film prepared with coaxial configuration at driving frequency of 5 kHz.

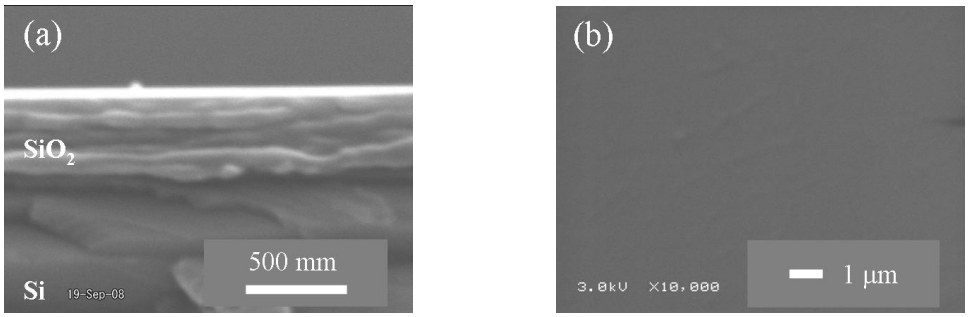

Figure 5.15 SEM images of deposited film prepared with tilted jet configuration at driving frequency of 30 kHz and scanning speed of substrate of 4 cm/min: Cross-sectional view (a) and surface (b).

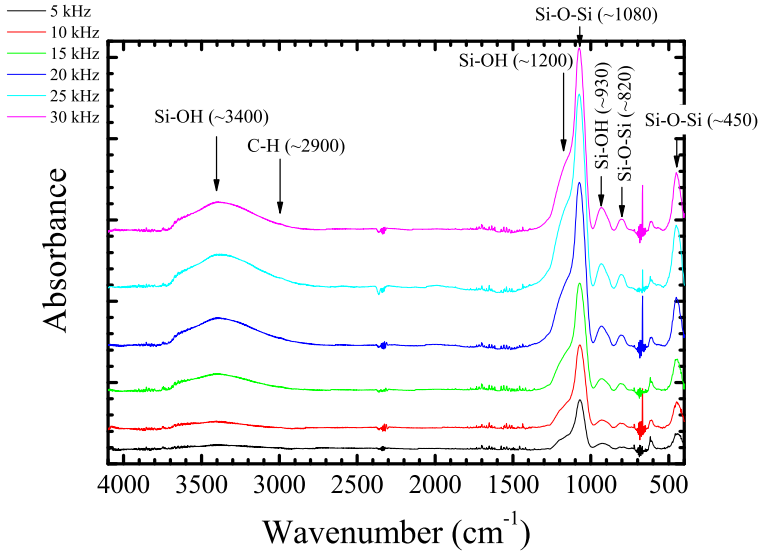

Figure 5.16 FTIR spectra of deposited films prepared with tilted jet configuration at scanning speed of substrate of 4 cm/min.

and the thickness of the deposited film was about 400 nm. Additionally, there were few cracks, dusts, and clusters on smooth surface as shown in Fig. 5.15(b). At every driving frequency, the deposited films were almost the same surface condition.

Figure 5.16 shows the spectra of Fourier transform infrared spectroscopy (FTIR) of the deposited films prepared by the tilted jet configuration at a scanning speed of the substrate of 4 cm/min. At every driving frequency, there were some peaks of Si-OH and Si-O-Si bands, and

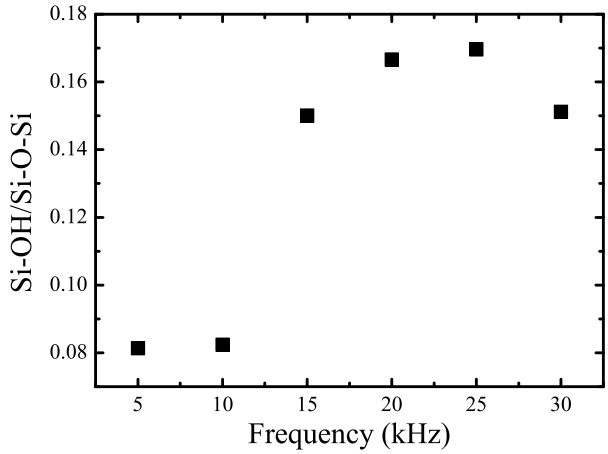

Figure 5.17 Ratio of peaks of Si-OH band (~3400 cm^{-1}) to Si-O-Si band (~1080 cm^{-1}) as a function of driving frequency.

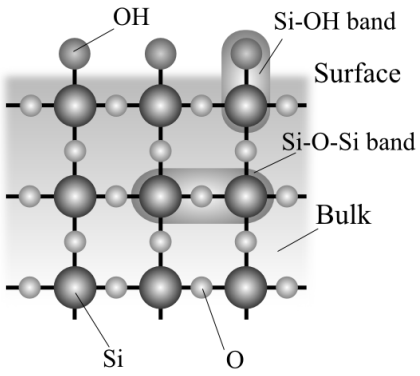

Figure 5.18 Schematic of SiO_2 at the bulk region and at the surface.

every spectra had almost the same waveform. Although there was a small peak of C-H band (~2900 cm^{-1}), almost pure SiO_2 films were obtained by the tilted jet configuration. Figure 5.17 shows the ratio of the peaks of Si-OH band (~3400 cm^{-1}) to Si-O-Si band (~1080 cm^{-1}) as a function of the driving frequency. The ratio of Si-OH band to Si-O-Si band increased with an increase in the driving frequency. The Si-OH bounding is present on the boundary surface of the bulk SiO_2 structure,as shown in Fig. 5.18, and so large amount of Si-OH bounding verifies a kind of porous films. It appears that the high driving frequency leads to porous films, which have low dielectric constant.

The current-voltage characteristics of the deposited films prepared by the coaxial configuration at driving frequencies of 2.5 and 7.5 kHz are shown in Fig. 5.19. In each case, the currents were almost 0 A below 5 V, and increased with an increase in the applied voltage beyond 5 V. At 5 V or higher, the resistance of the films prepared at a driving frequency of 2.5 and 7.5 kHz was 25 and 10 MΩ, respectively. Therefore, it is thought that the breakdown arose in the deposited

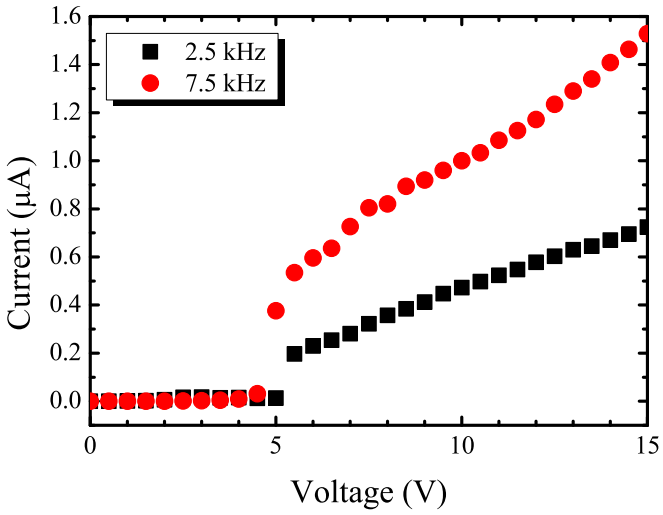

Figure 5.19 Current-voltage characteristics of deposited films prepared with coaxial configuration at driving frequencies of 2.5 kHz and 7.5 kHz.

film at 5 V. Since the thickness of the deposited film was estimated to be 100 nm, the breakdown voltage of the films were about 5×10^5 V/cm. Although the value is about 10 times lower than that of conventional SiO_2 films, this method can be realized at relatively-low temperature and at high-speed. Therefore, these films can be expected to be applied for the passivating coating of organic electroluminescence (EL) displays.

5.4 Discussion

Numerical calculation was carried out to analyze the reactions in the gas phase of the PE-CVD. Since the plasma in this experiment was at atmospheric pressure and the reaction time was much shorter than the residence time of gases in the plasma due to the gas flow velocity of about 4.7 m/s, a simplified global model of the plasma was developed. Similar global models have been widely used for analysing plasmas both at low pressure and around atmospheric pressure [5.18–20]. As global models are computationally simple, it is possible to implement a

large number of reactions and species to realistically model complicated plasma chemistry. The global model employed here accounts for 32 species, including e, He^*, He_2, He^+, He_2^+, N, N^+, N_2^+, N_4^+, O, O_3, O_2^+, O^-, $Si(C_2H_5)_3OH$, Oligomer and so on, contributing to 83 reactions in Table 5.2. There are not enough data of the dissociation of TEOS by electrons shown in Table 5.1, so that the reaction of TEOS and electrons were not considered in this calculation. The species denoted "Oligomer" is taken to mean any low molecular-weight polymer of dimer size or larger formed by the condensation reaction between two silanol-containing species. "Oligomer" can further react with O or O_3 to form a hydroxylated oligomer, designated "Oligo-OH", which is any monohydroxylated siloxane oligomer that is bigger than triethoxysilanol. Additional hydroxylation through reaction with O or O_3 yields "Oligo-$(OH)_2$".

Table 5.2 Reactions and their rate coefficients used in the global model.

Reactions	Rate constant, K (cm^3/s)	Ref.
$He + e \rightarrow He^* + e$	$f(E/p)$	[5.21]
$He + e \rightarrow He^+ + e$	$f(E/p)$	[5.21]
$He^* + 2He \rightarrow He_2 + He$	2.0×10^{-34} cm^6/s	[5.22]
$He^+ + 2He \rightarrow He_2^+ + He$	6.5×10^{-32} cm^6/s	[5.22]
$He_2 + M \rightarrow 2He + M$	1.0×10^{6} s^{-1}	[5.22]
$He_2^+ + e \rightarrow He^* + He$	8.9×10^{-9}	[5.22]
$2He_2 \rightarrow 2He + He_2^+ + e$	1.5×10^{-9}	[5.22]
$2He^* \rightarrow He_2^+ + e$	1.5×10^{-9}	[5.22]
$2He^* \rightarrow He^+ + He + e$	8.7×10^{-10}	[5.22]
$He^* + O_2 \rightarrow He + O_2^+ + e$	2.4×10^{-10}	[5.22]
$He_2 + O_2 \rightarrow 2He + O_2^+ + e$	1.0×10^{-10}	[5.22]
$He_2^+ + O_2 \rightarrow 2He + O_2^+$	1.0×10^{-9}	[5.22]
$O_2^+ + e \rightarrow 2O$	4.8×10^{-7}	[5.22]

Reactions	Rate constant, K (cm^3/s)	Ref.
$He^* + O \rightarrow He + O^+ + e$	4.3×10^{-10}	[5.22]
$O_2 + O^+ \rightarrow O_2^+ + O$	2.0×10^{-10}	[5.22]
$O_2 + e \rightarrow O_2^+ + 2e$	3.3×10^{-15}	[5.22]
$O_2 + e \rightarrow O(^1D) + O + e$	1.8×10^{-19}	[5.22]
$O(^1D) + O_2 \rightarrow O_3$	2.4×10^{-10}	[5.22]
$O_3 + O(^1D) \rightarrow O_2 + 2O$	3.8×10^{-10}	[5.22]
$O_3 + O(^1D) \rightarrow O_3 + O$	3.5×10^{-10}	[5.22]
$O(^1D) + H_2O \rightarrow 2OH$	2.2×10^{-10}	[5.22]
$O_3 + O(^1D) \rightarrow 2O_2$	1.2×10^{-10}	[5.22]
$O_3 + H\cdot \rightarrow \cdot OH + O_2$	2.9×10^{-11}	[5.22]
$O(^1D) + O_2 \rightarrow O + O_2(^3\Sigma_g^-)$	4.0×10^{-11}	[5.22]
$O(^1D) + O_2 \rightarrow O + O_2(b^1\Sigma_g^+)$	7.4×10^{-11}	[5.22]
$O(^1D) + H\cdot \rightarrow \cdot OH + O\cdot$	3.0×10^{-13}	[5.22]
$O(^1D) + O_2(b^1\Sigma_g^+) \rightarrow O + O_2(a^1\Delta_g)$	8.1×10^{-14}	[5.22]
$He + O(^1D) \rightarrow He + O\cdot$	1.5×10^{-15}	[5.22]
$O_2 + e \rightarrow 2O + e$	7.1×10^{-21}	[5.22]
$O_2(a^1\Delta_g) + O_2 \rightarrow O_3 + O\cdot$	2.9×10^{-21}	[5.22]
$O_2 + H\cdot \rightarrow \cdot OH + O\cdot$	2.5×10^{-21}	[5.22]
$O_2(a^1\Delta_g) + e \rightarrow O^- + O$	2.3×10^{-22}	[5.22]
$O_3 + H_2O \rightarrow H_2O_2 + O_2$	1.1×10^{-22}	[5.22]
$O + H_2O \rightarrow 2OH$	4.5×10^{-24}	[5.22]
$O_2 + e \rightarrow O_2(b^1\Sigma_g^+) + e$	3.1×10^{-26}	[5.22]
$He + O_3 \rightarrow He + O_2 + O$	2.3×10^{-26}	[5.22]
$He^* + N_2 \rightarrow He + N_2^+ + e$	6.9×10^{-11}	[5.22]
$He_2 + N_2 \rightarrow 2He + N_2^+ + e$	3.0×10^{-11}	[5.22]
$He_2^+ + N_2 \rightarrow He_2 + N_2^+ + e$	1.4×10^{-9}	[5.22]

Reactions	Rate constant, K (cm^3/s)	Ref.
$O(^1D) + N_2 \rightarrow O + N_2$	5.4×10^{-11}	[5.22]
$N_2 + N^+ \rightarrow N_2^+ + N$	9.4×10^{-29}	[5.22]
$N_2 + e \rightarrow 2N + e$	2.1×10^{-30}	[5.22]
$N + e \rightarrow N^+ + 2e$	9.3×10^{-39}	[5.22]
$N_2 + e \rightarrow N_2^+ + 2e$	4.0×10^{-46}	[5.22]
$N_4^+ + e \rightarrow N_2(C^3\Pi_u) + N_2$	$2.0\times10^{-6}\left(T_g/T_e\right)^{0.5}$ †	[5.23]
$N_2^+ + N_2 + e \rightarrow 2N_2$	$6.0\times10^{-27}\left(T_g/T_e\right)^{1.5}$ cm^6/s	[5.23]
$N_2^+ + 2N_2 \rightarrow N_4^+ + N_2$	5.0×10^{-29} cm^6/s	[5.23]
$M + O_3 \rightarrow M + O_2 + O$	$7.7\times10^{-9}\exp(-1.7\times10^{-19}/k_BT_g)$ ‡	[5.16]
$M + O_2 + O \rightarrow M + O_3 + O$	$1.7\times10^{-34}\exp(4.7\times10^{-21}/k_BT_g)$ cm^6/s	[5.16]
$O + O_3 \rightarrow 2O_2$	$4.9\times10^{-11}\exp(-4.7\times10^{-20}/k_BT_g)$	[5.16]
$Si(OC_2H_5)_4 + O \rightarrow Si(OC_2H_5)_3OH + CH_3CHO$	$3.4\times10^{-11}\exp(-1.8\times10^{-20}/k_BT_g)$	[5.16]
$Si(OC_2H_5)_4 + O_3 \rightarrow Si(OC_2H_5)_3OH + CH_3CHO + O_2$	$1.4\times10^{-15}\exp(-4.8\times10^{-20}/k_BT_g)$	[5.16]
$Si(OC_2H_5)_3OH + O \rightarrow Si(OC_2H_5)_2(OH)_2 + CH_3CHO$	$1.4\times10^{-15}\exp(-1.8\times10^{-20}/k_BT_g)$	[5.16]
$Si(OC_2H_5)_3OH + O_3 \rightarrow Si(OC_2H_5)_2(OH)_2 + CH_3CHO + 2O_2$	$1.4\times10^{-15}\exp(-4.8\times10^{-20}/k_BT_g)$	[5.16]
$CH_3CHO + O \rightarrow CH_3CO\cdot + \cdot OH$	$1.8\times10^{-11}\exp(-1.6\times10^{-20}/k_BT_g)$	[5.16]
$CH_3CHO + OH \leftrightarrow CH_3CO + OH$	1.7×10^{-11}	[5.16]
$CH_3CO + O \leftrightarrow CH_3 + CO_2$	1.6×10^{-11}	[5.16]
$CH_3CO + OH \leftrightarrow CH_3 + CO + OH$	5.0×10^{-11}	[5.16]
$CH_3 + O \leftrightarrow CH_2O + H$	1.3×10^{-10}	[5.16]
$CH_3 + OH \leftrightarrow CH_3O + H$	$9.5\times10^{-12}T_g^{-0.2}\exp(-9.7\times10^{-20}/k_BT_g)$	[5.16]
$CH_2O + O \leftrightarrow HCO + OH$	$3.0\times10^{-11}\exp(-2.1\times10^{-20}/k_BT_g)$	[5.16]
$CH_2O + OH \leftrightarrow HCO + H_2O$	$5.7\times10^{-15}T_g^{1.2}\exp(-3.1\times10^{-21}/k_BT_g)$	[5.16]
$HCO + HCO \leftrightarrow CH_2O + CO$	3.0×10^{-11}	[5.16]
$CH_3O + O \leftrightarrow CH_2O + OH$	1.0×10^{-11}	[5.16]
$CH_3O + OH \leftrightarrow CH_2O + H_2O$	3.0×10^{-11}	[5.16]

Reactions	Rate constant, K (cm^3/s)	Ref.
$HCO + O \leftrightarrow CO + OH$	5.0×10^{-11}	[5.16]
$HCO + OH \leftrightarrow CO + H_2O$	5.0×10^{-11}	[5.16]
$HCO + O \leftrightarrow CO_2 + H$	1.7×10^{-11}	[5.16]
$O_3 + CO \leftrightarrow CO_2 + O_2$	1.0×10^{-21}	[5.16]
$2Si(OC_2H_5)_3OH \rightarrow Oligomer + H_2O$	1.7×10^{-14}	[5.16]
$Oligomer + O \rightarrow Oligo\text{-}OH + CH_3CHO$	$3.4\times10^{-11}\exp(-1.8\times10^{-20}/k_BT_g)$	[5.16]
$Oligomer + O_3 \rightarrow Oligo\text{-}OH + CH_3CHO + O_2$	$1.4\times10^{-15}\exp(-4.8\times10^{-20}/k_BT_g)$	[5.16]
$Oligo\text{-}OH + Si(OC_2H_5)_3OH \rightarrow Oligomer + H_2O$	1.7×10^{-14}	[5.16]
$2Oligo\text{-}OH \rightarrow Oligomer + H_2O$	1.7×10^{-14}	[5.16]
$Oligo\text{-}OH + O \rightarrow Oligo(OH)_2 + CH_3CHO$	$3.4\times10^{-11}\exp(-1.8\times10^{-20}/k_BT_g)$	[5.16]
$Oligo\text{-}OH + O_3 \rightarrow Oligo(OH)_2 + CH_3CHO + O_2$	$1.4\times10^{-15}\exp(-4.8\times10^{-20}/RT_g)$	[5.16]
$Si(OC_2H_5)_3OH + Oligo(OH)_2 \rightarrow Oligo\text{-}OH + H_2O$	1.7×10^{-14}	[5.16]
$Oligo\text{-}OH + Oligo(OH)_2 \rightarrow Oligo\text{-}OH + H_2O$	1.7×10^{-14}	[5.16]
$Si(OC_2H_5)_3OH + Si(OC_2H_5)_2(OH)_2 \rightarrow Oligo\text{-}OH + H_2O$	1.7×10^{-14}	[5.16]
$Si(OC_2H_5)_2(OH)_2 + Oligo\text{-}OH \rightarrow Oligo\text{-}OH + H_2O$	1.7×10^{-14}	[5.16]
$2Si(OC_2H_5)_2(OH)_2 \rightarrow Oligo(OH)_2 + H_2O$	1.7×10^{-14}	[5.16]
$Si(OC_2H_5)_2(OH)_2 + Oligo(OH)_2 \rightarrow Oligo(OH)_2 + H_2O$	1.7×10^{-14}	[5.16]
$Oligo(OH)_2 + Oligo(OH)_2 \rightarrow Oligo(OH)_2 + H_2O$	1.7×10^{-14}	[5.16]

† T_g and T_e in all reactions refer to gas temperature and electron temperature in Kelvin.

‡ k_B is Boltzmann constant.

The input parameters are electron temperature T_e, gas temperature T_g, and gas composition of He, N_2 and O_2. For given parameters, the particle balance equation is solved simultaneously to determine the steady-state plasma composition. Although the plasma jet in this experiment is intermittently generated by a bipolar impulse power supply, for the sake of simplicity, we con-

sider the steady-state plasma. The dominant equation is expressed by the following equation:

$$\frac{dn}{dt} = S - L - D\left(\frac{2.405}{r}\right)^2 n, \tag{5.1}$$

where n is number density of particles, and S and L are source term and loss term, respectively. D is diffusion coefficient of every particle and r is radius of the plasma. For D of electrons and ions, the ambipolar diffusion coefficients were used and the values were taken from Ref. 5.24.

In this case, T_g and T_e were fixed at 170℃ and 1 eV, respectively, since the afterglow phase was considered. And, we assumed that the number density of TEOS was a constant value, 0.36% of neutral helium, from the experimental condition, and the number density of He^* atoms was constant; that in the glass tube was 10^{12} cm^{-3} and that near the substrate was 10^{10} cm^{-3} from the LAS measurement in Chapter 2. The initial density of the other active species is set to be zero. Additionally, the gas composition of helium and air (N_2:O_2 = 4:1) was also estimated from the fluid simulation in Chapter 2.

The calculated densities of several species are shown in Fig. 5.20: (a) shows time evolution of the calculated densities simulated in the glass tube, which represents the coaxial configuration, and (b) shows that near the substrate surface. When the reaction time is several tens μs, the plasma become nearly a steady state. Since the diffusion time of particles is of the order of ms, the densities of the active species are governed by the production and loss reactions in the plasma. In both cases, the electron density is around 10^{13} cm^{-3} at the steady state, and this value is in good agreement with the electron density of the microplasma array in Chapter 3 and Ref. 5.25. The positive ions in the plasma are mainly nitrogen ions, such as N_2^+ and N_4^+, even if the plasma is in the glass tube. This is because that the Penning ionization is dominant when

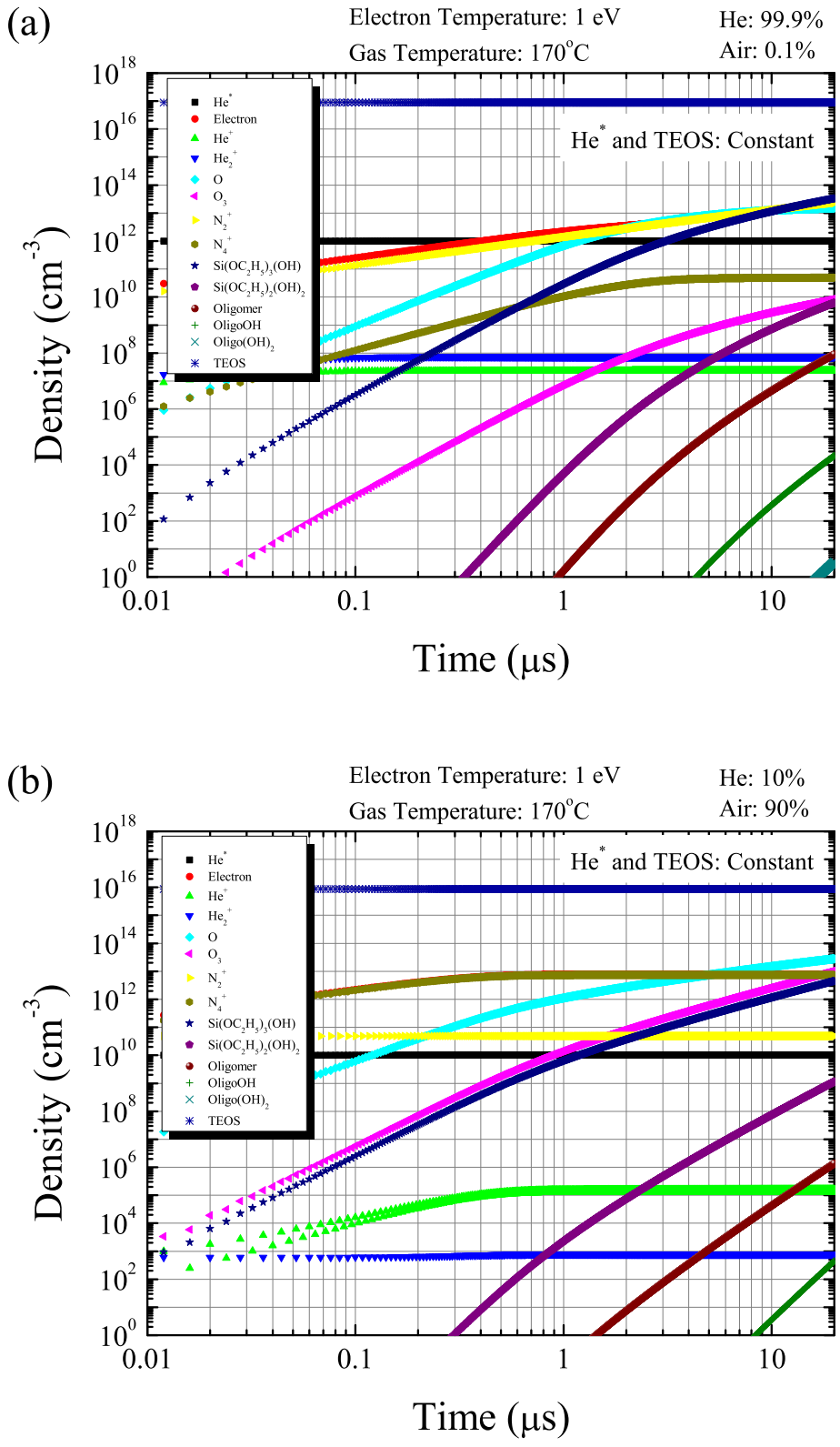

Figure 5.20 Time evolution of calculated densities of several species. Inside of glass tube; r = 1.5 mm, and the density of He^* atoms is fixed to 10^{12} cm^{-3} (a). Near substrate surface; r = 2.5 mm, estimated by visible emission, and the density of He^* atoms is fixed to 10^{10} cm^{-3} (b).

the density of N_2 molecules is low, and the direct and stepwise ionization of N_2 molecules are dominant in the case of high density of N_2 molecules. Compared with the plasma near the substrate surface, in the plasma in the glass tube, the density of $Si(OC_2H_5)_2(OH)_2$ and $Si(OC_2H_5)_3OH$, which form SiO_2 films on the substrate surface, is higher, but that of Oligomer, Oligo-OH and Oligo$(OH)_2$ whose reactivity is low to form films is also higher. Additionally, the density of O and O_3, which react with TEOS to form precursors, in the glass tube is lower than that near the substrate surface. Therefore, it is thought that powders composed of Oligomer and so on are formed in the glass tube and blown away in the gas phase in the case of the coaxial configuration. In contrast, in the crossed configuration, the plasma is generated just in the vicinity of the substrate, and the formation of powders in the gas phase is restrained. It is conjectured that this mechanism leads to higher deposition rate of the films in the tilted jet configuration.

From this result, the deposition rate of SiO_2 films was estimated by assuming that the sticking coefficient of precursors is 1, and all of precursors reaching the substrate is completely converted into the fully crystallized SiO_2. The estimated value of the deposition rate was about 2 nm/s, which is about 200 times less than experimental data. This discrepancy is probably owing to the insufficient density of the deposited SiO_2 in the experiment, the effect of the reaction between electrons and precursors, which was neglected in the calculation, and that of the surface reactions involving TEOS. The energetic electrons can dissociate the precursors effectively, and TEOS whose concentration is much higher than the precursors is regarded as playing an important role in SiO_2 deposition. Furthermore, since the change of the deposition rate was slight when additional O_3 of 10^{16} cm^{-3} was applied in the experiment, it may be that the density of O_3 was actually higher than the calculated value.

5.5 Summary

In summary, the high-speed PE-CVD of SiO_2 films was realized by the APPJ of a coaxial dielectric barrier discharge type and TEOS source. Among the three configurations used in this experiment, the tilted jet configuration was the best one for the highest deposition rate. In that case, the maximum deposition rate of SiO_2 films was about 400 nm/s at a frequency of 30 kHz with additional O_3 supply. The film contained little carbon fraction, and the breakdown voltage was about 5×10^5 V/cm. By employing the global model of the plasma used for PE-CVD, it is found that a large number of powders, which do not affect the deposition of SiO_2, are formed in the coaxial configuration. Therefore it is thought that higher deposition rate was obtained by the tilted jet configuration than the coaxial one.

References

[5.1] C. Cheng, Z. Liye and R.-J. Zhan: Surf. Coat. Technol. **200**, 6659 (2006).

[5.2] R. Foest, E. Kindel, H. Lange, A. Ohl, M. Stieber and K. D. Weltmann: Contrib. Plasma Phys. **47**, 119 (2007).

[5.3] J. H. Noh, H. K. Baik, I. Noh, J.-C. Park and I.-S. Lee: Surf. Coat. Technol. **201**, 5097 (2007).

[5.4] J. Y. Jeong, S. E. Babayan, A. Schütze, V. J. Tu, J. Park, I. Henins, G. S. Selwyn and R. F. Hicks: J. Vac. Sci. Technol. A **17**, 2581 (1999).

[5.5] T. Ideno and T. Ichiki: Thin Solid Films **506-507**, 235 (2006).

[5.6] S. E. Babayan, J. Y. Jeong, A. Schütze, V. J. Tu, M. Moravej, G. S. Selwyn and R. F. Hicks: Plasma Sources Sci. Technol. **10**, 573 (2001).

[5.7] J. Benedikt, K. Focke, A. Yanguas-Gil and A. von Keudell: Appl. Phys. Lett. **89**, 251504 (2006).

[5.8] Z. Yang, H. Shirai, T. Kobayashi and Y. Hasegawa: Thin Solid Films **515**, 4153 (2007).

[5.9] Y. Ito, K. Urabe, M. Kubo and K. Tachibana: *Proc. 18th Int. Symp. Plasma Chem.* 28P-65 (Kyoto, 2007).

[5.10] M. A. Lieberman and A. J. Lichtenberg: *Principles of Plasma Discharges and Materials Processing* (Wiley, New York, 1994).

[5.11] M. Teschke, J. Kedzierski, E. G. Finantu-Dinu, D. Korzec and J. Engemann: IEEE Trans. Plasma Sci. **33**, 310 (2005).

[5.12] K. Urabe, Y. Ito, K. Tachibana and B. N. Ganguly: Appl. Phys. Express **1**, 066004 (2008).

[5.13] K. Kitano and S. Hamaguchi: *Proc. 18th Int. Symp. Plasma Chem.* 27A-a5 (Kyoto, 2007).

[5.14] M. Matsuura, Y. Hayashide, H. Kotani and H. Abe: Jpn. J. Appl. Phys. **30**, 1530 (1991).

[5.15] T. Somekawa, T. Shirafuji, O. Sakai, K. Tachibana and K. Matsunaga: J. Phys. D: Appl. Phys. **38**, 1910 (2005).

[5.16] S. Romet, M. F. Couturier and T. K. Whidden: J. Electrochem. Soc. **148**, G82 (2001).

[5.17] O. Sakai, K. Tachibana, K. Tatsugawa, K. Ohishi and R. Inoue: Trans. Mater. Res. Soc. Jpn. **31**, 453 (2006).

[5.18] S. Kim, M. A. Lieberman, A. J. Lichtenberg and J. T. Gudmundsson: J. Vac. Sci. Technol. A **24**, 2025 (2006).

[5.19] K. R. Stalder, R. J. Vidmar, G. Nersisyan and W. G. Graham: J. Appl. Phys **99**, 093301 (2006).

[5.20] J. L. Walsh, D. X. Liu, F. Iza, M. Z. Rong and M. G. Kong: J. Phys. D: Appl. Phys. **43**, 032001 (2010).

[5.21] G. J. M. Hagelaar and L. C. Pitchford: Plasma Sources Sci. Technol. **14**, 722 (2005).

[5.22] V. Léveillé and S. Coulombe: Plasma Process. Polym. **3**, 587 (2006).

[5.23] I. A. Kossyi, A. Y. Kostinsky, A. A. Matveyev and V. P. Silakov: Plasma Sources Sci. Technol. **1**, 207 (1992).

[5.24] E. Nasser: *Fundamentals of Gaseous Inonization and Plasma Electronics* (Wiley, New York, 1971).

[5.25] O. Sakai, T. Sakaguchi, Y. Ito and K. Tachibana: Plasma Phys. Control. Fusion **47**, B617 (2005).

Chapter 6

Deposition and Analysis of ZnO Films[†]

6.1 Introduction

Plasma processes at atmospheric pressure are promising from the standpoint of developing convenient material processing. However, plasmas at atmospheric pressure have a tendency to be localized and to become thermal plasmas with high gas temperature. Such a possibility can be removed by reducing the plasma size and shortening the power-on time of the plasma [6.1].

From this point of view, an atmospheric-pressure plasma jet (APPJ) operated by a low-frequency power source (10 kHz order) in a rare gas has efficient characteristic features, such as a long plasma plume effused into the ambient air and low enough temperature to not burn human skin [6.2]. Our group has performed various diagnostics of this APPJ, which verified that the gas temperature in the jet is as low as 292 ± 20 K and that the bullet-like plume is driven by the ionization wave through the rare gas channel [6.3]. Recently, it has been attracting much attention due to its potential for various applications to material processing such as surface modification, dry etching [6.4] and plasma enhanced chemical vapor deposition (PE-CVD) [6.5]. In the previous paper [6.5] and in Chapter 5, an experimental study of PE-CVD of SiO_2 films from tetraethoxysilane (TEOS) using the APPJ was presented. The deposition rate

[†]This Chapter, in slightly altered form, is published in: Y. Ito, O. Sakai and K. Tachibana, "Study of Plasma Enhanced Chemical Vapor Deposition of ZnO Films by Non-thermal Plasma Jet at Atmospheric Pressure", Thin Solid Films **518**, 3513 (2010).

Table 6.1 Basic properties of zinc oxide.

	ZnO
Molar mass	81.408 g/mol
Crystal structure	Hexagonal wurtzite form (Fig. 6.1)
Density	5.6 g/cm^3
Melting point	1975℃
Relative permittivity	8.15
Refractive index	1.9 - 2.0
Band gap energy	~3.37 eV (Direct transition)
Lattice constant	*a*-axis: 32.407 nm
	c-axis: 51.955 nm

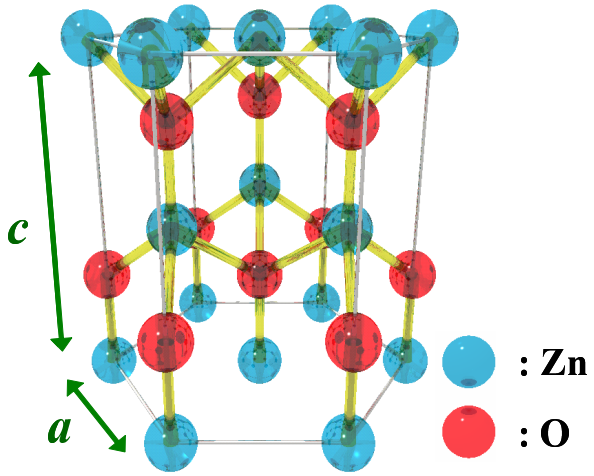

Figure 6.1 Schematic model of crystal structure of zinc oxide cristal.

of SiO_2 films increased with the driving frequency of the APPJ in a range from 2.5 to 30 kHz, and its best performance reached 400 nm/s at a driving frequency of 30 kHz with the aid of O_3 supply.

In this chapter, the deposition of zinc oxide (ZnO) films is carried out by PE-CVD system in Chapter 5. ZnO has an energy gap of 3.37 eV, i.e., it is transparent to visible light. The basic properties of ZnO are listed in Table 6.1, and the crystal structure is shown in Fig. 6.1. The oxygen ions O^{2-} in ZnO films are easily-removable by changing into oxygen molecules and the electrons are trapped in the film by oxygen vacancies as shown in Fig. 6.2; namely, ZnO is

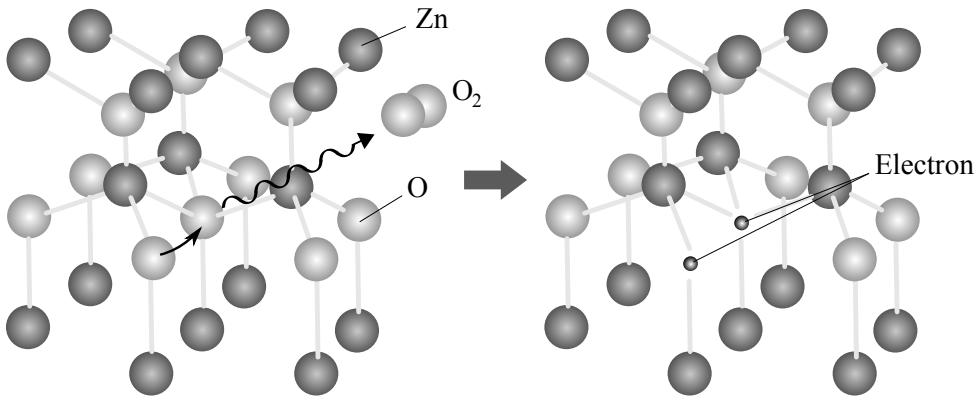

Figure 6.2 Desorption of oxygen and electron trapping in ZnO film.

typically an n-type semiconductor. Additionally, zinc is an abundant natural resource and is not harmful. Therefore, many researchers have tried various methods to deposit high-quality ZnO films as transparent conductive materials [6.6–9].

In this work, the APPJ was applied to one-dimensional deposition, which is achieved by moving a substrate and useful for roll-to-roll processing, of ZnO films as transparent conductive or semiconductor-like material, and the film quality was measured by Fourier transform infrared spectroscopy (FTIR), energy dispersive X-ray spectroscopy (EDX) and X-ray photoelectron spectroscopy (XPS).

6.2 Experimental Procedure

Figures 6.3(a) and (b) show the apparatuses used for the deposition of ZnO films using bis(octane-2,4-dionato)zinc ($Zn(OD)_2$, ADEKA Corp.) as a source material, shown in Fig. 6.3(c). The reasons that $Zn(OD)_2$ has been used in this experiment are that it is liquid at room temperature at atmospheric pressure for constant supply of source gas, and solvents with an ignition point lower than a hundred and several tens of ℃ at atmospheric pressure cannot be

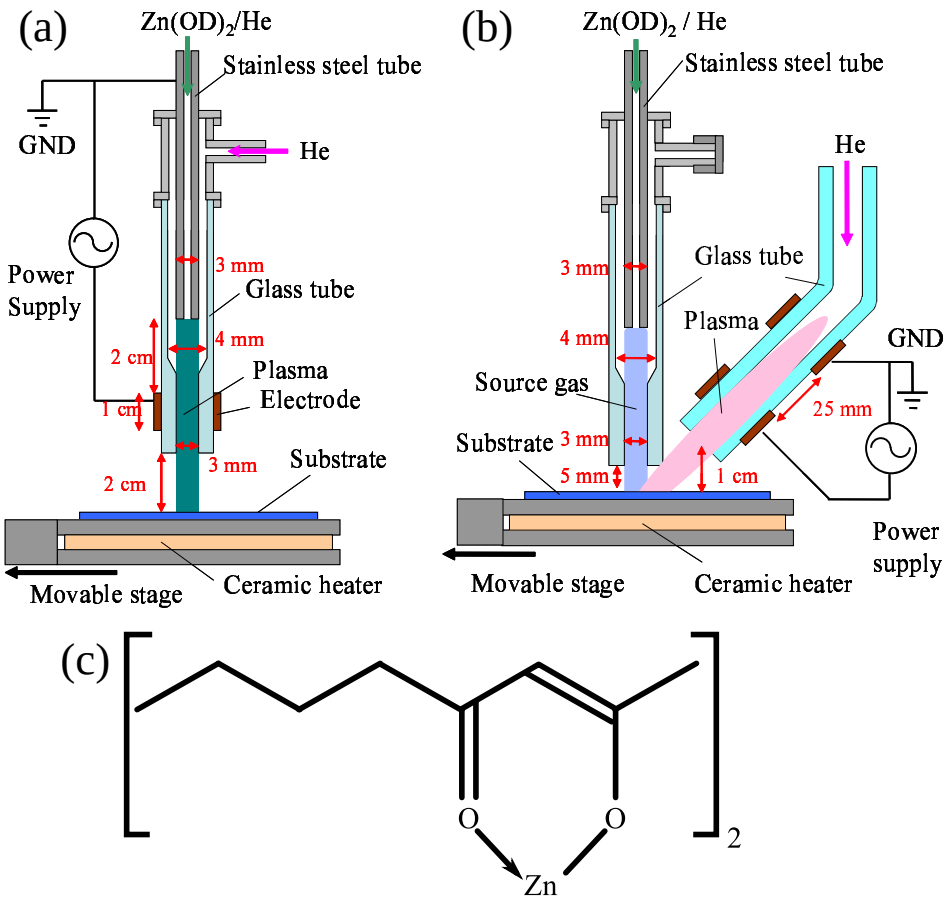

Figure 6.3 Schematic drawings of PE-CVD systems. Coaxial configuration (a) and crossed configuration (b). (c) shows the chemical structural formula of $Zn(OD)_2$.

used. And, two different configurations of the PE-CVD system have been applied in this chapter. Figure 6.3(a) shows the coaxial configuration of a zinc source supply. The plasma jet shown in Fig. 6.3(a) consisted of a glass tube of 4-mm inner diameter, equipped coaxially with a stainless steel tube of 3-mm outer diameter. The exit region of the glass tube was pinched to 3-mm inner diameter and a tubular copper electrode of 10-mm length was wound onto it. $Zn(OD)_2$ was heated to 130℃ and vaporized. At this temperature, the partial pressure of $Zn(OD)_2$ was 13 Pa. Also, the vaporized $Zn(OD)_2$ was carried to the process region by helium with a flow rate of 2 L/min and another helium gas flow of 1 L/min. The bipolar impulse voltage [6.10] with

an amplitude V_{0p} of 6 kV and the rage of a driving frequency of 5 - 30 kHz was applied to the tubular electrode. The substrate was heated to 100 - 250℃ by a heater under the substrate stage, which was placed 2 cm below the exit of the plasma jet. By moving this stage at a constant speed of 1 or 4 cm/min, one-dimensional deposition of ZnO was achieved.

On the other hand, Fig. 6.3(b) shows the crossed configuration of the PE-CVD system. The plasma jet consisted of a simple glass tube of 3-mm inner diameter and two tubular electrodes. The distance between the stage and the exit of the plasma jet was about 1 cm. The gas flow rate of helium for the plasma jet was 1.5 L/min and that for carrying $Zn(OD)_2$ was 2 L/min. The distance between the stage and the exit of $Zn(OD)_2$ was 5 mm.

To investigate the effects of the property of the substrate surface, three kinds of substrates were used in this experiment: silicon; SiO_2/Si, which was produced by thermal oxidation and the thickness of SiO_2 was about 2 μm; and glass plates whose thickness was about 1 mm. For the investigation of reactions in the gas phase, optical emission spectroscopy (OES; USB2000, Ocean Optics Inc.) was applied to the vicinity of the silicon substrate, on which the plasma jet of the coaxial configuration blew. The surface condition of deposited films was observed with an atomic force microscope (AFM; VN-8000, KEYENCE Corp.). The procedure used in assessing the deposition rate was as previously described in Chapter 5. A thin-film step-height standard method (XP-2, Ambious Technology) was used to measure the cross-sectional profile of the deposited film, which was a Gaussian-like shape and the maximum height was several hundreds of nm with a full width at half maximum (FWHM) of about 1 mm. The deposition rate was determined from the maximum height by multiplying by the moving speed of the stage and dividing by the diameter of the plasma jet which was assumed to be equal to the FWHM of the deposited film profile. For film bonding analysis, FTIR (WINSPEC100, JEOL) was applied

to the films on silicon substrate. And, the transparency of the deposited films on glass plates was measured with a visible-ultraviolet spectrophotometer (V-550, JASCO Corp.).

6.3 Experimental Results

6.3.1 Optical Emission Spectra during the Deposition

Figure 6.4 shows the spectra of OES of the coaxial configuration with and without $Zn(OD)_2$ supply. In both the cases, there are the spectra originating from nitrogen molecules and ions, which constitute the ambient air. In particular, the peaks corresponding to N_2^+ 1st negative system bands ($B^2\Sigma_u^+ - X^2\Sigma_g^+$: 391.4 nm, 427.8 nm, and so on) indicate that Penning ionization ($He^* + N_2 \rightarrow He + N_2^+(B^2\Sigma_u^+) + e$) took place in the plasma. Furthermore, there are also the peaks corresponding to N_2 2nd positive system bands ($C^3\Pi_u - B^3\Pi_g$: 310 - 360 nm), which might be due to the direct excitation of N_2 by electrons. In the case when $Zn(OD)_2$ existed, these peaks decreased little. In contrast, the peaks of helium ($3^3S_1 - 2^3P^\circ$: 706.5 nm) and N_2^+ 1st negative system bands with the existence of $Zn(OD)_2$ are smaller than those without $Zn(OD)_2$. This means that the input power provided to helium in the case of the absence of $Zn(OD)_2$ was put into $Zn(OD)_2$, or that helium excited atoms decompose $Zn(OD)_2$ when $Zn(OD)_2$ existed. Moreover, many other peaks arising from elements of the ambient air such as O and OH were observed when $Zn(OD)_2$ was absent. These radicals are considered to play important roles in decomposition of $Zn(OD)_2$ in the gas phase and formation of ZnO on the substrate surface. On the other hand, the peaks of zinc (467.6, 480.6 nm) [6.11] could not be observed. This means that $Zn(OD)_2$ did not sufficiently decompose into zinc atoms and hydrocarbon in the gas phase.

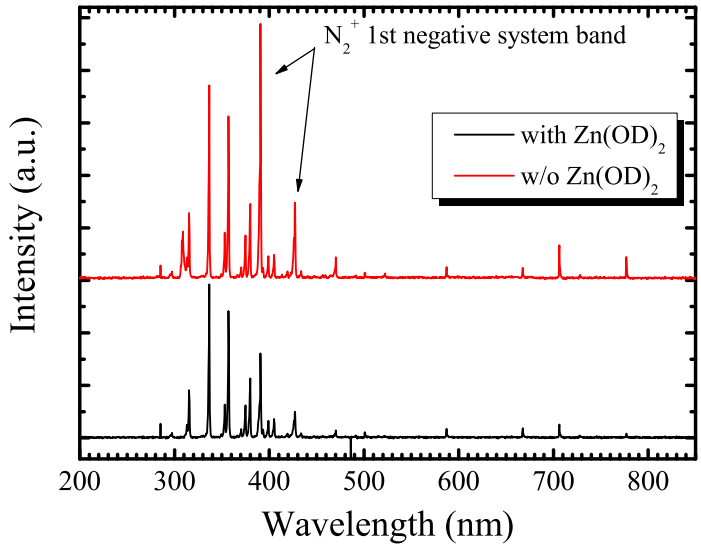

Figure 6.4 Typical optical emission spectra of the coaxial configuration of PE-CVD. Discharge parameters: total gas flow rate was 3 L/min, applied voltage was 6 kV, and driving frequency was 30 kHz.

6.3.2 High Speed Deposition of ZnO Films

PE-CVD of ZnO was carried out with the coaxial configuration with a stage speed of 4 cm/min. In this case, at the start of one-dimensional deposition, continuous deposition at a point of the substrate was carried out for 1 minute, and then the one-dimensional deposition started. Additionally, the continuous deposition at a point was performed at a halfway point for 30 seconds, and at the end of the one-dimensional deposition for 1 minute. Fig. 6.5 shows the appearance and the SEM images of the deposited films prepared with the coaxial configuration at a driving frequency of 10 kHz. The deposited film at the substrate temperature T_{sub} = 100℃ formed no interference pattern and consisted of several hundred nanometer-sized clusters on the place where the plasma was sprayed, and that at T_{sub} = 250℃ did not have measurable height, i.e., the thickness of the film was less than 10 nm. It is probably owing to too much formation

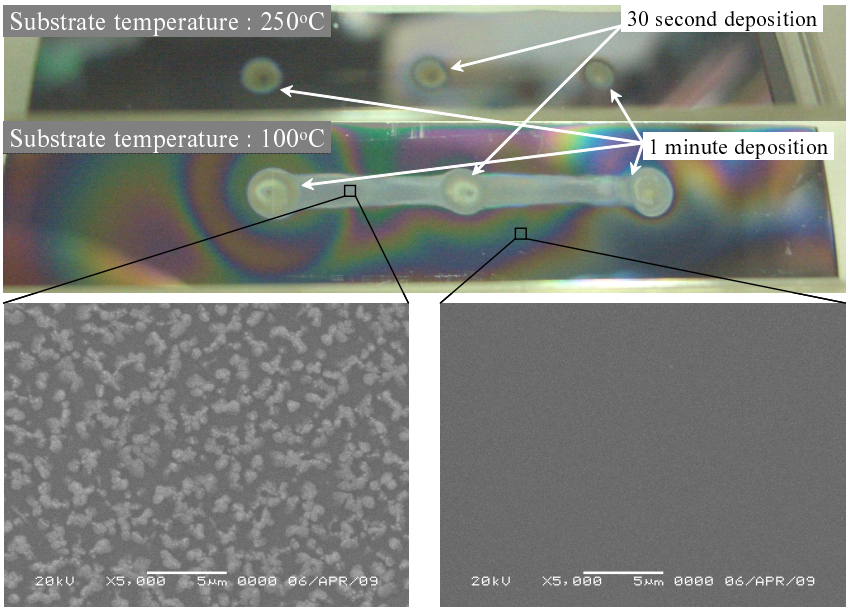

Figure 6.5 Appearance of deposited film prepared with the coaxial configuration at a driving frequency of 10 kHz with a stage speed of 4 cm/min.

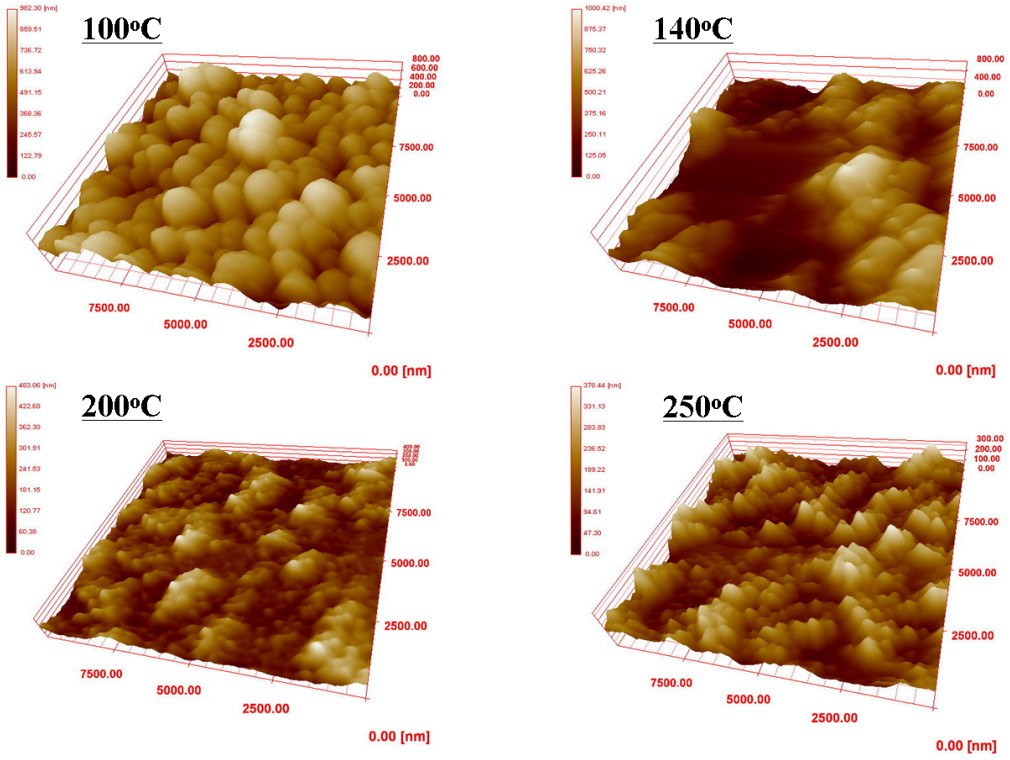

Figure 6.6 AFM images of deposited films prepared with the coaxial configuration at a driving frequency of 10 kHz at various T_{sub}.

Table 6.2 Roughness of deposited films prepared with the coaxial configuration.

T_{sub} (℃)	R_a (nm)
100	106.2
140	89.5
200	60.6
250	49.4

of inactive powders consisted of precursors in the gas phase because the reactive distance of 5.5 cm was too long to give rise to moderate reactions. In general, high concentration of source materials is subject to cause a number of powders during the PE-CVD. Additionally, as shown in Chapter 5, the reactions in the glass tube produce much more powders, and the high viscosity of $Zn(OD)_2$, about 330 mPa·s at room temperature, causes their attachment on the substrate. Therefore it is necessary to decrease the residence time of the source materials in the plasma in order to obtain smooth and clear films. Figure 6.6 shows the AFM images of the deposited films prepared with the coaxial configuration at a driving frequency of 10 kHz at various T_{sub}. The grain size of the clusters became smaller with an increase in T_{sub} as Table 6.2 shows. This indicates that the higher substrate temperature promotes the dissociation of the source materials and precursors on the surface.

In the case of the crossed configuration at a driving frequency of 30 kHz at T_{sub} = 100℃ with a stage speed of 1 cm/min, transparent films were obtained on a silicon and SiO_2/Si substrate as shown in Fig. 6.7. In this case, it is thought that moderate dissociation took place in the gas phase and the surface of the deposited film was smooth. The deposited films had almost the same cross-sectional profile nearly expressed in a Gaussian shape similar to the SiO_2 case. Figure 6.8 shows the deposition rate of the films with the crossed configuration at a stage speed of 1 cm/min. The thickness of the deposited films was hundreds of nm. The deposition rate

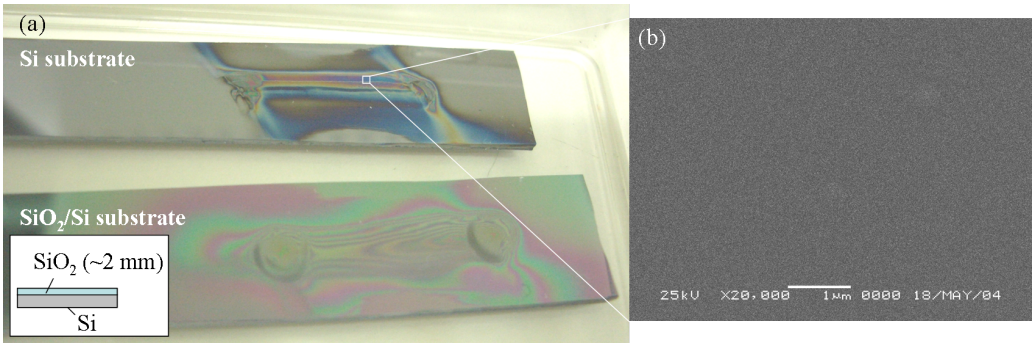

Figure 6.7 Appearance of deposited film prepared with the cross configuration at a driving frequency of 30 kHz with a stage speed of 1 cm/min and T_{sub} = 100℃.

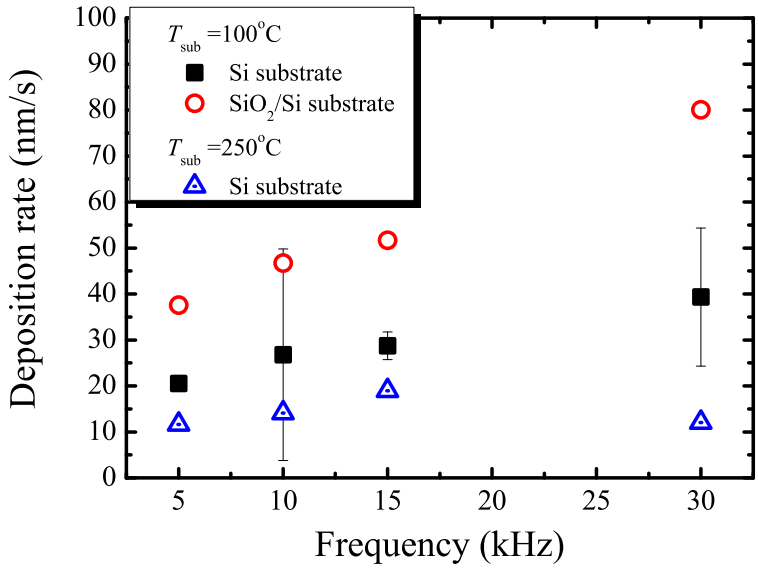

Figure 6.8 Deposition rate of the films with the crossed configuration as a function of driving frequency when one-dimensional deposition was carried out.

increased monotonically with an increase in a driving frequency, and was lower than that of SiO_2. It is thought that the molar flow rate of $Zn(OD)_2$ was about 40 times less than that of TEOS, and the fraction of carbon in $Zn(OD)_2$ was higher than that in TEOS. In the case of T_{sub} = 100℃, the deposition rate onto silicon substrates was lower than that onto SiO_2/Si substrates. This is because the plasma, which extended to the dielectric surface, spread widely by accumulated charges on the surface of the substrate with longer residence time. In the case of

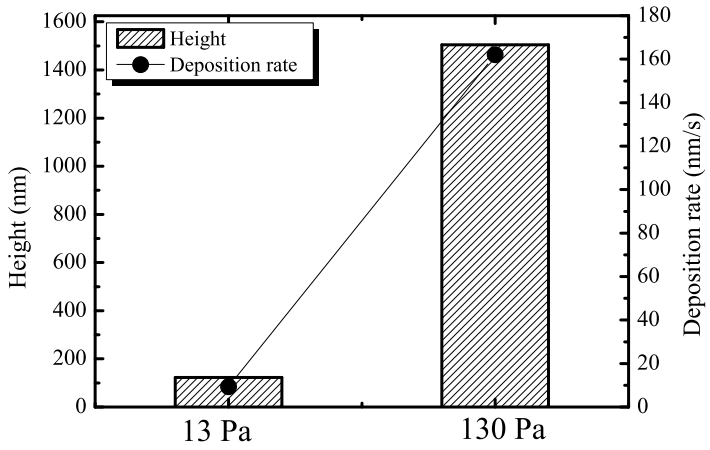

Figure 6.9 Height and deposition rate of the films depending on the supply of $Zn(OD)_2$.

T_{sub} = 250℃, the deposition rate onto silicon substrates was lower than that when T_{sub} = 100℃. There are two reasons; one is that the vaporization temperature of $Zn(OD)_2$ is around 200℃, i.e., $Zn(OD)_2$ is vaporized and blown away from the vicinity of the substrate when T_{sub} = 250℃, and the other is that the high temperature of the substrate causes the migration effect and slows down the deposition rate. Figure 6.9 shows the height and deposition rate of the films depending on the supply of $Zn(OD)_2$; the partial pressure was 13 and 130 Pa. In this case, the driving frequency was 30 kHz, the substrate temperature was 250℃, and the stage speed was 1 cm/min. From this figure, the height and the deposition rate increased with an increase in the supply of $Zn(OD)_2$. When the supply of $Zn(OD)_2$ was 130 Pa, the deposition rate was about 160 nm/s. It is about 10 times higher than that at 13 Pa.

In a comparison, there is reported result on the ZnO deposition rate of 0.15 nm/s obtained by molecular beam epitaxy (MBE) on a Si substrate with a MgO buffer layer whose thickness was 20 nm [6.12]. In a different situation with low-pressure metal organic chemical vapor deposition (MOCVD) using diethyl zinc as a source material, the deposition rate was about 0.4 nm/s on a

sapphire substrate at T_{sub} = 600℃ and a reactor pressure of 133 Pa [6.13]. In the other case, magnetron sputtering has been used for the deposition of ZnO, and the deposition rate was 1.3 nm/s at a sputter pressure of 0.8 Pa reported by Ellmer *et al* [6.14]. And, in recent years, mist CVD growth of ZnO films has been developed by Fujita's group [6.7, 15, 16]. In this case, the deposition rate reached about 8 nm/s using zinc acetate as a source and at T_{sub} = 270 - 500℃. Thus, from a standpoint of view of the deposition rate, PE-CVD using the APPJ is the fastest method.

6.3.3 Analysis of ZnO Films

FTIR spectra of the deposited films are shown in Figs. 6.10(a) and (b). The broad band centered at about 3400 cm^{-1} is attributed to the O-H stretching mode. It also contains the mode owing to water trapped in the films. In Fig. 6.10(a), the peaks centered at 2962 and 2872 cm^{-1} are C-H stretching mode in the methyl group, and those centered at 2926 and 2853 cm^{-1} are that in the methylene group of $Zn(OD)_2$. The peaks of the wave number of 1300 - 1700 cm^{-1} are the carbonate groups. Those peaks originating from C-H bonds and carbonate groups at

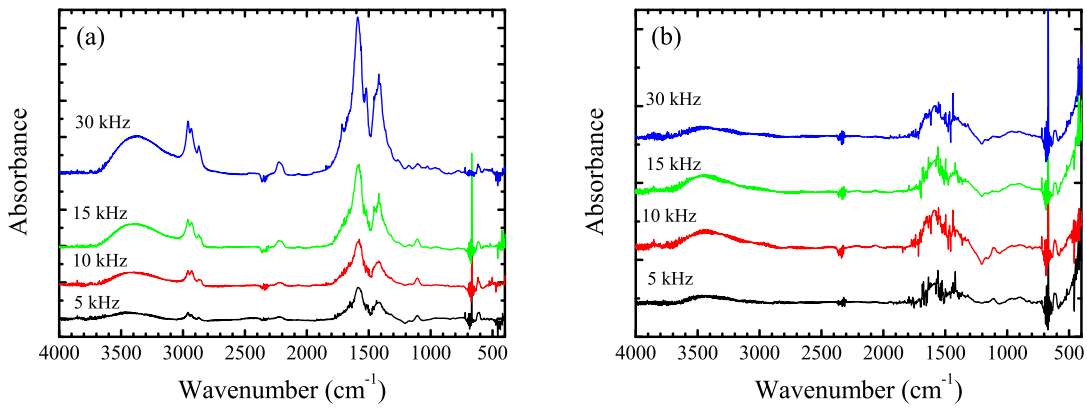

Figure 6.10 FTIR spectra of deposited films on Si substrates when the partial pressure of $Zn(OD)_2$ was 13 Pa at T_{sub} = 100℃ (a) and 250℃ (b).

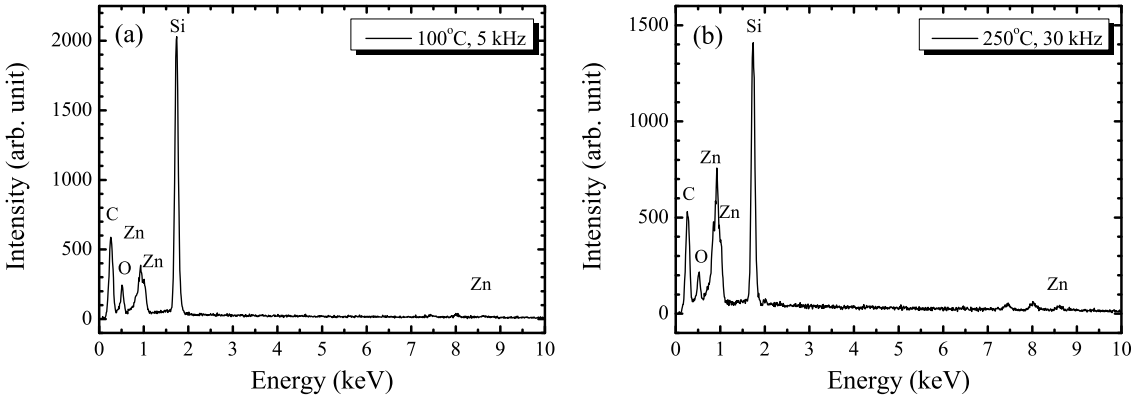

Figure 6.11 EDX spectra of deposited films when the partial pressure of $Zn(OD)_2$ was 13 Pa. T_{sub} = 100℃ at a driving frequency of 5 kHz (a) and T_{sub} = 250℃ at 30 kHz (b).

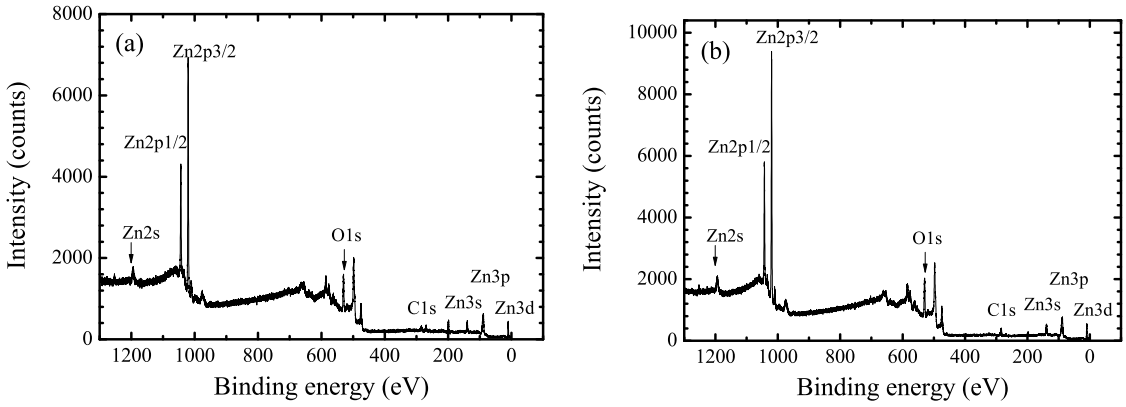

Figure 6.12 XPS spectra of deposited films at a driving frequency of 50 kHz and T_{sub} = 250℃. The partial pressure of $Zn(OD)_2$ was 13 Pa (a) and 130 Pa (b).

T_{sub} = 250℃ are lower than those at T_{sub} = 100℃ as shown in Fig. 6.10. This indicates that $Zn(OD)_2$ or the precursors decomposed insufficiently in the gaseous phase deposited on the substrate in both the cases, and the carbon contained in the precursors forms hydrocarbon and flies out due to the effect of heat on the substrate at T_{sub} = 250℃.

Figures 6.11(a) and (b) shows the spectra of EDX of the deposited films. The ratio of zinc to carbon of the deposited film at T_{sub} = 250℃ at a driving frequency of 30 kHz is higher than that at T_{sub} = 100℃ at 5 kHz. Since FTIR spectra, as shown in Fig. 6.10, have almost no change

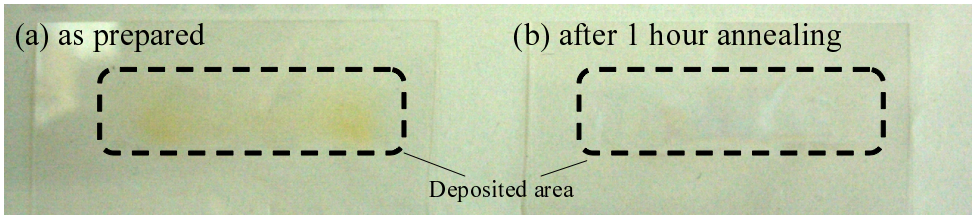

Figure 6.13 Appearance of deposited films on glass substrates: as prepared at T_{sub} = 160℃ (a) and after 1 hour annealing at 500℃ in the air (b).

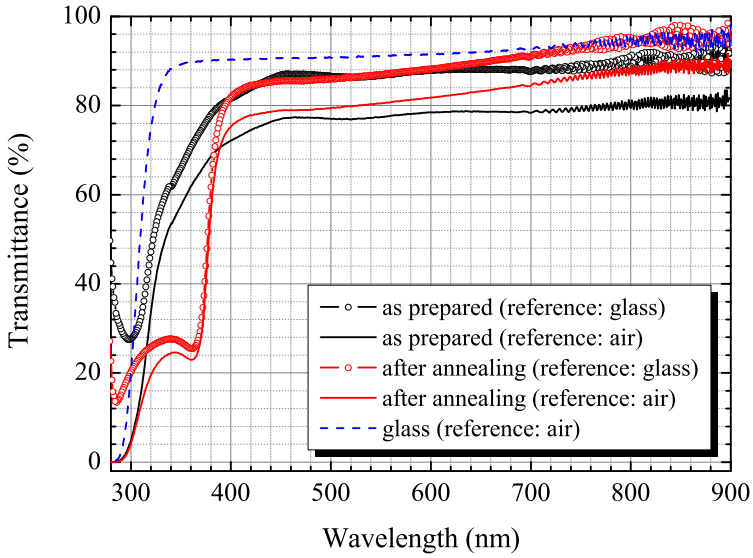

Figure 6.14 UV and visible transmittance of deposited films just prepared at T_{sub} = 160℃ and after 1-hour annealing at 500℃.

from varying the driving frequency in the range of 5 - 30 kHz, it is thought that the change of the ratio of zinc to carbon is due to the change of T_{sub}. This indicates that thermal reactions on the substrate surface play an important role in the film formation. XPS spectra of the deposited films on Si substrates is shown in Fig. 6.12. The peaks corresponding to Zn, O and C were observed. From the figures, there is no significant change of the film composition owing to the supply of $Zn(OD)_2$, i.e., there is little deterioration of the films by increasing in the deposition rate.

Table 6.3 Electrical properties of deposited films.

	(a) as prepared	(b) annealing
Resistivity (Ω cm)	4.0×10^7	1.3×10^6
Carrier concentration (cm^{-3})	1.6×10^9	1.5×10^{10}
Carrier mobility (cm^2/Vs)	1.0×10^2	1.0×10^2

Figure 6.13 shows the appearance of the deposited films on glass substrates. Figure 6.13(a) is a deposited film just prepared at T_{sub} = 160℃, and (b) is that after 1-hour annealing at 500℃ in the air. The film just prepared at T_{sub} = 160℃ was clear yellow but the film became transparent and white after 1-hour annealing at 500℃ in the atmosphere. Figure 6.14 shows the degree of the transparency of the deposited film on a glass film: just prepared at T_{sub} = 160℃ and after 1-hour annealing at 500℃. Both the films had high transparency of more than 80% in the range from 400 to 900 nm. The glass substrate is not transmissive for light with a wavelength under 300 nm. Therefore, the data at less than 300 nm of the deposited films against a glass substrate as a reference is not meaningful. The transmittance of the deposited film just prepared at T_{sub} = 160℃ shows a gradual drop in the 370 to 300 nm range. The band gap of ZnO is nearly equivalent to 370 nm, i.e., it is found that the deposited film contains a certain amount of ZnO although the film probably contains a large amount of carbon compounds. On the other hand, after 1-hour annealing at 500℃, the transmittance curve shows a sharp drop at around 375 nm and a characteristic shoulder at around 345 nm. The drop at around 375 nm is probably owing to the partial crystallization of ZnO in the deposited film by 1-hour annealing. And, the dip at around 360 nm indicates that the indirect band gap caused by some impurities and lattice defects was formed in the films [6.17–19].

In order to verify the crystal structure of the films, X-ray diffraction (XRD) measurement was applied to the deposited films. However, any signals could not be detected probably be-

cause those were amorphous films. Moreover, the Hall measurement was conducted at room temperature using the Van der Pauw method to determine the concentration of the carriers. In order to obtain a good ohmic contact, the four ends of the samples were coated with Al by a sputtering method prior to measurements. Some obtained electrical properties of the deposited films are presented in Table 6.3. After annealing, the resistivity of the deposited film became 10 times lower than that as prepared due to the increase in the carrier concentration. Therefore, the transparent and semiconductor-like films were obtained by PE-CVD using the APPJ.

6.4 Discussion

Here, the deposition mechanism is roughly estimated from the spatial configuration of the plasma jet crossing with vaporized $Zn(OD)_2$ gas flow. Assuming that $Zn(OD)_2$ is vaporized at the saturation level in the ambient gas, its flow rate to the deposition surface is 1.9×10^{-7} mol/s at partial vapor pressure of 13 Pa. If the supply amount is completely converted into fully crystallized ZnO thin films on the surface with a diameter of 4 mm, which is estimated by the diameter of the plasma jet and $Zn(OD)_2$ supply along with its spreading on the surface, the deposition rate should be 218 nm/s, which is much higher than that observed in the experiment.

In this deposition scheme, convection flux along the gas flow dominates transport of precursors rather than diffusion flux across the gas flow. That is, the key factors for deposition are decomposition rate of $Zn(OD)_2$ at the coalescence region with the plasma jet and sticking rate of the precursors on the surface. To enhance these two rates by plasmas, high electron density as a time-averaged value, efficient electron energy, and activation to yield dangling bonds on the surface might be important issues. When this type of plasma jet is used, the surface activation is

much more effective than the conventional plasma jet since the plasma jet becomes a seed to the additional discharge both on grounded metals and dielectrics. That is, if plasma parameters are enhanced to decompose more $Zn(OD)_2$ molecules, further high-rate deposition can be expected.

The linear dependence of the deposition rate at the low substrate temperature on the plasma generation frequency indicates that plasmas decompose $Zn(OD)_2$ with a significant amount of residue. A lower deposition rate at the high substrate temperature and change of the EDX spectrum indicate that the organic component was reduced by surface reaction assisted by thermal effects. The rather invariant deposition rate as a function of the plasma generation frequency at the high substrate temperature cannot be discussed using our limited experimental results, but there might be a critical substrate temperature, between 100 and 250℃, at which the deposition mechanism of precursors generated by the plasma changes. Beyond that temperature, it is thought that the carbon contamination in the deposited film is reduced and the UV transmittance of the film improves.

6.5 Summary

The deposition of ZnO films was carried out by using an APPJ and deposition rate of about 160 nm/s, which was more than 100 times higher than that of the conventional deposition schemes, was obtained. According to investigation of the properties of these films, there was much carbon content originating from source materials. However, the partial carbon component was reduced by heating the substrate to more than 250℃. The transparency of the deposited films was more than 80% in the wavelength range from 400 to 900 nm. The experimental results confirmed that the plasma jet decomposed bis(octane-2,4-dionato)zinc in the gaseous phase and on

the substrate and that there should be a critical level of T_{sub} to form high-quality ZnO films in the range from 100 to 250℃.

The resistivity of the deposited film was estimated to be about 10^6 Ωcm. It is concluded that the transparent and semiconductor-like films were obtained at high deposition rate.

References

[6.1] K. Tachibana: IEEJ Trans. Electr. Electron. Eng. **1**, 145 (2006).

[6.2] M. Teschke, J. Kedzierski, E. G. Finantu-Dinu, D. Korzec and J. Engemann: IEEE Trans. Plasma Sci. **33**, 310 (2005).

[6.3] K. Urabe, Y. Ito, K. Tachibana and B. N. Ganguly: Appl. Phys. Express **1**, 066004 (2008).

[6.4] Y. Ito, K. Urabe, M. Kubo and K. Tachibana: *Proc. 18th Int. Symp. Plasma Chem.* 28P-65 (Kyoto, 2007).

[6.5] Y. Ito, K. Urabe, N. Takano and K. Tachibana: Appl. Phys. Express **1**, 067009 (2008).

[6.6] M. Chichina, O. Churpita, Z. Hubička, M. Tichý, M. Holdová and P. Virostko: Acta Phys. Slov. **55**, 429 (2005).

[6.7] T. Kawaharamura, H. Nishinaka and S. Fujita: Jpn. J. Appl. Phys. **47**, 4669 (2008).

[6.8] S. Agouram and V. M.-S. M C Martínez-Tomás: J. Cryst. Growth **311**, 2564 (2009).

[6.9] Y. Kishimoto, O. Nakagawara, H. Seto, Y. Koshido and Y. Yoshino: Vacuum **83**, 544 (2008).

[6.10] T. Somekawa, T. Shirafuji, O. Sakai, K. Tachibana and K. Matsunaga: J. Phys. D: Appl. Phys. **38**, 1910 (2005).

[6.11] A. Klini, A. Manousaki, D. Anglos and C. Fotakis: J. Appl. Phys **98**, 123301 (2005).

[6.12] M. Fujita, N. Kawamoto, M. Sasajima and Y. Horikoshi: J. Vac. Sci. Technol. B **22**, 1484 (2004).

[6.13] Y. Zhang, G. Du, H. Zhu, C. Hou, K. Huang and S. Yang: Opt. Mater. **27**, 399 (2004).

[6.14] K. Ellmer, R. Cebulla and R. Wendt: Thin Solid Films **317**, 413 (1998).

[6.15] H. Nishinaka, T. Kawaharamura and S. Fujita: Jpn. J. Appl. Phys. **46**, 6811 (2007).

[6.16] T. Kawaharamura, H. Nishinaka, Y. Kamaka, Y. Masuda, J.-G. Lu and S. Fujita: J. Korean Phys. Soc. **53**, 2976 (2008).

[6.17] V. Kambilafka, P. Voulgaropoulou, S. Dounis, E. Iliopoulos, M. Androulidaki, K. Tsagaraki, V. Šály, M. Ružinský, P. Prokein and E. Aperathitis: Thin Solid Films **515**, 8573 (2007).

[6.18] E. Aperathitis, V. Kambilafka and M. Modreanu: Thin Solid Films **518**, 1036 (2009).

[6.19] M. Suchea, S. Christoulakis, M. Katharakis, N. Vidakis and E. Koudoumas: Thin Solid Films **517**, 4303 (2009).

Chapter 7

Conclusions

In this dissertation, the properties of microplasmas based on coaxial dielectric barrier discharges was investigated and they were applied to plasma enhanced chemical vapor deposition (PE-CVD). A microplasma array and an atmospheric-pressure plasma jet (APPJ) were demonstrated as plasma sources of the coaxial dielectric barrier discharges.

In Chapter 2, optical emission spectroscopy (OES) and laser absorption spectroscopy (LAS) were applied to the APPJ and it was found that the discharge mechanism is different between the plasma in the glass tube and that in the ambient air. OES and LAS revealed that the direct and stepwise ionization reactions of helium affect the generation of plasmas in the glass tube, but $He^*(2^3S_1)$ atoms play important roles in producing plasmas by Penning ionization with N_2 in the downstream site. Therefore, the plasma in the glass tube and that extending into the ambient air are independent of each other. Additionally, by measuring the length of the plasma plume, it was found that the plasma plume is propagated by the electric field along the helium flow and, moreover, that Reynolds number is the important factor in the plasma plume extension.

In Chapter 3, the electron density of a microplasma array in nitrogen with small admixtures of H_2O and O_2 was measured by the millimeter-wave transmission method to develop the measurement technique of nitrogen plasmas at atmospheric pressure. When plasmas extending into the ambient air is used for material processes, we have to know the effects of N_2, H_2O and O_2 on the plasma parameters. However, as shown in Chapter 2, the plasmas in nitrogen stayed up against the wall of mesh electrodes. Therefore, the mesh electrodes with narrow hollows were

used and the hollows were filled with nitrogen plasmas. Accordingly, the electron density in nitrogen of about 5×10^{12} cm^{-3}, which was confirmed by a simple particle-balance model, was obtained. Furthermore, in the case of small admixtures of H_2O and O_2, the measured electron density was of the order of 10^{12} - 10^{13} cm^{-3} in the microplasma array in every case. Consequently, it was proved that the millimeter-wave transmission method is suitable to diagnose these plasmas at atmospheric pressure.

In Chapter 4, the effect of accumulated charge on a substrate surface was investigated by measuring the discharge current. From the findings in Chapter 2, the plasma plumes in coaxial dielectric barrier discharges extending into the ambient air are affected by the electric fields and the gas flow. By comparing results obtained by the measurement and using on equivalent model of the plasma jet system, it was clarified that the accumulated charge on the substrate strongly affected the deposition rate when the capacitance on the substrate was less than 100 pF. Additionally, the capacitance of the glass capillary also affected the timing of the discharge current. Moreover, the effect of accumulated charge was ascertained through the measurement of the deposition of SiO_2 on a Si substrate, and the results were consistent with the fact that the discharge current, which is determined by the capacitance, governs the deposition rate.

In Chapter 5, PE-CVD was demonstrated by the APPJ, which was investigated in Chapters 2, 4, and the high-speed deposition of SiO_2 films was successfully achieved using TEOS source. Among the three configurations used in the experiment, the tilted jet configuration achieved the highest deposition rate. In the case, the maximum deposition rate of SiO_2 films was about 400 nm/s at a frequency of 30 kHz with an additional O_3 supply. By employing the global model of the plasma used for PE-CVD, it was found that a large number of powders, which do not affect the deposition of SiO_2, are formed in the coaxial configuration. Therefore it was thought that

higher deposition rate was obtained by the tilted jet configuration than the coaxial one.

In Chapter 6, the deposition of ZnO films was carried out by using an APPJ and deposition rate of 160 nm/s, which was more than 100 times higher than that of the conventional deposition schemes, was obtained. According to investigation of the properties of these films, there was much carbon content originating from source materials. However, the partial carbon component was reduced by heating the substrate to more than 250℃. The transparency of the deposited films was more than 80% in the wavelength range from 400 to 900 nm. The experimental results confirmed that the plasma jet decomposed bis(octane-2,4-dionato)zinc in the gaseous phase and on the substrate and that there should be a critical level of the temperature of the substrate to form high-quality ZnO films in the range from 100 to 250℃. And, the resistivity of the deposited film was estimated to be about $10^6\Omega$cm. Thus, it was concluded the transparent and semiconductor-like films were obtained at high deposition rate.

These experimental results and theoretical studies show that microplasmas based on coaxial dielectric barrier discharges at atmospheric pressure are useful tools for material processing. PE-CVD method described in this dissertation makes the deposition of oxide films dramatically easier and faster. In recent years, these kinds of oxide materials have been expanding the market of photonics and electronics. This technology offers a new avenue for novel processing, making it possible to draw sophisticated patterns freely and quickly.

In the first decade of this century, we have experienced a tumultuous world situation, therefore, remarkable breakthroughs are required and desired in the scientific and industrial fields. Consequently, it is my sincere wish that the findings and approaches of this study lead to the future development of the world.

List of Publications

[Scientific journals]

1. O. Sakai, T. Sakaguchi, **Y. Ito** and K. Tachibana, “Interaction and control of millimetre-waves with microplasma arrays”, Plasma Physics and Controlled Fusion **47**, B617 – B627 (2005).
2. K. Urabe, **Y. Ito**, K. Tachibana and B. N. Ganguly, “Behavior of N_2^+ Ions in He Microplasma Jet at Atmospheric Pressure Measured by Laser Induced Fluorescence Spectroscopy”, Applied Physics Express **1**, 66004 (2008).
3. **Y. Ito**, K. Urabe, N. Takano and K. Tachibana, “High Speed Deposition of SiO_2 Films with Plasma Jet Based on Capillary Dielectric Barrier Discharge at Atmospheric Pressure”, Applied Physics Express **1**, 67009 (2008).
4. **Y. Ito**, O. Sakai and K. Tachibana, “Study of Plasma Enhanced Chemical Vapor Deposition of ZnO Films by Non-thermal Plasma Jet at Atmospheric Pressure”, Thin Solid Films **518**, 3513 (2010).
5. **Y. Ito**, O. Sakai and K. Tachibana, “Measurement of electron density in a microdischarge-integrated device operated in nitrogen at atmospheric pressure using a millimetre-wave transmission method”, Plasma Sources Science and Technology **19**, 025006 (2010).
6. **Y. Ito**, Y. Fukui, K. Urabe, O. Sakai and K. Tachibana, “Effect of Series Capacitance and Accumulated Charge on a Substrate in a Deposition Process with an Atmospheric-Pressure Plasma Jet”, Japanese Journal of Applied Physics **49**, 066201 (2010).

[International conferences]

1. **Y. Ito**, K. Urabe, M. Kubo and K. Tachibana, “Study of plasma jet using coaxial dielectric barrier discharges at atmospheric pressure”, *The 18th International Symposium on Plasma Chemistry*, 28P-65, August 2007 Kyoto, Japan (Poster presentation).
2. **Y. Ito**, K. Urabe, M. Kubo and K. Tachibana, “Studies on plasma jet using coaxial dielectric barrier discharges at atmospheric pressure”, *The 1st GCOE International Symposium on Photonics and Electronics Science and Engineering*, P-30, March 2008 Kyoto, Japan (Poster presentation).
3. **Y. Ito**, K. Urabe, N. Takano and K. Tachibana, “Diagnostics of Low-frequency Plasma jet and its Application to Deposition of Silicon Dioxide Films”, *The 3rd International School of Advanced Plasma Technology*, P-28-10, July 2008 Varenna, Italy (Poster presentation).
4. **Y. Ito**, Y. Fukui, K. Urabe, and K. Tachibana, “Study of Plasma Enhanced Chemical Vapor Deposition of Oxide Films by using Non-thermal Plasma Jet at Atmospheric Pressure”, *The 2nd GCOE International Symposium on Photonics and Electronics Science and Engineering*, P-40, March 2009 Kyoto, Japan (Poster presentation).
5. **Y. Ito**, K. Urabe, N. Takano, Y. Fukui, O. Sakai and K. Tachibana, “Plasma jet CVD of oxide materials for optical functional devices”, *ISPC-19 Pre-Symposium in Japan “Toward the Next Generation of Plasma Science and Technology”*, May 2009 Kyoto, Japan (Poster presentation).
6. **Y. Ito**, Y. Fukui, K. Urabe and K. Tachibana, “Study of Plasma Enhanced Chemical Vapor Deposition of Oxide Films by Non-thermal Plasma Jet at Atmospheric Pressure”, *The 19th International Symposium on Plasma Chemistry*, O3-7, July 2009 Bochum,

Germany (Oral presentation).

7. **Y. Ito**, O. Sakai and K. Tachibana, “Study of Plasma Enhanced Chemical Vapor Deposition of Zinc Oxide Films by Atmospheric-Pressure Plasma Jet”, *2nd International Symposium on Advanced Plasma Science and its Applications for Nitrides and Nanomaterials (ISPlasma2010)*, PB021A, March 2010 Nagoya, Japan (Poster presentation).

[Domestic conferences]

1. **Y. Ito**, O. Sakai, T. Sakaguchi and K. Tachibana, “Measurement of electron density in N_2 coaxial micro dielectric barrier discharges at atmospheric pressure”, *Extended Abstracts (The 66th Autumn Meeting, 2005); The Japan Society of Applied Physics*, 10p-ZG-17, September 2005 Tokushima (Oral presentation).
2. **Y. Ito**, O. Sakai and K. Tachibana, “Effect of gas flow in integrated coaxial micro dielectric barrier discharges at atmospheric pressure”, *Extended Abstracts (The 67th Autumn Meeting, 2006); The Japan Society of Applied Physics*, 1p-S-7, September 2006 Kusatsu (Oral presentation).
3. **Y. Ito**, M. Kubo, O. Sakai and K. Tachibana, “Integration of coaxial micro dielectric barrier discharges at atmospheric pressure”, *The 24th Symposium on Plasma Processing (SPP-24)*, A4-02, January 2007 Toyonaka (Oral presentation).
4. **Y. Ito**, O. Sakai and K. Tachibana, “Surface modification using coaxial micro dielectric barrier discharges at atmospheric pressure”, *Extended Abstracts (The 54th Spring Meeting, 2007); The Japan Society of Applied Physics and Related Societies*, 29p-G-10, March 2007 Sagamihara (Oral presentation).
5. **Y. Ito**, N. Takano and K. Tachibana, “Fabrication of SiO_2 films using the low-temperature plasma jet at atmospheric pressure”, *Extended Abstracts (The 68th Autumn Meeting, 2007); The Japan Society of Applied Physics*, 4p-ZA-2, September 2007 Sapporo (Oral presentation).
6. **Y. Ito**, N. Takano and K. Tachibana, “Deposition of Silicon Dioxide Films Using Low-Temperature Plasma Jet at Atmospheric Pressure”, *The 25th Symposium on Plasma Processing (SPP-25)*, P2-33, January 2008 Yamaguchi (Oral presentation).

7. **Y. Ito**, N. Takano and K. Tachibana, “Enhanced deposition of SiO2 by the low-temperature plasma jet CVD at atmospheric pressure”, *Extended Abstracts (The 55th Spring Meeting, 2008); The Japan Society of Applied Physics and Related Societies*, 27p-S-11, March 2008 Funabashi (Oral presentation).
8. **Y. Ito**, K. Urabe, N. Takano and K. Tachibana, “Dependence on the kinds of substrates for the CVD of SiO_2 films by low-temperature plasma jet at atmospheric pressure”, *Extended Abstracts (The 69th Autumn Meeting, 2008); The Japan Society of Applied Physics*, 5a-ZF-8, September 2008 Kasugai (Oral presentation).
9. **Y. Ito**, K. Urabe and K. Tachibana, “One-dimensional high-speed deposition of SiO_2 using low-temperature plasma jet at atmospheric pressure”, *The 2nd Meeting on New Field of Plasma “Plasma Generation and Low Temperature Thin Film Processing”*, December 2008 Higashi-Hiroshima (Oral presentation).
10. **Y. Ito**, O. Sakai and K. Tachibana, “Study of Plasma Enhanced Chemical Vapor Deposition of ZnO Films by Non-thermal Plasma Jet at Atmospheric Pressure”, *The 22nd Symposium on Plasma Science for Materials*, B2-2, June 2009 Tokyo (Oral presentation).
11. **Y. Ito**, O. Sakai and K. Tachibana, “Study on high speed deposition of zinc oxide films by using plasma jet at atmospheric pressure”, *Extended Abstracts (The 70th Autumn Meeting, 2009); The Japan Society of Applied Physics*, 10p-N-8, September 2009 Toyama (Oral presentation).

Acknowledgements

First of all, My deepest appreciation goes to Professor Kunihide Tachibana, a professor emeritus at Kyoto University and a professor at Ehime University. He provided appropriate direction and priceless inspiration, and gave me invaluable advice, comments and encouragement for my study since I was an undergraduate student.

I also express my deep gratitude to Professor Gikan Takaoka, Professor Masao Kitano, and Professor Shizuo Fujita for their inspiring advice, stimulating comments, and fair consideration on my work and this dissertation.

I would particularly like to express my gratitude to Associate Professor Osamu Sakai for his considerate teaching, profound suggestions and ceaseless encouragement. I also would like to express my appreciation to Professor Tatsuru Shirafuji, a former Associate Professor at Kyoto University (now a professor at Nagoya University), Lecturer Toshihiro Nakamura, and Mr. Makoto Kubo, a former Assistant professor, for their kind supports and helpful advice.

I express my gratitude to all of students who have discussed and commented my work and staff members who have supported my work in the Plasma Science and Engineering Laboratory including the past members of Tachibana Laboratory. Especially, I would like to thank Mr. Yutaka Kishimoto (now at Murata Manufacturing Co., Ltd.), Mr. Takui Sakaguchi (now at ROHM Co., Ltd.), Dr. Dae-Sung Lee (now a researcher at the University of Illinois at Urbana-Champaign), Dr. Nobuhiko Takano (now at Fujifilm Corporation), Mr. Keiichiro Urabe, and Mr. Yutaka Fukui for fruitful discussion and sharing a sense of accomplishment in my life as a researcher. I am also indebted to Ms. Keiko Yamada, an office administrator in the Plasma Science and Engineering Laboratory, for all of her kind assistance in my laboratory life.

Special thanks to Professor Gerrit Kroesen, Dr. Eva Stoffels, Ms. Rina Boom and all of staff members and students in Kroessen's group at Eindhoven University of Technology. They provided me inspiration and support for my overseas study and life in the Netherlands.

I received generous support from Furukawa Electric Co., Ltd. In particular, I have greatly benefited from Mr. Hisashi Koaizawa, Mr. Nobuaki Orita, Mr. Norihisa Shibayama (now at Macro BEANS Center in BEANS Laboratory, Micromachine Center) and Dr. Kaoru Mitsuhashi (now a research associate at Yokohama National University).

Moreover, I received generous financial support of the USHIO Foundation for my study and life. And, I was also supported by the Ministry of Education, Culture, Sports, Science and Technology in Japan through the Global COE program (the Center of Excellence for Education and Research on Photonics and Electronics Science and Engineering, Kyoto University). So, I would like to sincerely thank Professor Susumu Noda, who is the project leader, Ms. Mizuki Yamada, who is the office administrator, and all the concerned parties.

This work was partially supported by the Center of Excellence for Education and Research on Photonics and Electronics Science and Engineering of Kyoto University, Venture Business Laboratory of Kyoto University, a transferred research fund from the New Energy and Industrial Development Organization through Furukawa Electric Corporation.

Finally, let me express my heartfelt appreciation to my parents, little brother, little sister, and all of my friends for their deep understanding, sincere encouragement and continuing supports.

December, 2009 in Kyoto

Yosuke ITO